THREE THEORETICAL STUDIES OF FERROELECTRIC MATERIALS IN DIFFERENT GEOMETRIES

by

LUCIA PÁLOVÁ

A Dissertation submitted to the

Graduate School-New Brunswick

Rutgers, The State University of New Jersey

In partial fulfillment of the requirements

For the degree of

Doctor of Philosophy

Graduate Program in Physics and Astronomy

Written under the direction of

Professor Premala Chandra

And approved by

_____

_____

_____

_____

_____

New Brunswick, New Jersey

October, 2010

ABSTRACT OF THE DISSERTATION

Three Theoretical Studies of Ferroelectric Materials in Different Geometries

By LUCIA PÁLOVÁ

Dissertation Director:

Professor Premala Chandra

Using a combination of numerical and analytical techniques, I present characterizations of ferroelectric materials in bulk, thin-film and nanostructure geometries. My results have impact on ongoing research and on design for nanodevices.

Size-dependent effects in ferroelectrics are important due to their long-range electrostatic interactions; thus their dielectric properties depend on electromechanical boundary conditions. In my first study, I address the effects of strain on the measured properties of thin-film (TF) ferroelectrics. It has been suggested that the observed suppression of many TF dielectric characteristics implies underlying strain gradients in the film. I show that the same effects can be explained by a simpler model with homogeneous strain, and I suggest a "smoking gun" benchtop probe.

The quantum paraelectric-ferroelectric transition (QPFT) is the topic of my second study. Using methods including finite-size scaling and self-consistent Gaussian theory, I calculate the classical-quantum crossover in the dielectric susceptbility and the resulting temperature-pressure phase diagram; comparison with current experiment is excellent and predictions are made for future measurements. Here, temperature can be considered a "finite-size effet" in time, and previous results on the QPFT using diagrammatic techniques are recovered and extended using this approach.

Recent synthesis of artificially structured oxides with "checkerboard" patterning at the nanoscale

has been reported, and this serves as motivation for my third study. Here, I use first-principles methods to characterize an atomic-scale $BiFeO_3$-$BiMnO_3$ nanocheckerboard, and find that it has properties that are distinctive from those of either parent compound. More specifically, it has both a spontaneous polarization and magnetization, and also displays a magnetostructural effect. My work on this prototypical multiferroic nanocheckerboard motivates further theoretical and experimental studies of new heterostructures with properties that are geometrically induced.

Acknowledgements

I owe my deepest gratitude to Professor Premi Chandra for her support and guidance during my graduate study at Rutgers University. She sets a great example as a woman scientist, teacher, and researcher whose love for science is contagious. Many thanks for the numerous discussions, advice, and encouragement, without which I would not have achieved my goals. Last but not least, thank you for the fruitful women's lunches, which contribute to the richness of our physics department.

I am much indebted to Professor Karin M. Rabe and Professor Piers Coleman, whose guidance has been very valuable. It has been my pleasure to collaborate with you. Thank you for sharing new ideas; these contributed in many ways to the results of my thesis.

Many thanks to the faculty and collaborators, Professors Eva Y. Andrei, Paul L. Leath, Andrew J. Baker, Matthew Dawber, Ichiro Takeuchi, Daisuke Kan, David Vanderbilt, Donald R. Hamann, David C. Langreth, Valery Kiryukhin, Sang-Wook Cheong, Valanoor Nagarajan, Judith Driscoll, Satyabrata Patnaik, Gustau Catalan, David Khmelnitskii, Stephen E. Rowley, Siddarth S. Saxena, Gilbert G. Lonzarich, Jim F. Scott, Eric Bousquet, Nicola A. Spaldin, Craig J. Fennie, Jeffrey B. Neaton, Claude Ederer, Viktor Oudovenko, for their valuable discussions.

As a special person in my life from now till forever, I would like to thank my son Patrik for bringing sunshine into my days. Thank you for giving me strength and reasons to be a better mommy. I am grateful to my loving husband, Martin, for being here for Patrik and me. Thanks for carrying the weight of your graduating wife, and thank you for listening.

My achievements would not have been possible without the extraordinary love and support of my mother, Anna. She sets an example for me as a great woman, mother, and grandmother.

Thanks to my friends and office mates, Rebecca Flint, Kasturi Basu, Senia Katalanic, Adina Luican, Maria E. Pezzoli, Marianna Maltseva, Shen Li, Andrei Malashevich, Carl-Johan Eklund, Ilya Berdnikov, Sinisa Coh, Anindya Roy, Alexey A. Soluyanov, Chuck-Hou Yee, Sung Po Chao,

Table of Contents

List of Tables

List of Figures

Chapter 1

Introduction

1.1 Motivation

1.1.1 A Brief History of Ferroelectrics

Ferroelectricity was first observed in two water-soluble crystals, Rochelle salt (sodium potassium tartrate tetrahydrate) and KDP (potassium dihydrogen phosphate) [1, 2]. However, it took more than twenty years for a new class of much simpler materials, perovskite oxides, to be discovered [3]. Though there were early theoretical studies on the Rochelle salt [4], the discovery of these simple perovskite ferroelectrics has led to much progress in understanding the physics underlying the observed experimental phenomena. [see Fig. 1.3] [5–7].

The first studied ferroelectric perovskite is now well known $BaTiO_3$ [8, 9] [see Sec. 1.2.3]. After its discovery, many new ferroelectrics have been studied, leading to deeper understanding of their properties. A breakthrough was made with the development of the soft mode description of the ferroelectric transition [10, 11]. Today, we use the phenomenological Landau-Ginzburg theory with symmetry considerations placed on the order parameter [polarization] to describe phase transitions in ferroelectrics [12, 13] [see Sec. 1.2.4]. After an era of bulk perovskites, miniaturization took place, and thin ferroelectric films [14, 15] and later perovskite oxide superlattices [16–26] were introduced. The goal is now to design new materials with better properties, such as higher polarization or critical temperature values, than those found in nature. Today, a triumph of ferroelectric materials is in their wide functionality, with important applications that include sonar, medical ultrasound, ferroelectric random access memories (FeRAMs), and even chips inside ski passes.

1.1.2 Ferroelectric Applications

Ferroelectric random access memory (FeRAM) is a promising application of ferroelectric materials. FeRAM is non-volatile as it retains stored information even when not powered. This is a very useful property because information is automatically stored, without pressing a "save" button. For example, non-volatile competing Flash memories are currently used in digital cameras. In contrast to Flash memories, FeRAM's advantages are its lower power consumption, faster write performance and a greater maximum number of write-erase cycles [27, 28]. So why don't we use FeRAM memories instead of Flash memories in our digital cameras? One of the big problems is that the existing FeRAMs have lower storage density than their Flash counterparts. To increase the amount of information stored per unit of area, we need to go to smaller scales, and this is exactly where basic research comes into play. It concentrates on questions related to nanoscales: What happens to electric properties when we go to smaller sizes? Is there any difference in ferroelectric film vs. bulk behavior?

The answer is that there is a huge difference between bulk ferroelectric properties and those of thin ferroelectric films. This is due to the fact that the electromechanical boundary conditions are very important at small scales because of the underlying long-range electrostatic interactions in ferroelectrics, in contrast to short-range [Heisenberg] spin interactions in ferromagnets. Of course, when one starts to talk about boundary conditions, it is important to know details associated with the ferroelectric film. How is the film fabricated? What and where are the electric contacts? It turns out that most of the films are epitaxially grown on substrates, and the choice of the substrate influences the dielectric properties of a ferroelectric film a lot. For example, a material that displays no bulk ferroelectric behavior may be ferroelectric as a thin film grown on a specific substrate [15]. Similarly, the choice of metalic contacts matters, and can lead to suppression of the ferroelectric signal [switchable polarization, see Sec. 1.2.1] due to depolarization effects [29].

Ferroelectric materials have the ability to generate an electric signal upon deformation. This so called piezoelectric property [see Eq. (1.9)] is in fact what makes these materials so useful. From a guitar pickup to a piezoelectric motor, the mechanical energy is converted to an electric signal, or

vice versa. For example in a piezoelectric microscope, the piezoelectric crystal is used to finely tune changes in position with an electric signal. In sonar, the sound [or pressure variations] is detected and generated using an electric signal. Similarly, motion of a baby in the uterus is detected by medical ultrasound devices.

The technologically most important ferroelectric, and piezoelectric nowadays is $PbZr_{1-x}Ti_xO_3$ (PZT). Its advantage lies in large values of its spontaneous polarization and its piezoelectric co-eiffcient that are important for good signal readout and efficient electromechanical conversion, respectively. PZT also displays reliably constant behavior over a wide temperature range; this characteristic is connected to its morphotropic, temperature-independent, phase boundary between two structural phases at about $x = 50\%$ of Ti concentration. Unfortunately, because PZT contains lead, an environmentally unfriendly element, much current research focuses on identifying and designming lead-free ferroelectrics with comparable properties.

1.1.3 Ferroelectrics in Solid State Theories

The reason why we study ferroelectrics is not only because of their wide range of technological applications, but also because these materials turn out to be useful examples of systems, for which simple theoretical descriptions work very well. One such theory is a phenomenological Landau [or Landau-Ginzburg] theory of phase transitions. This theory is based on describing the system by the order parameter, polarization in this case, that takes into account symmetries of the studied phases. Although Landau theory is usually connected with the description of magnetic transitions in most of the textbooks, it actually works much better for paraelectric-ferroelectric transitions [see Sec. 1.2.4]. In essence, the Landau theory is a mean field theory. Therefore it works well when the coordination number [number of nearest neighbours] is high. This can be achieved either by large dimensionality of the system, or by long-range interactions; the presence of Coulomb interactions in ferroelectrics leads to the fact that Landau theory is reliable in these systems for a temperature window close to the ferroelectric-paralectric phase transition. [13]

Another reason why ferroelectric materials have been studied recently is because of their connection to quantum criticality. Because ferroelectric materials are insulating systems [see Sec. 1.2.1], there are no free charges and thus no electronic dissipation. Because there is limited disorder and no other competing fixed points in these materials, they display very simple behavior close to their quantum critical point at low temperatures and high pressures [see Sec. 1.3.2 and Chapter 3]. Furthermore, unlike magnetic systems, they can be studied below, at or just above their upper critical dimension. Finally, another advantage of these quantum critical systems is that the theory can be directly compared to ongoing experiment [30–32].

1.1.4 Multiferroics

Multiferroics are materials where electric and magnetic [sometimes also elastic] properties are combined in a single phase material. Just as ferroelectric materials are used for ferroelectric memories, current research concentrates on questions related to possible multiferroic memories. A memory element made of a multiferroic material can be in one of four possible states [instead of two in a traditional memory element], which means that twice as much information can be stored per cell. Another advantage of multiferroic memories lies in that they support fast low-power electrical write and non-destructive magnetic read operation. This would remove the disadvantage of the destructive read process currently associated with ferroelectric memories [33, 34]. However, to implement such memory one needs a material whose magnetic state can be changed by applying an electric field or vice versa, a material with a high value of the so called magnetoelectric coupling. Of course, for a multiferroic memory to be used technologically, one also needs a material with room temperature ferroelectric and ferromagnetic behavior.

In general, it is difficult to find a room temperature single-phase multiferroic with large magnetoelectric coupling. This is mostly because different criteria need to be fulfilled in order for a material to be both, a ferroelectric and a ferromagnet. Broken inversion symmetry needs to be satisfied in the case of ferroelectrics [see Sec. 1.2.1], whereas broken time-reversal symmetry in the case of ferromagnets [35]. Ferroelectrics are insulators [we do not want any free carriers, but electric

dipoles], whereas ferromagnets are usually metals [as for example iron], where spins of electrons of partially filled d shells magnetically order [33, 36]. Some materials do exhibit ferroelectricity and ferromagnetism simultaneously in spite of these criteria, but they either have a weak magnetoelectric coupling [for example, $BiFeO_3$, see Sec. 1.2.3], or their critical temperatures, or electric polarizations are very low [$\sim 10K$ and $\sim 10^{-2}\mu C/cm^2$, respectively] [33, 37]. Because it is difficult to find a single phase multiferroic, current research also concentrates on questions related to artificial design of new multiferroic materials.

1.2   Overview of Ferrolectrics

1.2.1   Ferroelectric

Let us now properly define a ferroelectric material (ferroelectric). A ferroelectric is an insulating system with two or more discrete stable [or metastable] states of different nonzero electric polarization in zero applied electric field, referred to as "spontaneous" polarization. For a system to be considered ferroelectric, it must be possible to switch between these states with an applied electric field, which changes the relative energy of the states through the coupling of the field to the polarization $-\vec{E} \cdot \vec{P}$ [38]. A typical dependence of energy on the spontaneous polarization is shown in Fig. 1.1, where the ferroelectric undergoes a phase transition from a paraelectric [non-polar] high temperature to a ferroelectric [polar] low temperature phase at a critical temperature T_c.

An essential property of a ferroelectric is that it is characterized by a hysteresis loop, that is, the dependence of the electric polarization on an applied electric field, Fig. 1.2. When an electric field is first applied, the ferroelectric becomes polarized developing a finite value of the electric polarization, and it stays polarized having a nonzero spontaneous polarization value even when the field is turned off. The latter feature distinguishes a ferroelectric and a paraelectric, in which polarization scales linearly with an applied electric field, and vanishes when the field is turned off. Switching between two spontaneous polarization states in a ferrolectric is achieved by inverting the sign of the applied electric field, as is shown in Fig. 1.2. This switching property between "up"
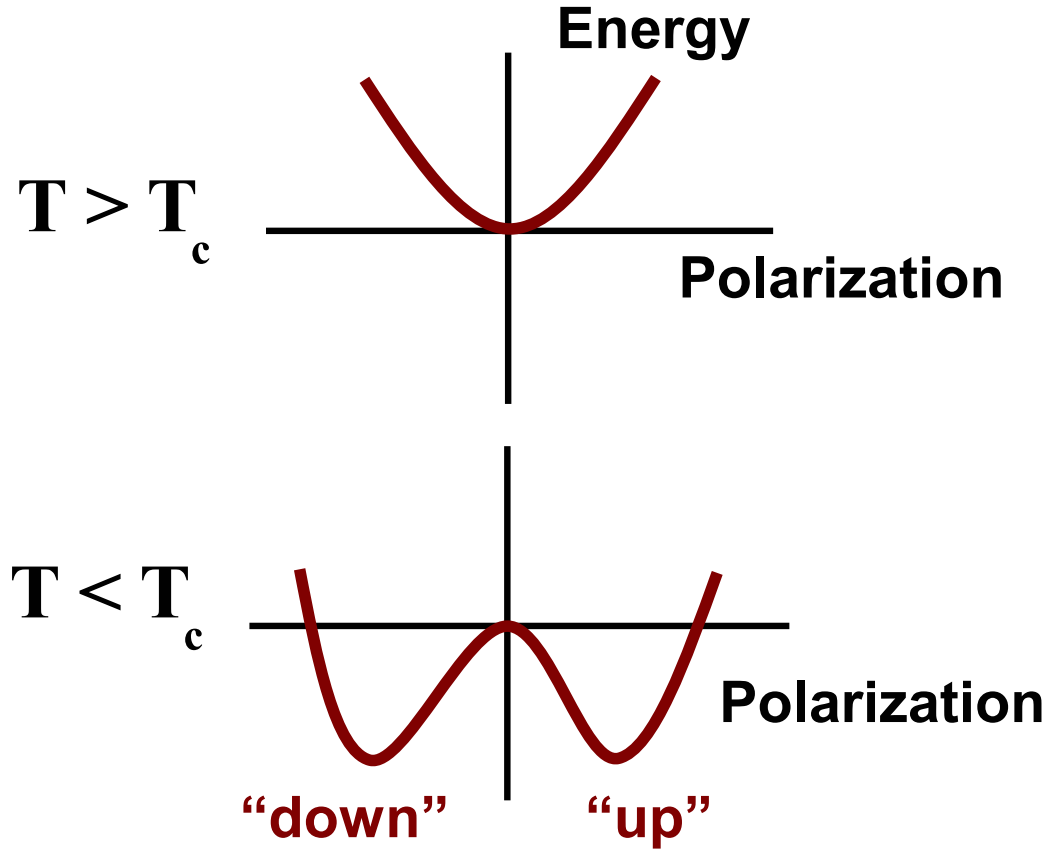
Figure 1.1: Energy versus "spontaneous" polarization is sketched above and below critical temperature T_c. Two minima in the energy for two distinct spontaneous polarization ["up" and "down"] states form below T_c, whereas the polarization is zero above T_c [see Fig. 1.5]. Electric field switches between the "up" and "down" ferroelectric states [see Fig. 1.2].

and "down" polarization states [see Figs. 1.1 and 1.2] has turned out to be useful for encoding information as "0" and "1" states in the ferroelectric random access memory (FeRAM).

The electric polarization $\vec{P}$ is usually defined for a finite system as the electric dipole moment per volume V, where the dipole moment is obtained from the charge density $\rho(\vec{r})$,

$$\vec{P} = \frac{1}{V} \int d\vec{r} \, \vec{r} \rho(\vec{r}). \tag{1.1}$$

However, it has been discussed that Eq. (1.1) is not a useful bulk definition of the polarization in a finite crystal due to possible redistribution of surface charges, nor is it a useful definition for
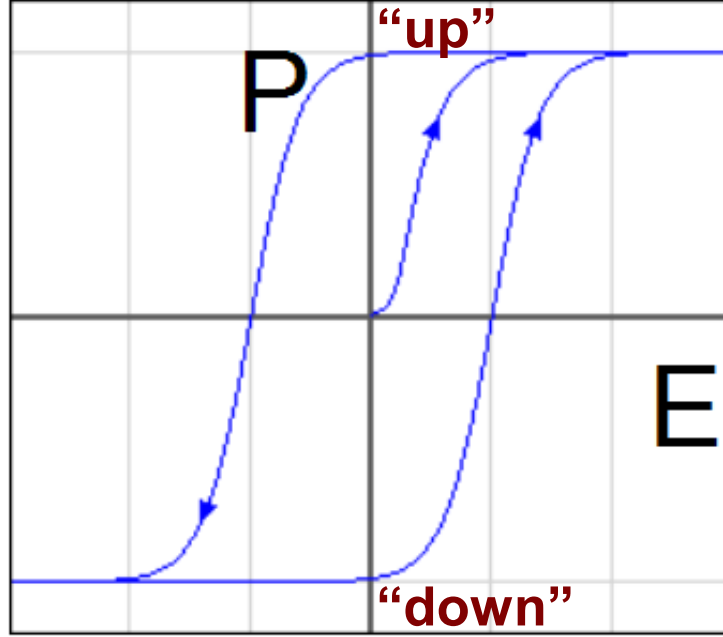
Figure 1.2: Ferroelectric hysteresis loop. Polarization (P) dependence on the applied electric field (E). When electric field is first applied, the ferroelectric material becomes polarized, and it stays polarized even when the field is turned off. Switching between two spontaneous polarization "up" and "down" states is achieved by inverting the sign of the applied electric field.

calculations on infinite ferroelectric crystals with periodic boundary conditions. The "modern theory of polarization" provides another way how to define $\vec{P}$, and its advantage lies in connecting the definition of polarization directly to what is measured experimentally [39, 40],

$$\Delta \vec{P} = \int dt \frac{1}{V_{cell}} \int_{cell} d\vec{r} j(\vec{r}, t). \tag{1.2}$$

Here, the polarization is expressed as an integrated current density, and is directly connected to the electrical and optical means of measuring polarization. Notice that only difference in the electric polarization $\Delta \vec{P}$ is defined via Eq. (1.2). This is exactly half of the difference between the two spontaneous polarization ["up" and "down"] states that is obtained experimentally from, for example, the hysteresis loop measurements [see Fig. 1.2].

1.2.2 Multiferroic

Next, we define a ferromagnet, ferroelastic, and finally a multiferroic material (multiferroic). A ferromagnet is a material where, similarly to a ferroelectric, switching between two or more spontaneous magnetization states is achieved by applying a magnetic field. A ferroelastic exhibits spontaneous strain. A multiferroic is a material in which two or all three of ferroelectricity, ferromagnetism and ferroelasticity occur in the same phase [33, 41]. We will be mostly interested in so called magnetoelectric multiferroics [multiferroics from now on] that exhibit spontaneous polarization and spontaneous magnetization simultaneously.

1.2.3 Perovskites
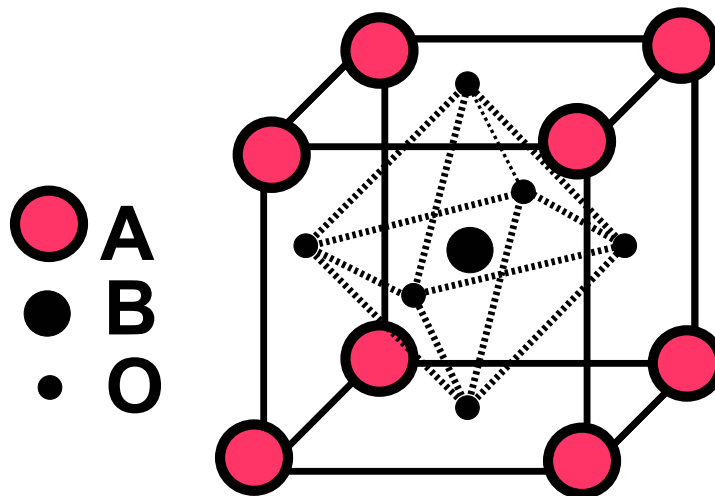
Figure 1.3: Ideal cubic perovskite structure [space group Pm$\bar{3}$m]: A site cations occupy corners of the cube, while typically smaller B site cations occupy center of the cube. Six oxygens O form an octahedron around the B site cation [shown by dashed lines].

Typical examples of ferroelectric, and also multiferroic materials are perovskite oxides. This is a very large family of composition ABO_3 [see Fig. 1.3], where A and B each represent a cation element or mixture of two or more such elements or vacancies. We will see that choosing a magnetic B site cation leads to a possibility of an antiferromagnetically, or ferromagnetically ordered

perovskite, and in general the combined ferroelectric and magnetic properties can lead to a multiferroic perovskite-based system [see Chapter 4]. In this section, we describe electric and magnetic properties of a few bulk perovskites that we study in more detail in the form of either bulk [see Chapters 3 and 4], thin film [see Chapter 2], or superlattice [see Chapter 4] in the next Chapters.

Before we describe individual systems, let us first point to a useful quantity, the Goldschmidt tolerance factor,

$$t = \frac{r_A + r_O}{\sqrt{2}(r_B + r_O)}, \tag{1.3}$$

where r_A, r_B and r_O are ionic radii of A, B cations and O anion, respectively. Goldschmidt has shown that the perovskite structure is formed when $t \approx 1$. In general, when $t > 1$, the B atom is small and the structure develops a small polar distortion, as in BaTiO$_3$. When $t < 1$, the A atom is small, and the oxygens move towards the "empty" space such that the corner-shared oxygen octahedra rotate, as in SrTiO$_3$, or BiFeO$_3$ [38].
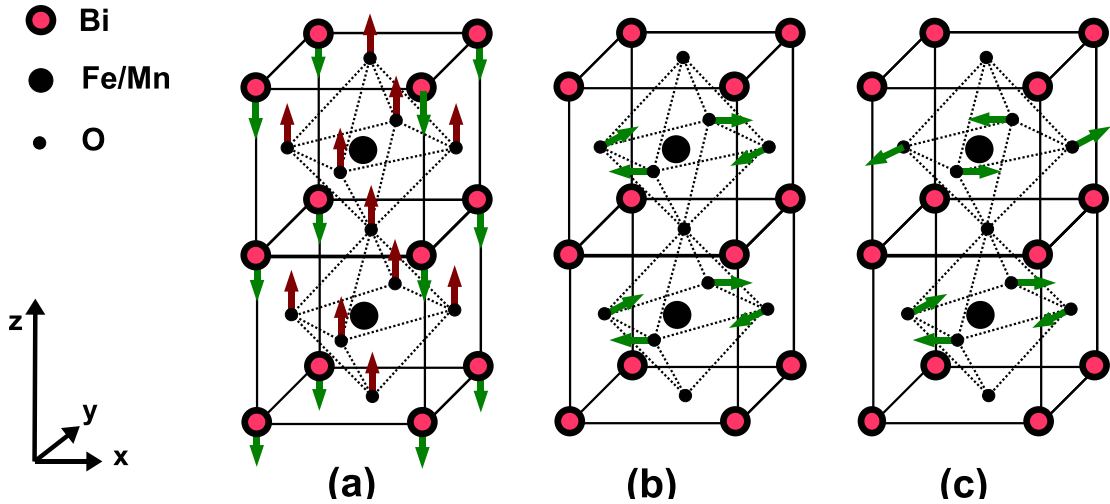
Figure 1.4: Common structural distortions of the cubic perovskite cell [of a BiFe(Mn)O$_3$ system, see Chapter 4]: (a) Polar distortion with relative shift of Bi and Fe/Mn cations with respect to O anions along the z-axis [$\Gamma_4^-(z)$], (b) + (in-phase) rotations of the oxygen octahedra [dashed lines] about the z-axis [$M_3^+(z)$], (c) − (out-of-phase) rotations of the oxygen octahedra [dashed lines] about the z-axis [$R_4^+(z)$].

Recently, Stokes has classified three typical unstable structural distortions of the ideal cubic

perovskites [42]: (i) polar distortion of cations with respect to anions that leads to an electric dipole moment and to the electric polarization, and two non-polar rotational distortions (ii) + rotations of the oxygen octahedra, that is all rotations about a given axis are in phase, or (iii) − rotations of the oxygen octahedra, that is sense of rotations alternates along the rotation axis, as is sketched in Fig. 1.4. By freezing in these modes, or combinations of these modes, we generate various perovskite structures that correspond to different structural space groups.

BaTiO$_3$
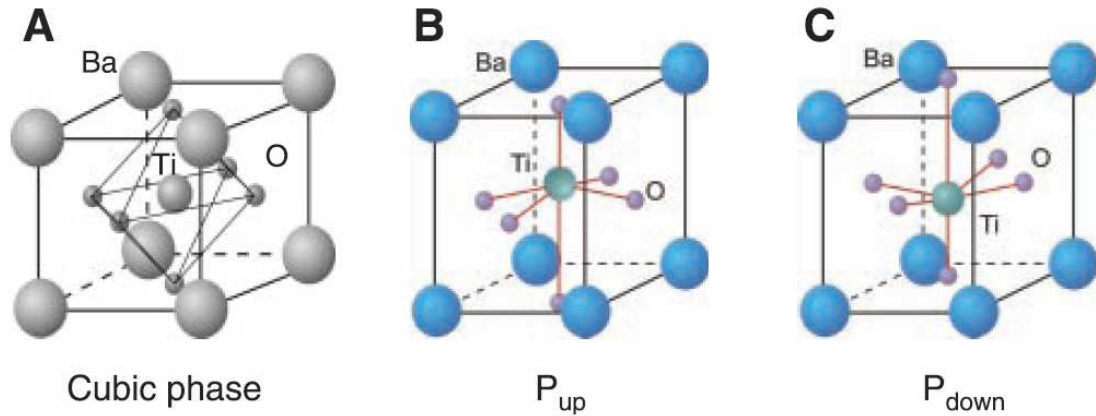
Figure 1.5: Crystal structure of the perovskite ferroelectric BaTiO$_3$. (A) High temperature, paraelectric, cubic phase Pm$\bar{3}$m. (B and C) Room temperature, ferroelectric, tetragonal P4mm phases. Displacing Ti cation with respect to O anions leads to a nonzero electric dipole moment and breaks the inversion symmetry of the cubic phase. Two symmetry equivalent "up" and "down" polarization variants are shown. The atomic displacements are scaled to be clearly visible [18].

Barium titanate (BaTiO$_3$) is a typical ferroelectric perovskite. It has a paraelectric cubic perovskite structure [Pm$\bar{3}$m] at high temperatures, and it undergoes a series of phase transitions: first to a ferroelectric tetragonal P4mm phase [generated by polar $\Gamma_4^-(z)$ mode] at 393 K [as shown in Fig. 1.5], then to a ferroelectric orthorhombic Amm2 phase [generated by polar $\Gamma_4^-([110])$ mode] at 278 K, and finally to a ferroelectric rhombohedral R3m phase [generated by polar $\Gamma_4^-([111])$ mode] at 183 K, see Fig. 1.6. The first transition is of a second order, while the latter two are first order transitions [see Sec. 1.2.4]. A phenomenological order-disorder model best describes

the sequence of these phase transitions as follows. As we already mentioned above, because the B cation (Ti) is small [$t > 1$, see Eq.(1.3)], it always displaces towards the "empty" space along one of the cube diagonals. At high temperature, all possible [111] directions are allowed, therefore the averaged displacement is zero [paraelectric Pm$\bar{3}$m phase]. At low temperature, the displacements all adopt either the same orientation [giving the rhombohedral R3m symmetry], or two, or four preferred [111] directions [giving the orthorhombic Amm2, or tetragonal P4mm symmetry, respectively] [38, 36].

Spontaneous polarization arises from breaking inversion symmetry of the cubic perovskite paraelectric phase. This is done by displacing the Ti cation with respect to O anions, which leads to a nonzero electric dipole moment. The displacement is along [111], [110], or [001] direction in the ferroelectric R3m, Amm2, or P4mm BaTiO$_3$ phase, with values of polarizations satisfying the $\sqrt{3} : \sqrt{2} : 1$ ratio, respectively [36, 38]. For example, the polarization in the tetragonal ferroelectric phase is about $27\mu C/cm^2$. Here, the Ti cation displaces either "upwards" or "downwards" with respect to the oxygen anions, leading to two polarization P_{up} or P_{down} symmetry equivalent states, Fig. 1.5. As we discussed already in Sec. 1.2.1, it is possible to switch between these two states by applying an electric field.

SrTiO$_3$ and KTaO$_3$

Strontium titanate (SrTiO$_3$) is an "incipient ferroelectric" [43]. It remains paraelectric down to zero temperatures, but it lies close to a paraelectric-ferroelectric transition as we describe in Sec. 1.3.2 [see Fig. 1.12], and in Chapter 3. First principles calculations show that quantum fluctuations suppress the ferroelectricity in SrTiO$_3$ [44–46]. SrTiO$_3$ [$t < 1$, see Eq.(1.3)] undergoes a structural phase transition from the paraelectric cubic Pm$\bar{3}$m to the paraelectric tetragonal I4/mcm phase at about 110 K [47], where the oxygen octahedra rotate around cartesian axis in an antiferrodistortive $R_4^+(z)$ mode.

Potassium tantalate (KTaO$_3$) is also an "incipient ferroelectric". It does not undergo any structural transition, and it remains cubic paraelectric Pm$\bar{3}$m down to low temperatures [48]. As we

discuss in Chapter 3, $KTaO_3$ lies deeper in the paraelectric phase than $SrTiO_3$, and away from the quantum paraelectric-ferroelectric transition, because its zero temperature dielectric constant is much lower than the dielectric constant in $SrTiO_3$ [43, 49].

$Ba_xSr_{1-x}TiO_3$
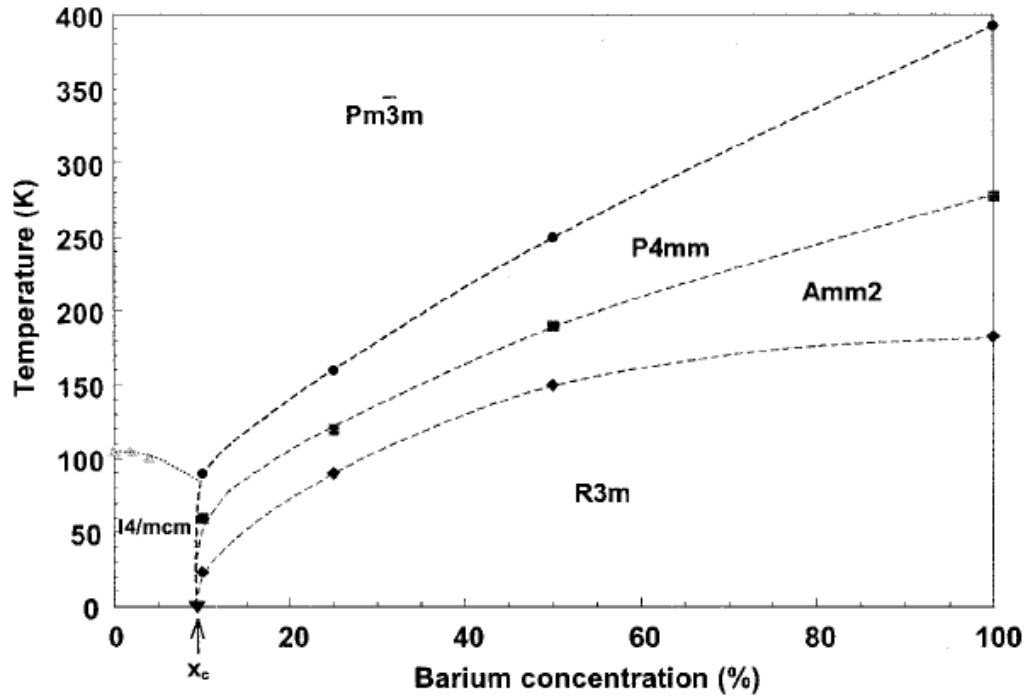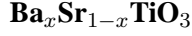
Figure 1.6: Critical temperature vs. concentration phase diagram of $Sr_{1-x}Ba_xTiO_3$, deduced from the x-ray and neutron-diffraction studies [50].

Another possibility how to create a new perovskite system is to substitute A, or B site cation. For example, the isoelectronic A site substitution of Ba^{2+} by Sr^{2+} results in $Ba_xSr_{1-x}TiO_3$ (BST), Fig. 1.6. As more Sr is introduced, the ferroelectric transition temperatures are lowered, and the value of the spontaneous polarization decreases inside each ferroelectric phase [50].

BiFeO$_3$

Bismuth ferrite (BiFeO$_3$) is a room temperature ferroelectric, and a promising lead-free material for room temperature electronic applications [51]. The spontaneous polarization of BiFeO$_3$ is large, about $60 - 100 \mu C/cm^2$ [Refs. [52–56]], and is comparable to the polarization of the widely used and technologically important ferroelectric PZT.
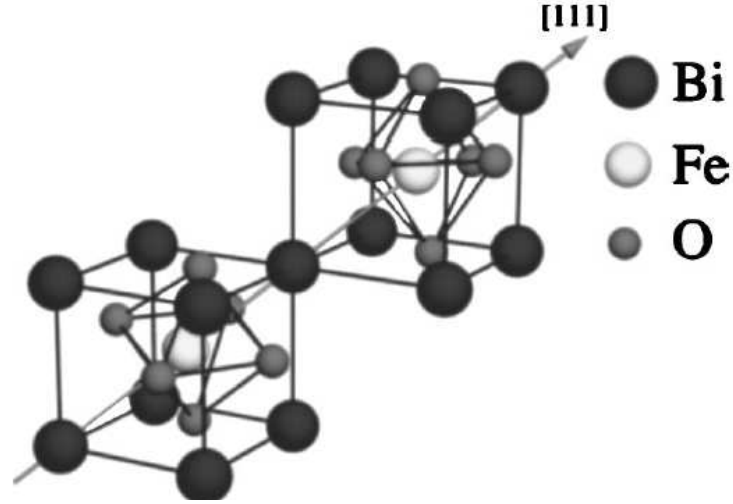
Figure 1.7: Ground state structure of R3c BiFeO$_3$: counter-rotations of the oxygen octahedra [R_4^+([111])] and polar ionic displacements [Γ_4^-([111])] are along the body diagonal [111] axis [56].

We show the ground state structure of BiFeO$_3$ in Fig. 1.7. It has rhombohedral R3c symmetry, where the oxygen octahedra rotate alternatively clockwise and couterclockwise along the body diagonal [111] direction [rotational R_4^+([111]) mode], and where Bi^{3+} and Fe^{3+} cations displace with respect to O^{2-} anions in the structure along the [111] direction [polar Γ_4^-([111]) mode]. Again, because the Goldschmidt tolerance factor $t < 1$ [see Eq.(1.3], the oxygen octahedra rotations are favored. The polar mode is responsible for ferroelectric behavior of BiFeO$_3$, and for the onset of spontaneous polarization that accordingly points along the body diagonal [111] direction. Ferroelectricity in BiFeO$_3$ has a different origin than that of BaTiO$_3$ [see Sec. 1.2.3] [36]. It is driven by stereochemically lone-pair-active Bi^{3+} cations that off-center toward neighboring oxygen anions, and this off-centering is stabilized by a covalent bond formation between Bi and O [57].
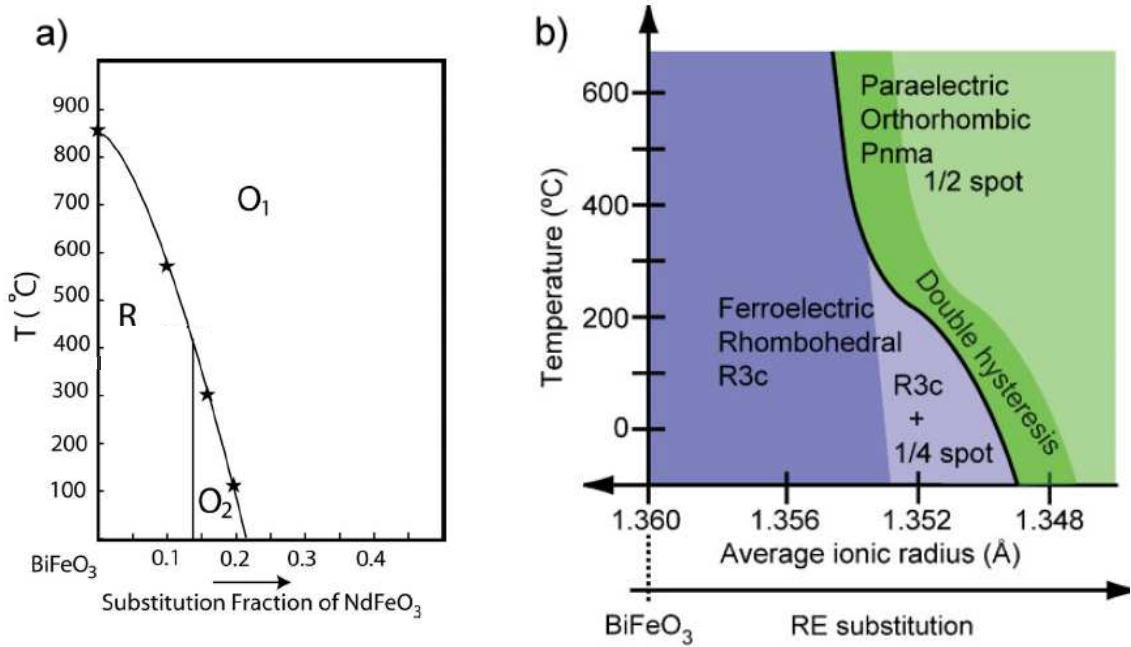
Figure 1.8: (a) Critical temperature vs. $NdFeO_3$ concentration phase diagram of $Bi_{1-x}Nd_xFeO_3$. Solid lines correspond to the structural phase transitions, where R refers to the rhombohedral R3c, and O1 and O2 refer to the $GdFeO_3$-type Pnma and $PbZrO_3$-type Pbam structures, respectively [61]. Notice that pure $BiFeO_3$ undergoes a transition from the R3c to Pnma phase at 1100 K. (b) Proposed phase diagram for rare-earth (RE) substituted $BiFeO_3$, $Bi_{1-x}RE_xFeO_3$. The black line represents the structural phase boundary between the rhombohedral R3c (in blue) and the orthorhombic Pnma (in green) structural phases. At lower temperature side, the region in light blue corresponds to the coexistence of R3c and Pbam phases. Double hysteresis loop behavior (in dark green) is observed close to the structural transition [60].

$BiFeO_3$ undergoes a phase transition from the ferroelectric rhombohedral R3c to a paraelectric orthorhombic Pnma phase at Curie temperature 1100 K [58]. The paraelectric Pnma phase is also a high pressure phase of $BiFeO_3$ [59]. We show that Pnma lies very close, only $14 meV$ per perovskite cell, above the R3c ground state of $BiFeO_3$ [60]. Therefore, perturbations such as the external pressure, or a rare-earth [RE=Sm^{3+}, Gd^{3+}, Dy^{3+}, Nd^{3+}] A site isoelectronic substitution on place of Bi^{3+} in $Bi_{1-x}RE_xFeO_3$ are enough to stabilize this phase, Fig. 1.8.

In $Bi_{1-x}RE_xFeO_3$, the substitution of smaller RE cation on place of Bi cation results in suppression of ferroelectricity [which is driven by the stereochemically active Bi^{3+}], and because the

Goldschmidt tolerance factor [see Eq.(1.3)] decreases, more "space" is given to the oxygen octahedra to rotate in a new rotational $R_4^+([110])$ and $M_3^+([001])$ (Pnma) pattern [62]. Double hysteresis loops are observed in $Bi_{1-x}RE_xFeO_3$ close to the R3c-Pnma transition [see dark green region in Fig. 1.8 (b)]. We recognize that this behavior is due to an electric-field-induced transition between the paraelectric Pnma and ferroelectric R3c phases, rather than arising from true antiferroelectric character of $Bi_{1-x}RE_xFeO_3$. Finally, because the R3c-Pnma phase transition is of the first order, structural changes at the transition are accompanied by high value of the piezoelectric coefficient of $Bi_{1-x}RE_xFeO_3$, which becomes comparable to the technologically used PZT [60].

In $BiFeO_3$, ferroelectricity and magnetism coexist at room temperature. Bulk $BiFeO_3$ has a G-(rocksalt)-type antiferromagnetic (AFM) ordering of the Fe magnetic moments. In addition, a spiral spin structure with incommensurate long-wavelength period of $\sim 620\mathring{A}$ is superimposed on this magnetic ordering [63]. Its Neel temperature is 643 K [64]. It has been shown that a net magnetization arises from the Dzyaloshinskii-Moriya-type [65, 66] weak ferromagnetism [67], where the spin-orbit coupling plays a crucial role in that it forces the Fe magnetic moments to cant, which results in a small net magnetization value. Such small magnetization has been indeed measured in $BiFeO_3$ thin films, where the spiral spin structure is suppressed due to the presence of the substrate [54]. $BiFeO_3$ is therefore known as a room temperature multiferroic. Because its ferroelectric behavior originates from the Bi-O interaction, and the magnetic ordering and magnetization from the Fe magnetic moments, its magnetoelectric coupling is weak [36, 68].

$BiMnO_3$

Bulk bismuth manganite ($BiMnO_3$) has a Goldschmidt tolerance factor $t < 1$ [see Eq. (1.3)] close to $BiFeO_3$, because of the similarity between the Fe and Mn transition metals, and therefore favors oxygen octahedra rotations. However, because Mn is Jahn-Teller active, the structure becomes highly distorted [36, 69, 70]. $BiMnO_3$ has centrosymmetric monoclinic structure with the space group C2/c [71, 72], and thus zero spontaneous polarization [57]. We mention that there have been several experiments on $BiMnO_3$, and some of them show ferroelectric hysteresis loops [73], or
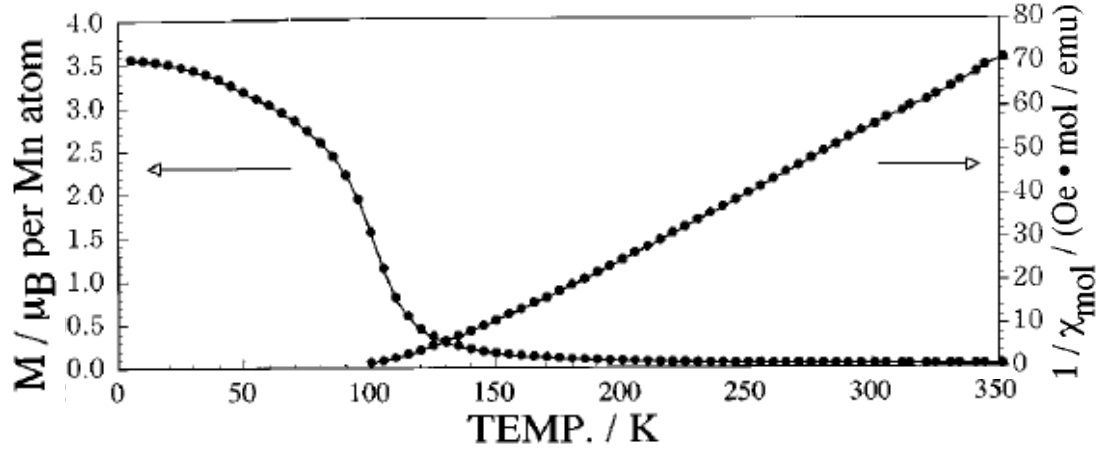
Figure 1.9: Temperature variation of magnetization M and inverse of molar magnetic susceptibility χ_{mol} of BiMnO$_3$ measured at 1T [75].

optical second-harmonic generation [74]. Therefore, further measurements are encouraged in order to justify the BiMnO$_3$ ground state. BiMnO$_3$ is also known as a ferromagnet with Curie temperature 105 K, and with a low tepmerature magnetic moment $3.6\mu_B$ per Mn [75–78], Fig. 1.9.

1.2.4 Phase Transitions - Landau Theory

We mentioned that a ferroelectric undergoes a phase transition from the ferroelectric phase with nonzero spontaneous polarization to a paraelectric phase with zero spontaneous polarization at a critical temperature T_c, see Fig. 1.1. Similarly, a phase transition occurs between the ferromagnetic [or antiferromagnetic] and paramagnetic phase, and we discussed examples of these transitions in perovskites in Sec. 1.2.3. Here, we use phenomenological Landau theory to describe these phase transitions, and we focus our attention on the ferroelectric-paraelectric transitions. Similar results can be obtained for magnetic transitions, and we refer the reader to find details of these derivations elsewhere [13, 79].

The basic idea of Landau theory is that the free energy can be expressed as a series expansion of polarization [the order parameter] close to the phase transition. In addition, symmetry constraints

are postulated on the expansion. In particular, we want the free energy to be invariant under the inversion symmetry, $\vec{P} \rightarrow -\vec{P}$. Because the two symmetry equivalent $\vec{P}$ ("up") and $-\vec{P}$ ("down") states have the same energy [see Fig. 1.1], we allow only even terms in the power series of the polarization,

$$G(P) = \frac{1}{2}aP^2 + \frac{1}{4}bP^4 + \frac{1}{6}cP^6 - EP. \tag{1.4}$$

Here, we truncate the power series at the sixth term, and the last term is the coupling energy between electric field and polarization, $\vec{E} \cdot \vec{P}$, introduced in Sec. 1.2.1. For simplicity, we assume bulk ferroelectric with spatially uniform polarization [a monodomain sample]. We note that we choose the origin of the free energy for the free unpolarized, unstrained crystal to be zero.

The condition for finding the system in its equilibrium state is $\frac{\partial G(P)}{\partial P} = 0$. This condition leads to an equation for the spontaneous polarization, $aP + bP^3 + cP^5 = E$. In most ferroelectrics, the linear dielectric susceptibility, defined as $\chi \equiv \frac{\partial P}{\partial E}\big|_{P=0}$, is observed to follow the Curie-Weiss behavior at reasonably high temperatures [see Fig. 1.9] [79],

$$\chi = \frac{C}{T - T_0}. \tag{1.5}$$

From Eq. (1.4) and Eq. (1.5), we find that $\chi = \frac{1}{a}$, and the temperature dependent coefficient in the expansion of the free energy $G(P) \equiv G(P, T)$, a, vanishes at the phase boundary at $T = T_0$,

$$a \sim T - T_0. \tag{1.6}$$

Let us now distinguish two types of transitions: a first-order (discontinous) and a second-order (continous) phase transition. A first-order transition leads to a finite jump in the dielectric susceptibility and the spontaneous polarization at the ferroelectric-paraelectric phase boundary at $T_c \neq T_0$. It is also accompanied by a finite change in the volume between the ferroelectric and paraelectric phase, and by a latent heat. In a second-order phase transition, the spontaneous polarization smoothly decreases until it vanishes at the critical temperature $T_c = T_0$, where also the dielectric

susceptibility diverges [see Eq. (1.5)]. It is convenient to use the sign of the Landau coefficient b to distinguish the order of the phase transition: it can be shown that $b < 0$ corresponds to the first, while $b > 0$ corresponds to the second order phase transition.

There are also two types of transitions in ferroelectrics: a displacive, and an order-disorder type of transition. The latter has been already described in Sec. 1.2.3 on the example of ferroelectric $BaTiO_3$, where the spontaneous polarization always exists, but has a random orientation above the critical temperature T_c resulting in zero net polarization. On the contrary, the polarization, and the displacements of ions that contribute to the polarization, completely vanish above T_c in a displacive ferroelectric, such as, for example, in strained $SrTiO_3$ [see Sec. 1.3.1, or Chapters 2 and 3].

Finally, let us discuss when the Landau theory breaks down. Non-uniform charge distribution in a ferroelectric leads to a spatially dependent polarization $\vec{P}(\vec{r})$, and in general to a ferroelectric domain structure. Therefore to fully describe a paraelectric-ferroelectric transition, one has to allow spatial fluctuations of the order parameter, polarization, which lead to an additional Ginzburg term in the free energy [Eq. (1.4)], $G_G \sim \int d^d\vec{r}\,(\nabla P(\vec{r}))^2$. However, when the fluctuations of the polarization become too large, and comparable to the polarization value itself, the Landau mean field theory breaks down. This criterion is known as the Ginzburg criterion, and one can show that the Landau-Ginzburg theory is valid for systems sitting above their upper critical dimension, $d > 4$. We will see in Chapter 3 that this is the case of bulk quantum paraelectrics [see Sec. 1.3.2] that sit close to their quantum paraelectric-ferroelectric transition at very low temperatures.

For $d = 3$, the Ginzburg [or Levanyuk-Ginzburg] criterion can be written in the form

$$\mathcal{A}\frac{1}{(\Delta C_v)^2\, \xi_0^6} << |\frac{T - T_0}{T_0}|, \tag{1.7}$$

where ΔC_v is the change in the specific heat at the phase transition, $\mathcal{A} \sim 1$ is a constant, and ξ_0 is the range of polarization-polarization interaction, which is typically large in ferroelectrics. This criterion is therefore satisfied over a broad temperature range, and the Landau [or Landau-Ginzburg] theory works well in the vicinity of the paraelectric-ferroelectric transition [13].

1.3 Discussion of Thesis Topics

1.3.1 Challenge of Ferroelectric Films
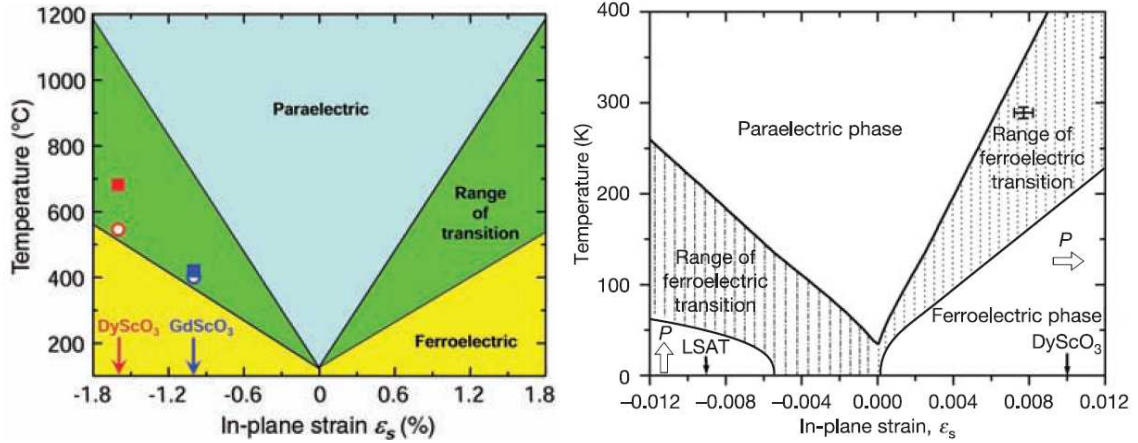
Figure 1.10: (left) Expected T_c of (001) BaTiO$_3$ under biaxial in-plane strain (ϵ_s), based on thermodynamic analysis. The green region represents the range (error bars) in the predicted T_c resulting from the spread in reported property coefficients for BaTiO$_3$ that enter into the thermodynamic analysis. The data points show the observed ϵ_s and T_c values of coherent BaTiO$_3$ films grown by molecular beam epitaxy (MBE) on GdScO$_3$ (blue circle) and DyScO$_3$ (red circle) substrates and by pulsed laser deposition (PLD) on GdScO$_3$ (blue square) and DyScO$_3$ (red square) substrates [14]. (right) Expected shift in T_c of (100) SrTiO$_3$ with biaxial in-plane strain, based on thermodynamic analysis. The arrows indicate the predicted direction of the polarization for strained SrTiO$_3$: in-plane for biaxial tensile strain and out-of-plane for biaxial compressive strain. The ϵ_s values for SrTiO$_3$ fully constrained (commensurate) to the lattice constants of (LaAlO$_3$)$_{0.29}$×(SrAl$_{0.5}$Ta$_{0.5}$O$_3$)$_{0.71}$ (LSAT) and (110) DyScO$_3$ substrates are indicated by the positions of the corresponding arrows. The cross shows the observed T_c shift of a 500-Å-thick SrTiO$_3$ film epitaxially grown on (110) DyScO$_3$ [15].

Ferroelectric films can show tremendously different behavior than bulk. We illustrate this difference on two ferroelectric BaTiO$_3$ and SrTiO$_3$ thin films grown on different substrates [GdScO$_3$, DyScO$_3$, or (LaAlO$_3$)$_{0.29}$×(SrAl$_{0.5}$Ta$_{0.5}$O$_3$)$_{0.71}$ (LSAT)] in Fig. 1.10. The temperature axis in the figure denotes the critical temperature T_c, which dramatically raises by several hundreds of degrees when the films are strained [14, 15]. Notice that even though bulk SrTiO$_3$ is paraelectric down to zero temperatures [see Sec. 1.2.3], SrTiO$_3$ thin film grown on DyScO$_3$ displays room temperature ferroelectricity [15].
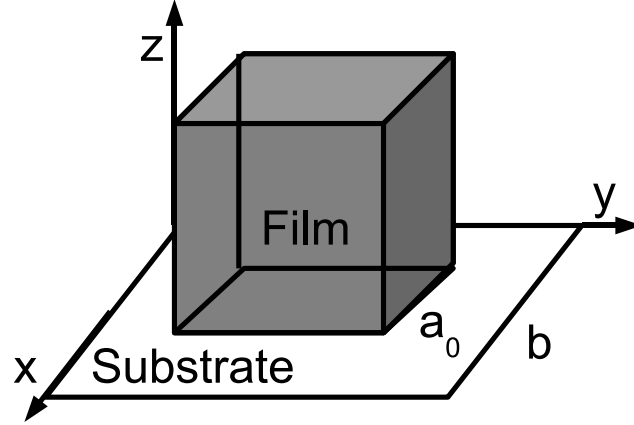
Figure 1.11: Schematic of a ferroelectric thin film (unit cell) epitaxially grown on a substrate with in-plane lattice constants a_0 and b, respectively. The film stretches in the in-plane direction so that its lattice constant matches to the substrate and creates an in-plane [tensile] strain ϵ_s, while it relaxes its out-of-plane lattice constant.

In order to understand this effect, we need to look at the mechanical boundary conditions postulated by the substrate. In particular, the in-plane strain that acts on the ferroelectric thin film [horizontal axis in Fig. 1.10] arises from a lattice mismatch between the film and the substrate. Schematically, this situation is sketched in Fig. 1.11, where the film in-plane lattice constant a_0 is smaller than the lattice constant b of the substrate. The film has a tendency to stretch so that its lattice constant matches the lattice constant of the substrate, while it relaxes in the out-of-plane direction. Value of the misfit bi-axial in-plane strain is then expressed as

$$\epsilon_s = \frac{b - a_0}{b}, \tag{1.8}$$

where $\epsilon_s > 0$ corresponds to a tensile, while $\epsilon_s < 0$ corresponds to a compressive strain. We use Landau theory in Chapter 2 to show that the critical temperature indeed raises with strain.

Very thin films have a tendency to be strained uniformly by an elastic deformation, while thick films relax the strain by forming dislocations, and the strain becomes zero in the bulk limit far from the substrate [80]. We address the question of how misfit dislocations are distributed within the film in Chapter 2, where we compare a segregated strain model with misfit dislocations residing in a thin

buffer layer close to the substrate and the rest of the film homogeneously strained, with a model where uniform distribution of the dislocations leads to an inhomogeneous strain in the film [81].

The effect of strain on polarization $\vec{P}$ is encorporated in the piezoelectric coupling d_{ijk},

$$d_{ijk} = \frac{\partial P_i}{\partial \epsilon_{jk}}, \tag{1.9}$$

where $\{i, j, k\} \in \{x, y, z\}$, and the strain tensor $\epsilon_{jk} = \frac{1}{2}\left(\frac{\partial u_j}{\partial r_k} + \frac{\partial u_k}{\partial r_j}\right)$ is defined as by how the displacement $\vec{u}$ of a point in the solid varies with position $\vec{r}$. We note that $\epsilon_{xx} = \epsilon_{yy} = \epsilon_s$ in Eq. (1.8).

Similarly, a flexoelectric coupling tensor μ between the strain gradient and polarization can be introduced in inhomogenously strained films [81, 82],

$$P_l = \mu_{ijkl}\frac{\partial \epsilon_{ij}}{\partial r_k}. \tag{1.10}$$

The flexoelectric effect was depicted to be responsible for an observed broadening and suppression of the dielectric susceptibility in thin ferroelectric films [81]. We note that the dielectric susceptibility diverges at the paraelectric-ferroelectric phase boundary in a second order phase transition of a bulk, and therefore understanding this dramatic change in the characteristic dielectric behavior is necessary for any potential thin film ferroelectric applications. In fact, this critical observation motivates our research in Chapter 2, where we discuss possible origin of the broadening and suppression of many thin-film characteristics. We show that these observed effects can be explained by a simpler model with homogeneous strain in the majority of the film, and our work suggests that further benchtop experiments beyond dielectric measurements are necessary to determine the nature of the underlying strain. We predict a "smoking gun" protocol to test our model.

1.3.2 Ferroelectrics as a Way to Study Quantum Critical Behavior

The Curie-Weiss law [Eq. (1.5)] has been observed to break down at very low temperatures in some perovskites, for example in $BaTiO_3$, $SrTiO_3$, ^{18}O-substituted $SrTiO_3$, or $KTaO_3$, where the

temperature dependence of the dielectric constant [or equivalently the dielectric susceptibility] becomes inversely proportional to temperature squared rather than having linear temperature dependence [30, 32, 83, 84]. We show in Chapter 3 that this change comes from quantum fluctuations of the polarization at low temperatures where quantum effects need to be incorporated, and therefore the classical Landau-Ginzburg description breaks down.

In other words, the main difference is that a ferroelectric at a quantum critical point at zero temperature possesses fluctuations of the polarization on all spatial and temporal scales, whereas a ferroelectric at the classical critical point [or classical paraelectric-ferroelectric phase transition] has fluctuations on all spatial scales only. This can be understood from a formalism that maps a quantum system of dimension d back to a classical system of dimension $d+z$, where z is a dynamical critical exponent [also the temporal direction] defined from the dispersion relation $\omega \sim q^z$. We show in Chapter 3 that $z = 1$ in ferroelectrics, and therefore there is only one temporal dimension.

The main reason why studying ferroelectrics close to their quantum critical point is so intriguing it that now the effective dimension of the quantum ferroelectric system in bulk [$d = 3$] becomes $d + 1 = 4$. This is fascinating because as we discuss in Sec. 1.2.4, $d = 4$ is just the upper critical dimension, and thus we are able to study ferroelectrics below [as effectively two dimensional thin films], at [as bulk], or above the upper critical dimension [with dipole-dipole interactions effectively lifting the dimension of tetragonal phases]. Let us point out that this is not the case in other [magnetic] critical systems where $z > 1$.

In addition, simple theoretical scaling predictions can be compared directly with experiment. We show two measurements on bulk $SrTiO_3$ in Fig. 1.12. Results of the dielectric constant temperature dependence of $SrTi^{16}O_3$ are plotted in the figure on the left, where large dielectric response at low temperatures saturates at $T \sim 4K$ [43]; quantum fluctuations are believed to stabilize the paraelectric phase [44, 46]. On the other hand, when ^{16}O is substituted by ^{18}O, the system becomes ferroelectric at critical temperature $25K$ [peak in the dielectric constant in the figure on the right at atmospheric pressure 1 bar]. As we see in Sec. 1.3.1, application of strain induces ferroelectricity in $SrTiO_3$, and therefore it is not surprising that ^{18}O substitution [yet another perturbation of the
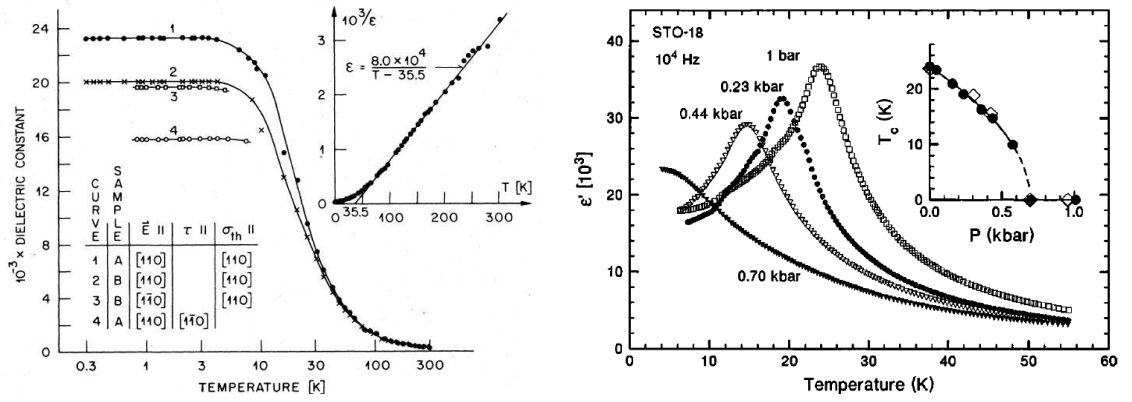
Figure 1.12: (left) Dielectric constants ϵ_{110} and $\epsilon_{1\bar{1}0}$ of the monodomain $SrTiO_3$ samples A and B [σ_{th} is the stress applied by thermal treatment]. Inset: $10^3/\epsilon$ vs. temperature T [43]. (right) The large influence of pressure on the temperature dependence of the dielectric constant $\epsilon'(T)$ in ^{18}O-substituted $SrTiO_3$ leading to the complete suppression of the ferroelectric state. The inset shows the shift of T_c with pressure [30].

perovskite structure] drives ferroelectricity. What is more interesting is that by applying pressure on the ^{18}O-substituted $SrTiO_3$, the critical temperature is tuned continuously to $T = 0$ [see the inset in the figure on the right], thereby making it an ideal setting for the detailed study of a quantum critical point sitting at $\{T_c, p_c\} \equiv \{0K, 0.7kbar\}$. Even though this point sits strictly at zero temperature, we show in Chapter 3 that it has a significant impact on the dielectric properties at a wide range of temperatures and pressures [see Fig. 3.10].

1.3.3 A Designed Multiferroic

We discuss in Sec. 1.1.4 that it is difficult to find a single phase multiferroic material, and that much of attention is given to an artificial design of new materials. Our research is motivated by the latter, with first principles methods [85–87] being an essential tool for the study of promising systems [17, 18, 88, 89].

In Chapter 4, we identify a promising artificially structured perovskite-based system with an unusual heterostructure, an atomic-scale $BiFeO_3$-$BiMnO_3$ nanocheckerboard [see Fig. 4.1]. We

find that the multiferroic nanocheckerboard ground state inherits the desired properties of each constituent material: polar and ferrimagnetic due to $BiFeO_3$ and $BiMnO_3$, respectively [see Sec. 1.2.3]. We also study the effect of arrangement of the magnetic B-site cations [Fe and Mn] on magnetic properties of the $BiFeO_3$-$BiMnO_3$ system, and examine the effect of structural distortion. Our first-principles calculations uncover a magnetostructural effect in the nanocheckerboard where switching between finite and zero magnetization states is possible. Such magnetostructural effect is not observed either in the bulk, or other superlattice structures of the constituent materials. We show that the interesting magnetostructural behavior is linked to quasidegenerate magnetic states of the magnetically frustrated checkerboard geometry, and thus is not restricted only to the $BiFeO_3$-$BiMnO_3$ nanocheckerboard, and we encourage future experiments on different nanocheckerboard systems [90].

1.4 Outline of the Present Work

The rest of this dissertation is organized as follows. In Chapter 2, we study dielectric properties of thin ferroelectric films using phenomenological Landau theory that we introduce in Sec. 1.2.4. In particular, we explain broadening of the dielectric susceptibility as a result of a segregated strain model and an effective bias field in thin ferroelectric films [see Sec. 1.3.1]. In Chapter 3, we focus our attention on how the dielectric properties of bulk quantum paraelectrics change at very low temperatures and high pressures [see Sec. 1.3.2]. Finally, in Chapter 4, we design a new multiferroic system with a novel magnetostructural effect, the $BiFeO_3$-$BiMnO_3$ nanocheckerboard, using first principles methods [see Sec. 1.3.3].

Chapter 2

Modeling the Dependence of Properties of Ferroelectric Thin Film on Thickness

2.1 Introduction

Increasing demands for high-density data storage with ultra-fast accessibility present tremendous challenges. In parallel to the characterization of new materials, important size-dependent effects must be understood to optimize design. This is particularly true for ferroelectric memories, whose nonvolatility and low power consumption make them well-suited for portable applications; [27, 28] their dielectric properties are strongly dependent on electromechanical boundary conditions due to the long-range nature of their underlying electrostatic interactions.

The sensitivity of ferroelectricity to homogeneous strain in bulk perovskite oxides is well-known [91] [see Sec. 1.3.1]. In thin films, the effects of homogeneous misfit strain have been identified [92], studied and controlled to the point that particular systems have been strain-engineered to have spontaneous polarizations significantly larger than those in the bulk [14, 15]. Despite these impressive achievements, several authors [81, 93–95] have suggested that homogenous epitaxial strain cannot qualitatively account for all the observed effects in ferroelectric films. In particular, the thickness-dependence of their dielectric properties has been attributed to defect-induced strain gradients [81, 93]. We explore whether these observed size-effects are also consistent with an alternative scenario where the majority of each ferroelectric film is homogeneously strained. Our phenomenological study indicates that thickness-dependent dielectric measurements are insufficient to determine the presence, or absence of underlying inhomogeneous strain and we suggest further benchtop experiments that will resolve this issue.

In well-screened coherent epitaxial ferroelectric thin films, uniform polarization is energetically favored. Lattice mismatch between the film and the substrate is a key source of macroscopic strain

in these systems [22, 92]. For very thin films, the energy cost for homogeneously straining the film to match the substrate is less than that associated with the introduction of stress-relieving defect structures at the interface. However in thicker films, such misfit dislocations form and produce strain gradients [22, 80, 93, 96, 97]; threading dislocations and point defects are additional sources of inhomogeneous strain.

In planar ferroelectric films, inhomogeneous strain can affect the ferroelectric transition through both smearing and through its coupling to the polarization. Such flexoelectric coupling of strain gradients to the polarization has been the topic of much recent interest [81, 82, 98], particularly as it has been suggested that flexoelectric effects are enhanced by large dielectric coefficients [99]. Recently, it has been argued that such strain and/or stress gradients are crucial for the modeling of thickness-dependent dielectric properties of ferroelectric films. [81, 93] Here, we propose an alternative model: that the misfit dislocations reside within a thin buffer layer next to the interface; the majority of the film, which is relatively defect-free, is then homogeneously strained. [100] In our phenomenological treatment, we also include a bulk anisotropy [95] in the form of an effective field, [101] possibly due to asymmetry of the electrodes and/or to the thin buffer layer. We model the thickness-dependent dielectric properties in two different types of ferroelectric films, and compare our results with experiment and with first-principles calculations whenever possible. Finally, we discuss a benchtop "smoking gun" probe to distinguish our segregated strain scenario with that of inhomogeneous strain in ferroelectric thin films.

The structure of this chapter is as follows. In Sec. 2.2, we review the experiments that motivate this study and their implications for any descriptive model. Details of our phenomenological Landau approach are presented in Sec. 2.3, with specific discussion of the appropriate boundary conditions and depolarization effects. In Sec. 2.4 we present our main results for films of two specific materials, with comparison to previous findings whenever possible and predictions for future measurements. The implications of our model and our results are discussed in Sec. 2.5. We end with a summary (Sec. 2.6) and with ideas for future work.

2.2 Experimental Motivation

Broadening of the temperature-dependent permittivity in thin films near the paraelectric-ferroelectric transition is reported by several experimental groups; [102–107] this observed smearing, accompanied by an overall reduction in its magnitude, is more pronounced with decreasing film thickness. Careful measurements on free-standing ferroelectric lamellae yield bulk-type dielectric responses, suggesting interfacial effects as the source of these thickness-dependent effects. [108] A second related observation is that there is a clear separation of temperature scales associated with the onset of reversible spontaneous polarization and the maximum of the dielectric constant in thin ferroelectric films. [81]
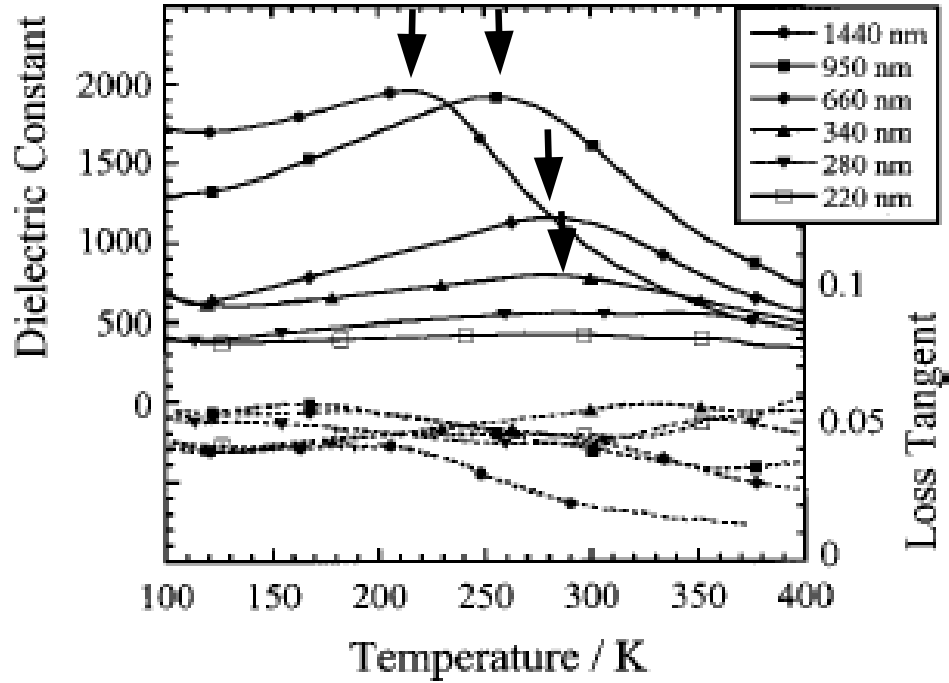
Figure 2.1: Relative permittivity (dielectric constant) as a function of temperature $[\epsilon(T)]$ for $(Ba, Sr)TiO_3$ (BST) films of different thicknesses grown on $SrRuO_3/MgO$ (SRO) substrates [106] where the $\epsilon_{max}(T)$ at temperature T_{max} is indicated with an arrow.

In Fig. 2.1, we display relative permittivity measurements done on $(Ba,Sr)TiO_3$ (BST) thin films grown on $SrRuO_3$ (SRO). [106] The measurements show suppression of the relative permittivity

with decreasing film thickness. As the film thickness decreases to 340 nm, the temperature associated with the maximum of the permittivity (T_{max}) appears to saturate at about 300 K, with T_{max} for the two thinnest films not being clearly discernable. As we will discuss in Sec. 2.4, this is consistent with the prediction of our model that there should be a maximum in $T_{max}(l)$ at a thickness $l = l^*$; from the data in Figure 2.1 we estimate $l^* < 340$ nm in BST films grown on SRO.

In ferroelectric films, in contrast with their bulk counterparts, there is an observed distinction [81] between T_{max} and T_{ferro}, the temperature where polarization becomes switchable. This separation of temperature-scales and the permittivity broadening discussed earlier are both features characteristic of dielectric behavior in an applied bias field [101]; the latter could be due to a real charge distribution or it could result from another physical effect [95] that breaks the symmetry $P \to -P$. For example, it has been noted [81] that flexoelectric coupling, known to increase near a ferroelectric transition [82], implies a spatially-varying effective field term due to the underlying inhomogeneous strain [81]. The resulting phenomenological model successfully reproduces key thickness-dependences of the dielectric properties [81]. Here, we ask whether these experimental trends are indeed proof of underlying strain inhomogeneities, or whether they may be consistent with another strain profile.

2.3 Landau Theory

We model the thickness-dependent properties of strained ferroelectric films using a Landau approach [13, 91], where all misfit dislocations are assumed to reside within a thin buffer layer of size $l_B << l$, where l is the film thickness (e.g., Fig. 2.2); this is in contrast to other approaches where these defects are assumed to be roughly uniformly distributed within the film [93]. Elastic relaxation then occurs so that there is homogeneous strain in the film except for the buffer layer (e.g., Fig. 2.3). Recent X-ray diffraction experiments [106] support previous suggestions [109] that the in-plane film strain u_l [we change the notation from ϵ_s in Eqs. (1.8) and (1.9) to u_l so that ϵ is attributed to the dielectric constant] decreases with increasing thickness (l) of the overall films; furthermore the observed thickness-dependent strain fits an exponential form [106, 109] very well. Therefore in our
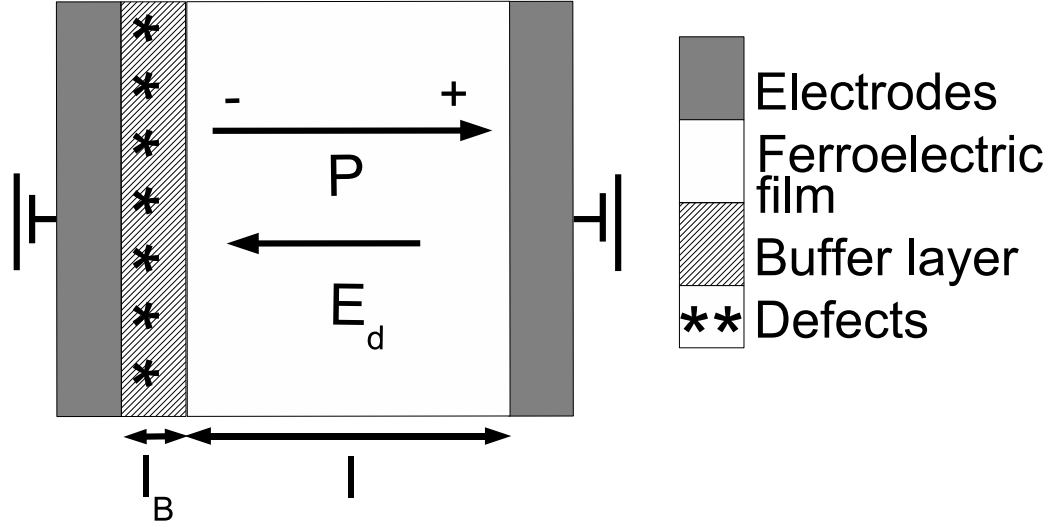
Figure 2.2: A schematic of the planar ferroelectric capacitor under consideration, with the key length scales and regions clearly demarcated. Note that the mismatch defects are segregated in a buffer layer of thickness l_B on the substrate, and that the polarization and strain are homogeneous in the majority of the film. Incomplete charge compensation at the ferroelectric-electrode interfaces results in a residual depolarization field, as shown.

segregated strain approach, thin films experience homogeneous film strain that decreases exponentially with their overall thickness l; more specifically we model this thickness-dependent in-plane film strain as

$$u_l = u_m e^{-l/l_c}, \quad u_m = (b - a)/b, \tag{2.1}$$

where l_c is a characteristic length scale of the strain relaxation, and a and b refer to the in-plane lattice parameters of the film (bulk value) and the substrate, respectively [100]. We emphasize that our values of l_c are determined from X-ray diffraction [106, 109] for films of a range of thicknesses. We note that these values of l_c are comparable to the film thicknesses of interest ($l_c \sim l$), resulting in a non-trivial thickness-dependence of the strain-related properties. More generally, we remark that the segregated strain approach described here has been used in modeling epitaxially strained

Segregated Strain Model
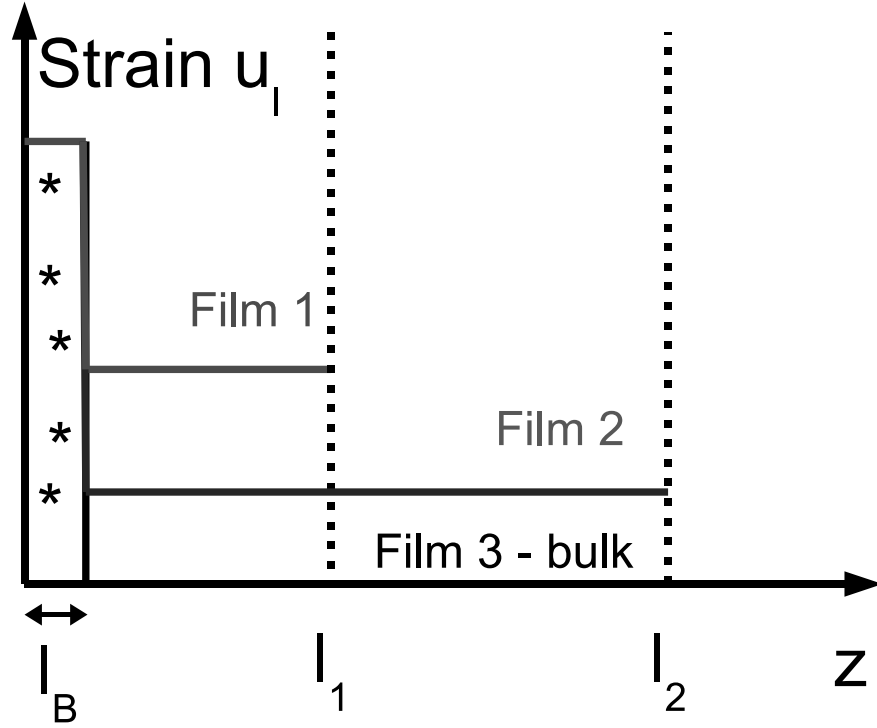
Figure 2.3: Schematic of the segregated strain model; here the elastic defects reside within l_B ($<< l$) of the film-substrate interface so that the majority of the film is homogeneously strained.

superlattices [21] with results that are consistent with experiment [110].

In Fig. 2.2, we display a schematic of the planar ferroelectric capacitor under consideration with the length scales involved. More specifically we assume a single-domain ferroelectric film with the (uniaxial) polarization in the z direction, normal to the film-substrate interface. Physically, we expect a build-up of free surface charge at the ferroelectric boundaries which, if uncompensated, results in a depolarization field E_d. In practice such depolarization effects are significantly reduced by metal electrodes that provide charge compensation; however, their non-ideal nature means that some residual depolarization field remains. Because E_d is proportional to $\frac{l_e}{l}$, where l_e is the screening length of the electrodes, its importance increases with reduced film thickness [22, 13, 111, 112] and becomes significant [29, 113] for $l \sim 100$nm; a term in our Landau expansion will be included to account for these depolarization effects.

The defect buffer layer is also displayed in Fig. 2.2 and, as discussed above, we assume homogeneous (but possibly relaxed relative to the substrate) strain in the remainder of the ferroelectric film which is controlled by the substrate-film lattice mismatch. Following a previous analysis of epitaxially strained films [92], the stress tensors $\sigma_{zz} = \sigma_{xz} = \sigma_{yz} = 0$, because there are no tractions acting on the top film surface. For the special case of a (001) ferroelectric film grown on a cubic substrate, the strain $u_{xx} = u_{yy} = u_l$ and $u_{xy} = 0$ since the angle between the two lattice vectors remains unchanged ($\theta = \frac{\pi}{2}$). We consider here film tetragonal symmetry with $u_{zz} \neq 0$ and $u_{yz} = u_{xz} = 0$. These mixed mechanical boundary conditions associated with two-dimensional clamping mean that the standard elastic free energy $G(P, \sigma)$ cannot be used to find the equilibrium properties of these systems; instead a Legendre transformation, $G'(P, u_l) = G(P, \sigma) + u_l(\sigma_{xx} + \sigma_{yy}) + u_{zz}\sigma_{zz}$, to a modified thermodynamic potential must be performed in order to study the equilibrium properties of the constrained film [92].

We are almost ready to write an expression for $G'(P, u_l)$ and to calculate observable thermodynamic quantities. As discussed earlier, the experiments suggest a term in G that breaks the symmetry $P \rightarrow -P$. This is achieved by linear coupling of P to an external electric field E_{ext} and/or to an effective bias field [95], which we take to be of the form

$$W_l = W_0 e^{-l/l_w}, \tag{2.2}$$

where $l_w \sim l_c$. We note that the thickness-dependence of W_l is included to model the increased smearing of the dielectric susceptibility with decreasing l of ferroelectric films [95]. At present we will treat W_l phenomenologically, and will defer discussion of its exponential decay and its possible origins to Sec. 2.5.

Putting all these elements together, we begin our phenomenological study with the free-energy

expansion

$$
\begin{aligned}
G(P,\bar{\sigma},T) &= \frac{1}{2}\tilde{\alpha}(T)P^2 + \frac{1}{4}\gamma P^4 - (W_l + E_{ext})P - Q_{11}\sigma_{zz}P^2 \\
&\quad - Q_{12}(\sigma_{xx} + \sigma_{yy})P^2 - \frac{1}{2}s_{11}(\sigma_{xx}^2 + \sigma_{yy}^2 + \sigma_{zz}^2) \\
&\quad - s_{12}(\sigma_{xx}\sigma_{yy}) - s_{12}\sigma_{zz}(\sigma_{xx} + \sigma_{yy}) - \frac{1}{2}s_{44}\sigma_{xy}^2,
\end{aligned}
$$

(2.3)

where $\tilde{\alpha}(T) = \alpha(T) + \alpha_d$; $\alpha(T) = \beta(T - T_{bulk})$, T_{bulk} is the bulk transition temperature, α_d is discussed below, and β and γ are Landau coefficients. Here Q_{ij} and s_{ij} are the electrostrictive constants and the elastic compliances at constant polarization, respectively. The depolarization field contributes to the free energy through the coefficient $\tilde{\alpha}(T)$ in Eq. 2.3 [13, 114],

$$
\alpha_d = \frac{l_e}{\epsilon_0 \epsilon_e l},
$$

(2.4)

where l_e is the screening length of the electrodes, and ϵ_0 and ϵ_e are the electric permittivities of the vacuum and the electrodes, respectively.

The mechanical conditions in the film are $\partial G/\partial \sigma_{xx} = \partial G/\partial \sigma_{yy} = -u_l$, $\partial G/\partial \sigma_{xy} = 0$, and $\partial G/\partial \sigma_{zz} = -u_{zz}$ [92]. Solving for the in-plane stresses, one finds that $\sigma_{xy} = 0$ and $\sigma_{xx} = \sigma_{yy} \equiv \sigma$, where the applied in-plane stress σ is eliminated by the in-plane strain $u_l(\sigma)$. This procedure, together with $\sigma_{zz} = 0$, leads to

$$
G'(P_l, u_l, T) = \frac{u_l^2}{s_{11} + s_{12}} + \frac{1}{2}\alpha_l^*(T)P_l^2 + \frac{1}{4}\gamma^* P_l^4 - (W_l + E_{ext})P_l,
$$

(2.5)

where $\gamma^* = \gamma + \frac{4Q_{12}^2}{s_{11}+s_{12}}$ and $\alpha_l^*(T) = \alpha(T) - u_l\frac{4Q_{12}}{s_{11}+s_{12}} + \alpha_d$. We note that we explicitly refer to the l-dependence of the polarization (P_l), which here results from the thickness-dependence of the strain (u_l), the bias field (W_l) and depolarization field term (α_d), consistent with observation. [81] One can express the out-of-plane strain (u_{zz}) through its dependence on the out-of-plane polarization

(P_l) and the in-plane strain (u_l) as

$$u_{zz}(P_l, u_l) = \frac{2s_{12}}{s_{11} + s_{12}} u_l + \left(Q_{11} - \frac{2s_{12}}{s_{11} + s_{12}} Q_{12} \right) P_l^2. \tag{2.6}$$

The Curie film temperature T_c^* refers to the paraelectric-ferroelectric transition at zero total field, $E_l^T \equiv W_l + E_{ext} = 0$. It increases with an applied compressive strain $(Q_{12} < 0)$

$$T_c^* = T_{bulk} + \frac{1}{\beta} \left[u_l \frac{4Q_{12}}{s_{11} + s_{12}} - \frac{l_e}{\epsilon_0 \epsilon_e l} \right] \tag{2.7}$$

but has a decreasing component for very thin films due to depolarization effects. The dielectric susceptibility is

$$\chi_l^{-1} = \epsilon_0 \frac{d^2 G}{dP_l^2} = \epsilon_0 \left[\alpha_l^*(T) + 3\gamma^* P_l^2 \right] \tag{2.8}$$

which diverges at T_c^* if the spontaneous polarization $P_l \to 0$; that can only occur if $E_l^T = 0$ (see Eq. (2.10) below). The dielectric susceptibility is observed to diverge for bulk systems [91] and for free-standing films. [108] In general, $E_l^T \neq 0$ for ferroelectric capacitors and $P_l \neq 0$ at T_c^*, so that χ_l has a finite maximum at a temperature T_{max} defined by $\frac{\partial \chi_l}{\partial T}|_{T=T_{max}} = 0$. We note that this condition combined with the expression for χ_l above yields

$$P_l(T) \frac{dP_l(T)}{dT} \bigg|_{T_{max}} = -\frac{\beta}{6\gamma^*}, \tag{2.9}$$

where we see that T_{max}^l differs from T_c^* and depends on film thickness via the polarization; this equation generally has to be solved numerically to obtain T_{max}^l once the expression for $P_l(T)$ has been determined.

The condition for finding the system in its equilibrium state is $\frac{\partial G}{\partial P} = 0$. The spontaneous polarization P_l emerges then as the solution(s) to the following cubic equation:

$$\alpha_l^*(T) P_l + \gamma^* P_l^3 = E_l^T \tag{2.10}$$

where for $E_l^T = W_l + E_{ext} \neq 0$, we have to be careful to distinguish between the paraelectric (nonswitchable) polarization P_p and the ferroelectric (switchable) polarization P_f. Here, switchable refers to the fact that there are multiple solutions for the polarization that can be accessed by application of a finite E_{ext}. There are three solutions to Eq. (2.10),

$$P_p = \left(\frac{E_l^T}{2\gamma^*} + \sqrt{\mathcal{R}} \right)^{1/3} - \left(-\frac{E_l^T}{2\gamma^*} + \sqrt{\mathcal{R}} \right)^{1/3} \tag{2.11}$$

and

$$P_f = \frac{1}{2} P_p \pm i \frac{\sqrt{3}}{3} \left[\left(\frac{E_l^T}{2\gamma^*} + \sqrt{\mathcal{R}} \right)^{1/3} + \left(-\frac{E_l^T}{2\gamma^*} + \sqrt{\mathcal{R}} \right)^{1/3} \right], \tag{2.12}$$

where

$$\mathcal{R} \equiv \frac{\alpha_l^{*3}(T)}{27\gamma^{*3}} + \frac{(E_l^T)^2}{4\gamma^{*2}} \tag{2.13}$$

and the number of polarization solutions is determined by the sign of $\mathcal{R}$ so that the single nonswitchable P_p corresponds to $\mathcal{R} > 0$. Therefore the transition temperature T_{ferro} between nonswitchable and switchable polarizations occurs when $\mathcal{R} = 0$, leading to the expression

$$T_{ferro} = T_c^* - \frac{3}{\beta} \left(\frac{\gamma^*}{4} \right)^{1/3} (E_l^T)^{2/3}. \tag{2.14}$$

At this temperature, the paraelectric solution becomes an unstable extremum.

In general, the three temperature scales T_{ferro}, T_{max} and T_c^* differ as indicated in Fig. 2.4. We note that for very thin films (< 60 nm), there is suppression of all three temperatures due to depolarization effects. We also remark on the presence of a maximum in $T_{max}(l)$ that has already been alluded to in Section 2.2; this feature will be discussed in more detail when we apply this phenomenology to specific materials and substrates.

2.4   Results

In this section, we calculate dielectric properties for two specific materials, $(Ba_{0.5}Sr_{0.5})TiO_3$ (BST) and $SrTiO_3$ (STO). Our study of BST films allows us to make direct comparison between our
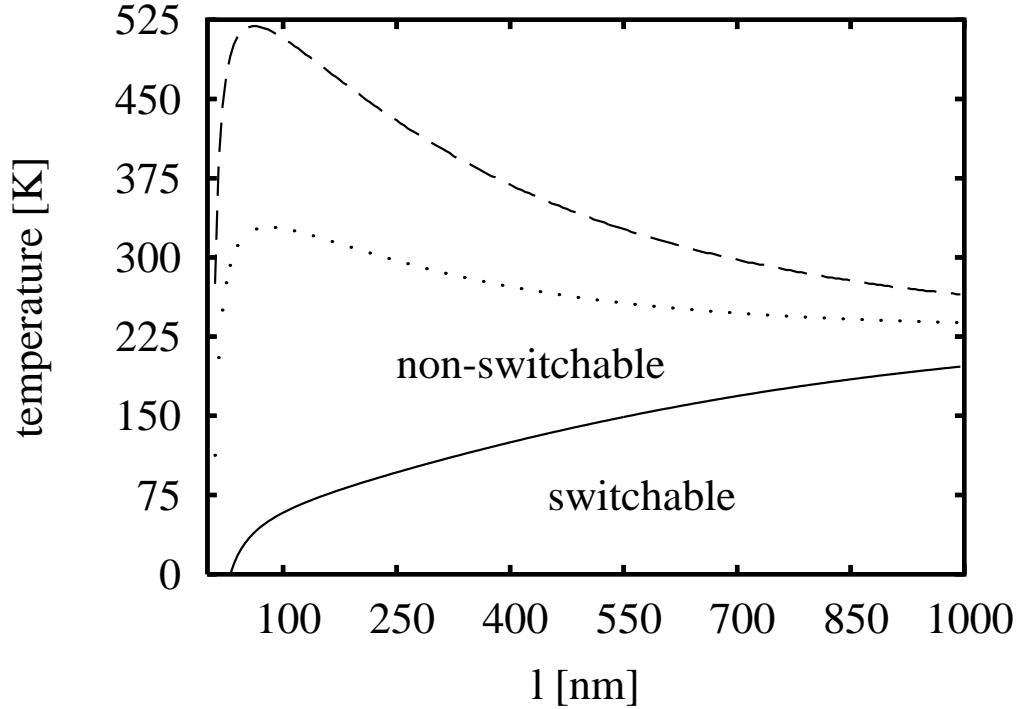
Figure 2.4: Thickness dependence of the three distinct temperature scales T_{ferro} (solid), T_{max} (dashed) and T_c^* (dotted line) for $E_{ext} = 0$ in the segregated defect model described in the text. Here, Landau coefficients for BST on SRO [see Tables 2.1 and 2.2 in Sec. 2.4] have been used and $T_{max}(l)$ is noted to display a peak at $l^* = 60$ nm.

calculated properties and the experiments (Fig. 2.1) that motivated the inhomogeneous strain scenario. [81] In order to explore different parameter regimes, we study these films on two distinct substrates, SRO and Pt/SiO$_2$/Si (PSS); here, we note that the latter is a hypothetical case since to date epitaxially grown single-crystal films of BST on PSS have not yet been realized.

We also apply our phenomenological treatment to STO films that are known for their coherence; this is achieved by highly controlled growth conditions that inhibit defect formation, and thus, inhomogeneous strain effects are not expected. [15] To our knowledge, there do not exist published high-resolution dielectric measurements of strained STO films with polarization normal to the electrode-ferroelectric interface. We therefore compare our results whenever possible to first-principles calculations, [116] and make experimental predictions for a range of epitaxial strain values that could be realized by a variety of substrates.

The parameters used in our calculations are presented in Tables 2.1 and 2.2. Table 2.1 indicates

Table 2.1: Landau parameters for BST [92, 81] and STO [115] (in SI units). We use the $T > 100K$ values for $\alpha(T)$, except in calculations in Fig. 2.15 where we interpolate the $T > 100K$ and the $T < 50K$ values to $75K$, where the two $\alpha(T)$ functions cross.

Film	$\gamma(T)$ (10^6)	Q_{11}	Q_{12}	$s_{11} + s_{12}$ (10^{-12})
BST	4[796 + 2.16(T-273)]	0.110	-0.0430	5.6
STO	1700	0.066	-0.0135	3.0

Film	$\alpha(T)$ (10^5)
BST	9.1 (T - 235.0)
STO ($T > 100K$)	7.06 (T - 35.5)
STO ($T < 50K$)	263.5 (Coth[42.0/T] - 0.90476)

Table 2.2: Film parameters: effective field W_0 and compressive strain u_m [15, 81], with associated length scales l_w and l_c [106] [see Eqs. 2.1 and 2.2]; also the values for screening length l_e [117] and the relative permittivity ϵ_e of electrodes are shown.

Film	Substrate	W_0 (kV/cm)	l_w (nm)	u_m (%)	l_c (nm)	l_e (nm)	ϵ_e
BST	SRO	400	300	-0.50	300	0.023	1.0
BST	PSS	450	300	-0.77	300	0.400	1.0
STO	LSAT	400	300	-0.90	300	0.023	1.0

the Landau coefficients used for each material. Film-related parameters, displayed in Table 2.2, are determined from data on strain relaxation; the characteristic length l_c [see Eq. (2.1)] from the lattice constant measurements lies somewhere between 200 and 300 nm [106, 109]. In order to make comparison with the inhomogeneous strain model scenario, which uses a characteristic length scale of 300 nm [81], we keep this l_c value in our calculations. Data on electrode screening lengths (l_e) is l_e of SRO of 0.23 Å [117], and we set l_e of $(LaAlO_3)_{0.29} \times (SrAl_{0.5}Ta_{0.5}O_3)_{0.71}$ (LSAT) to be the same value, since LSAT is dominated by $SrAl_{0.5}Ta_{0.5}O_3$ that is very similar to SRO. We choose the screening length of PSS to be $l_e = 4$ Å, which is expected to be larger than l_e in metallic SRO due to the presence of semiconducting silicon. We display strain u_m value for three different substrates, BST on SRO, [81] BST on PSS ($a_{BST} = 3.95$ Å, $b_{Pt} = 3.92$ Å), and STO on LSAT. [15] The bias

field is set to be $W_0 = 4.0 \times 10^7$ V/m for BST films on SRO, a value that is comparable to that of applied external fields in related BST dielectric measurements. [106] We keep the same W_0 for STO films and a slightly different one ($W_0 = 4.5 \times 10^7$ V/m) for BST films on PSS. The bias field W_l is treated phenomenologically [see Eq. (2.2)] and we emphasize its crucial role in modeling key features of the dielectric properties of ferroelectric films, as will be discussed in more detail shortly.

2.4.1 $(Ba_{0.5}Sr_{0.5})TiO_3$

In Fig. 2.4, we display the three temperature scales as a function of thickness for BST films on SRO electrodes with $E_{ext} = 0$: T_{max}, T_c^* and T_{ferro}. Because $E_l^T = W_l \neq 0$, there is a clear separation of the three temperatures; for $E_l^T = 0$, they collapse onto T_c^* [compare Eqs. (2.7), (2.9), and (2.14)]. Therefore an estimate of W_0 can be obtained from the difference of T_{max} and T_c^*, where the latter can be expressed in terms of (experimentally accessible) Landau parameters and by the value of the misfit strain [Eq. (2.7)]. The magnitude of the obtained bias field, $W_0 = 400$ kV/cm, is in rough agreement with experiment: the experimental temperature $T_{max}^{exp} = 250$ K for a 950 nm film in Fig. 2.1 is close to the calculated $T_{max}^{calc} = 268$ K in Fig. 2.4, and $T_{max}^{exp} = 280$ K for the 660 nm film in Fig. 2.1 is also reasonably close to the calculated $T_{max}^{calc} = 304$ K in Fig. 2.4.

The temperature T_{max} displays a peak, $T_{max} = 519$ K at $l^* = 60$ nm, and it decreases with increasing thickness and asymptotically approaches T_c^*, the bulk transition temperature. As previously noted in Sec. 2.2, for $l < l^*$, T_{max} decreases with decreasing l; by contrast for $l > l^*$, the trend is consistent with that displayed in Fig. 2.1. More generally, the behavior of T_{max} depends on that of the polarization as a function of temperature [see Eq. (2.9)]. Both the strain and the bias field make the polarization decrease with increasing film thickness ($l > 60$ nm) as will be discussed shortly, and this monotonic behavior makes T_{max} decrease as well. The observed peak in T_{max} is driven by the depolarization field contribution in our model. T_{max} becomes suppressed for very thin films ($l < 60$ nm) and approaches zero just as does the polarization at these film thicknesses (see Fig. 2.7). The value of $l^* = 60$ nm is determined by the strength of the depolarization contribution, and thus, is expected to depend on the electrode and/or substrate material. As already noted, we use

a longer l_e for BST films on PSS than for BST on SRO. Because the depolarization field contribution to our free energy is proportional to $\frac{l_e}{l}$, [see Eq. (2.4)], the resulting l^* will be larger for BST on PSS than on the SRO substrate. For BST on PSS, we calculate that the peak in T_{max} occurs at $l^* \sim 300$ nm, in contrast to the value of $l^* \sim 60$ nm for BST on SRO displayed in Fig. 2.4.

The theoretical temperature T_c^* in Fig. 2.4 refers to the paraelectric-ferroelectric transition at zero total field, $E_l^T = W_l + E_{ext} = 0$ [see Eq. (2.7)]. It has a peak at 80 nm with a maximum value of $T_c^* = 329$ K, and then decreases with increasing film thickness due to the strain relaxation term, $u_l \sim e^{-l/lc}$. It reaches its bulk transition temperature value ($T_{bulk} = 235$ K) for thicker fully relaxed films: $T_c^* = 238$ K for 1000 nm film. Due to the depolarization contribution [see Eq. (2.4)], T_c^* is suppressed for very thin films and eventually reaches zero.

The temperature T_{ferro} that separates switchable and nonswitchable polarization regimes increases for increasing l and saturates when it reaches the bulk transition temperature. In Eq. (2.14), we see that there is competition between thickness-dependent contributions due to u_l and to W_l in T_{ferro}. Therefore whether this temperature increases or decreases with increasing film thickness depends on their relative magnitudes. For example, T_{ferro} is shown to increase with increasing l in Fig. 2.4, reflecting the dominance of the bias field contribution in this particular case. We note that the switchable (ferroelectric) regime is lost as the films become very thin, e.g., ferroelectricity vanishes at $l \sim 100$ nm at fixed temperature 60 K. T_{ferro} reaches zero at a critical film thickness ($l_{crit} \sim 35$ nm here) and films with $l < l_{crit}$ remain in the nonswitchable polarization regime at all temperatures.

In Fig. 2.5, we display our calculated relative permittivity $\epsilon(T)$ ($\epsilon = 1+\chi$) for BST films on SRO substrates with $E_{ext} = 0$. Reduction in $\epsilon(l)$ as a function of decreasing thickness is observed for both theory and experiment (Fig. 2.1); ϵ_{max} decreases and T_{max} increases as l decreases. Favorable comparison of the calculated relative permittivity ϵ_{max}^{calc} can be made to its measured analog [106] ϵ_{max}^{exp} shown in Fig. 2.1: $\epsilon_{max}^{calc} = 2035$ at $T_{max} = 268$ K matches with $\epsilon_{max}^{exp} \approx 1900$ at $T_{max} \approx 260$ K for the 950 nm film, and $\epsilon_{max}^{calc} = 1044$ at $T_{max} = 304$ K matches with the $\epsilon_{max}^{exp} \approx 1100$ at $T_{max} \approx 290$ K for the 660 nm film.
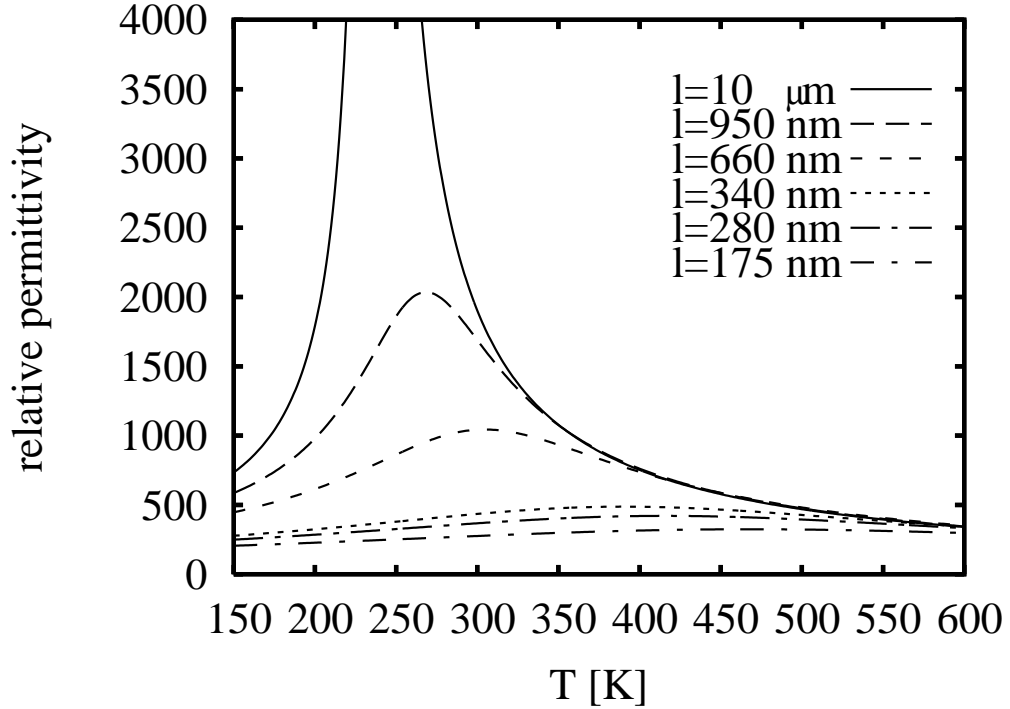
Figure 2.5: Calculated relative permittivity as a function of temperature for BST films on SRO substrates of thicknesses $l = 10\mu m$, 950, 660, 340, 280 and 175 nm. The highest permittivity corresponds to the thickest film; the divergence for $10\mu m$ film at the bulk Curie temperature 235 K is indicated. Reduction of the permittivity for thin films is observed; the peak of permittivity shifts towards higher temperatures in agreement with Fig. 2.1.

We also predict the thickness-dependent dielectric behavior of $\epsilon(T)$ for BST films epitaxially grown on PSS in Fig. 2.6. For films of decreasing thickness where $l < l^*$, a systematic reduction in ϵ is observed and the peak in the permittivity is shifted to lower temperatures.

Next we present the calculated nonswitchable polarization in Fig. 2.7 at temperature 300 K with $E_{ext} = 0$ for BST films on SRO. The polarization is roughly proportional to the bias field W_l and its value increases with increasing misfit strain u_l [see Eq. (2.10)]. Motivated by experiment, we have modeled the bias field and misfit strain to decrease with increasing film thickness exponentially ($\{W_l, u_l\} \sim e^{-l/l_x}$, $l_x = \{l_w, l_c\}$), and therefore the polarization also decreases with thicker films. However, for very thin films ($l < 50$ nm), there is suppression of the polarization (P) due to depolarization field effects and a peak with a maximum value of polarization $P_{max} = 0.2\ C/m^2$ at $l = 50$ nm develops. The temperature dependence of the polarization for two different film thicknesses is displayed in the inset of Fig. 2.7. These $P(T)$ curves shows good qualitative agreement with
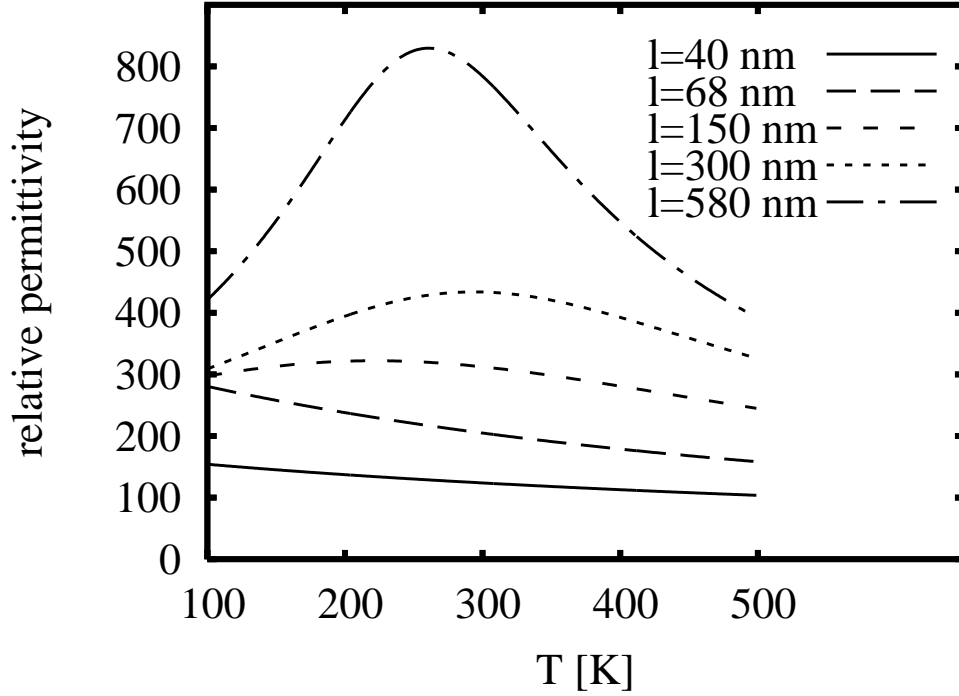
Figure 2.6: Calculated relative permittivity as a function of temperature for BST films epitaxially grown on PSS substrates of thicknesses $l = 40, 68, 150, 300$ and 580 nm. The highest permittivity corresponds to the thickest film. Reduction of the permittivity for thin films is observed, and the peak of permittivity shifts towards lower temperatures.

analogous measurements. [81] In general, the polarization decreases with increasing temperature.

T_{ferro}, the transition temperature separating the presence of switchable and nonswitchable spontaneous polarizations, is plotted in the presence of external electric field for BST films on SRO in Fig. 2.8. $T_{ferro}(E_{ext})$ reaches its maximum at $E_{ext} = -W_l$ (where $W_l = W_0 e^{-l/l_c}$), and decreases symmetrically about this value in agreement with Eq. (2.14); we note that the maximum of T_{ferro} decreases for thicker films as anticipated by the zero-total-field (E_l^T) results of T_c^* displayed in Fig. 2.4. The temperature T_{ferro} at zero external field matches the behavior of Fig. 2.4. Switchable and nonswitchable polarization phases are marked.

Calculated hysteresis loops are displayed in Fig. 2.9 for BST films on SRO substrates at $T = 290$ K with $l = 100$ nm and $l = 175$ nm. According to Fig. 2.8, at this temperature for these film thicknesses, the switchable polarization develops only for certain values of nonzero external electric field: $E_{ext} = \{-298, -275\}$ kV/cm for 100 nm film and $E_{ext} = \{-229, -218\}$ kV/cm for 175 nm
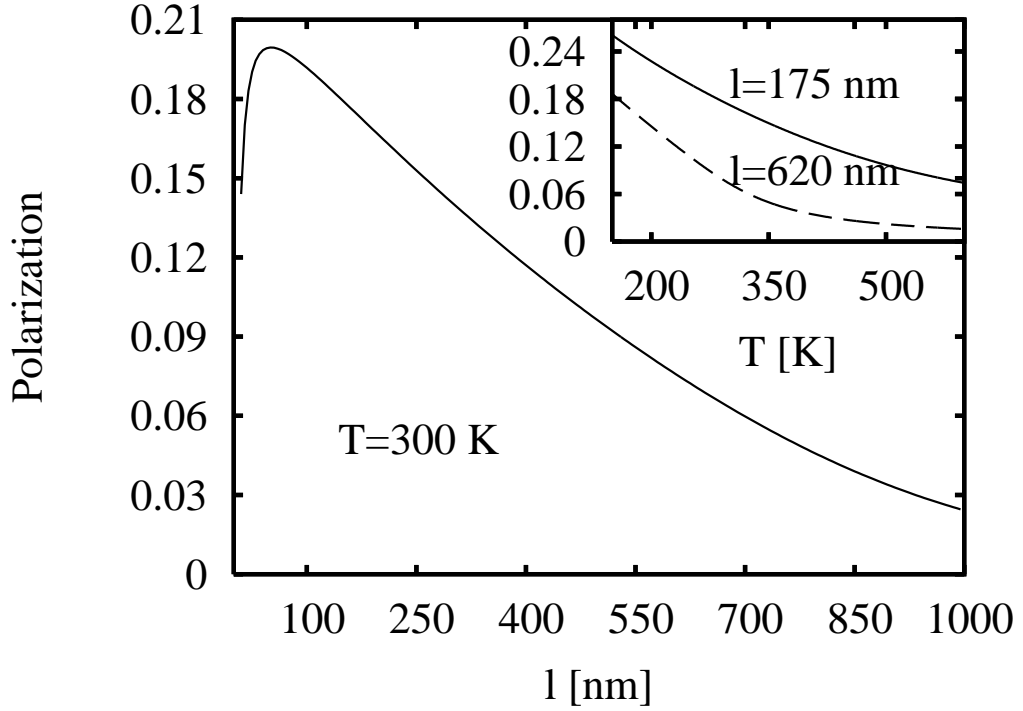
Figure 2.7: Calculated nonswitchable polarization P[$\frac{C}{m^2}$] (see Fig. 2.4) for BST films on SRO substrates of various thicknesses (l) at temperature 300 K and for $E_{ext} = 0$; polarization as a function of temperature for films of thickness 175 (solid) and 620 nm (dashed line) is shown in the inset.

film. The width of the hysteresis loops in Fig. 2.9 is given by the above field ranges; it decreases with increasing film thickness and shows good qualitative agreement with experiment. [106] Hysteresis loops are symmetric around the point $E_{ext} = -W_l$ and $P = 0$, where the bias field W_l is the thickness-dependent field offset. This field offset (specifically, we refer to the shift of the center of the hysteresis loop along the field axis from zero-field position) becomes larger for thinner films [see Eq. (2.2)] and is temperature independent. However, the width of the loops shrinks as temperature is increased, as shown in Fig. 2.8. Symmetry in the hysteresis loops around $P = 0$ yields zero offset in the spontaneous polarization and therefore no associated charge offset within the thin film. We note that significant charge offsets are observed in graded films with designed polarization and strain gradients. [118]
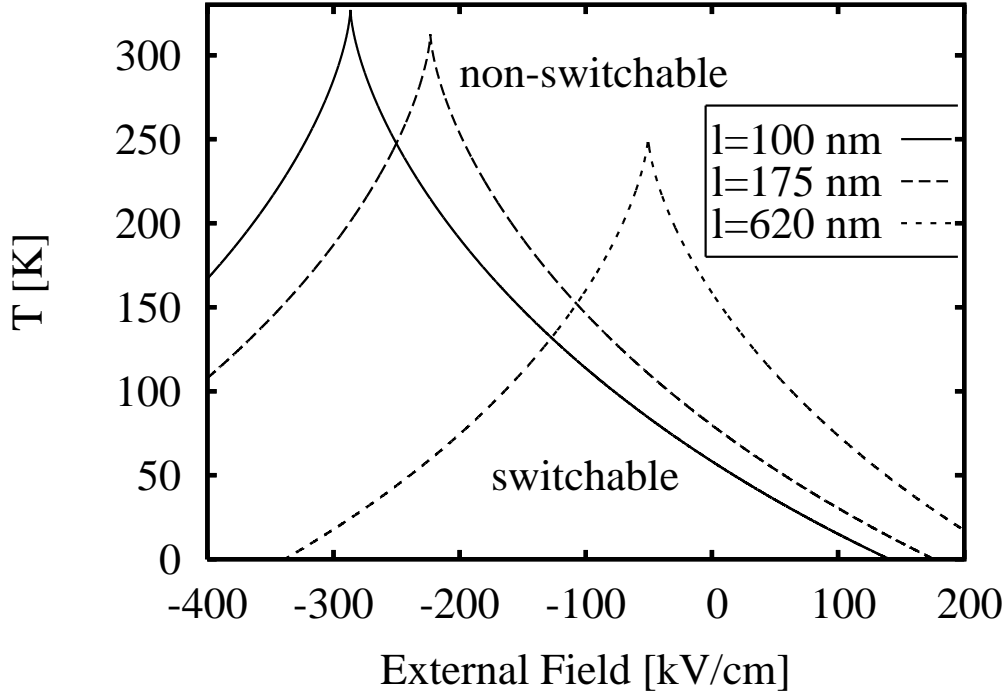
Figure 2.8: Transition temperature T_{ferro} as a function of applied external electric field E_{ext} for BST films on SRO substrates of thicknesses 100 (solid), 175 (dashed) and 620 nm (dotted line). The corresponding line divides the region into switchable and nonswitchable polarization phases for each film.

2.4.2   Strained SrTiO$_3$

Bulk strontium titanate (STO) remains paraelectric down to the lowest temperatures accessible, but strained STO films may be driven into a ferroelectric phase even at room temperature. [15] To our knowledge, detailed thickness-dependent dielectric measurements on such STO films have been performed only with tensile epitaxial strain, resulting to in-plane polarization. [15, 119] Here, we make predictions for the thickness-dependent dielectric properties of STO films with compressive epitaxial strains and polarizations normal to the film-substrate interface.

We begin by making direct comparison between our results and those of *ab initio* studies, [116] displayed in Figs. 2.10 and 2.11. Since *ab initio* calculations consider uniformly strained films without strain relaxation and without an effective bias field, we set $W_l = 0$ for the purpose of comparison here. In Fig. 2.10, we present the spontaneous polarization as a function of misfit strain for a $l = 100$ nm STO film at zero total field, $E_l^T = 0$. Dots in the figure correspond to
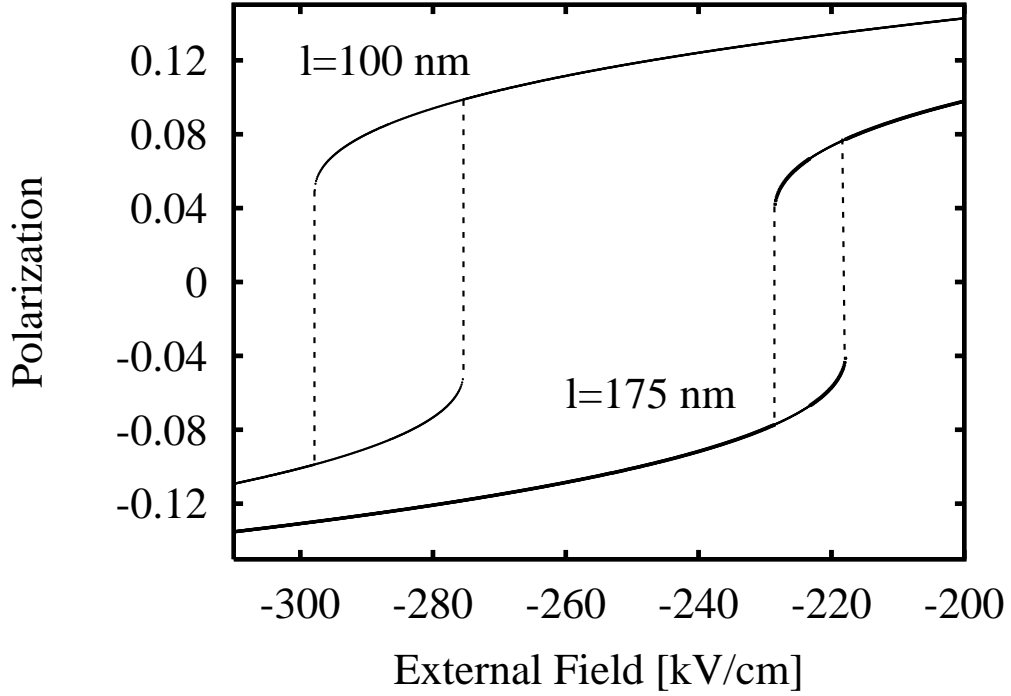
Figure 2.9: Calculated hysteresis polarization loops for BST films on SRO substrates of thicknesses 100 and 175 nm at temperature 290 K.

first-principles calculations, [116] where the out-of-plane polarization in the ferroelectric tetragonal phase ($u_l < -0.75\%$) for films with zero macroscopic field has been calculated. We choose the $l = 100$ nm STO film where we do not expect depolarization effects to be important ($l > l^*$; see Fig. 2.14) for comparison with the *ab initio* data. Good agreement is achieved at temperatures $T \sim 250$ K; our calculated curves follow the behavior of the *ab initio* dots. At lower temperatures, better agreement is achieved for less compressive strain, correctly indicating that fully relaxed STO is paraelectric down to zero temperature.

Continuing our comparison with the results of *ab initio* calculations, [116] we display the paraelectric relative permittivity as a function of external electric field E_{ext} and film strain u_l for a $l = 100$ nm STO film at $T = 200$ K in Fig. 2.11. A nonpolar tetragonal phase develops for strains $-0.75\% < u_l < +0.54\%$ according to the *ab initio* calculations. [116] From Fig. 2.10, the best fit for the polarization just at the paraelectric-ferroelectric phase boundary ($u_l = -0.75\%$) is achieved
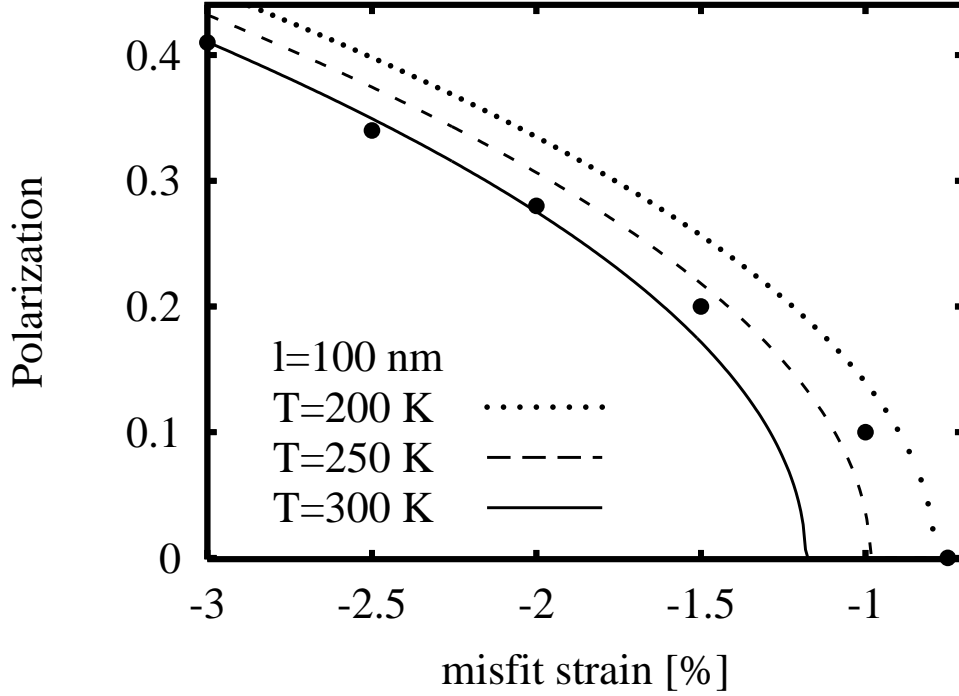
Figure 2.10: Spontaneous polarization $P[C/m^2]$ as a function of misfit strain (u_l) for 100 nm STO film at temperatures $T = 200$ (dotted), $T = 250$ (dashed) and $T = 300$ K (solid line) and zero total field, $E_l^T = 0$. Dots correspond to ab-initio values of the polarization taken from [116].

at $T = 200$ K, and therefore we choose this temperature to calculate our paraelectric permittivity data. We compare our results to the *ab initio* calculations in the range of compressive strain $-0.5\% < u_l < 0.0\%$: in both cases, the permittivity (ϵ) increases with increasing compressive strain; this occurs even more rapidly in the range of external fields $-150 < E_{ext} < 150$ kV/cm, and its magnitude in the range $800 \leq \epsilon \leq 1500$ in Fig. 2.11 roughly corresponds to the *ab initio* values $400 \leq \epsilon \leq 1800$. [116] We note that the observed increase of the paraelectric permittivity with strain can be understood from Eq. (2.8).

Both Figs. 2.10 and 2.11 indicate good agreement between results of our phenomenological model and those of previous first-principles calculations, and this provides us with confidence regarding the Landau coefficients and more generally with the approach described here applied to strained STO films. Next we calculate the dielectric properties of strained STO films using a nonzero value for the effective bias field, $W_0 = 400$ kV/cm, that is comparable to that used for BST films in Sec 2.4.1.
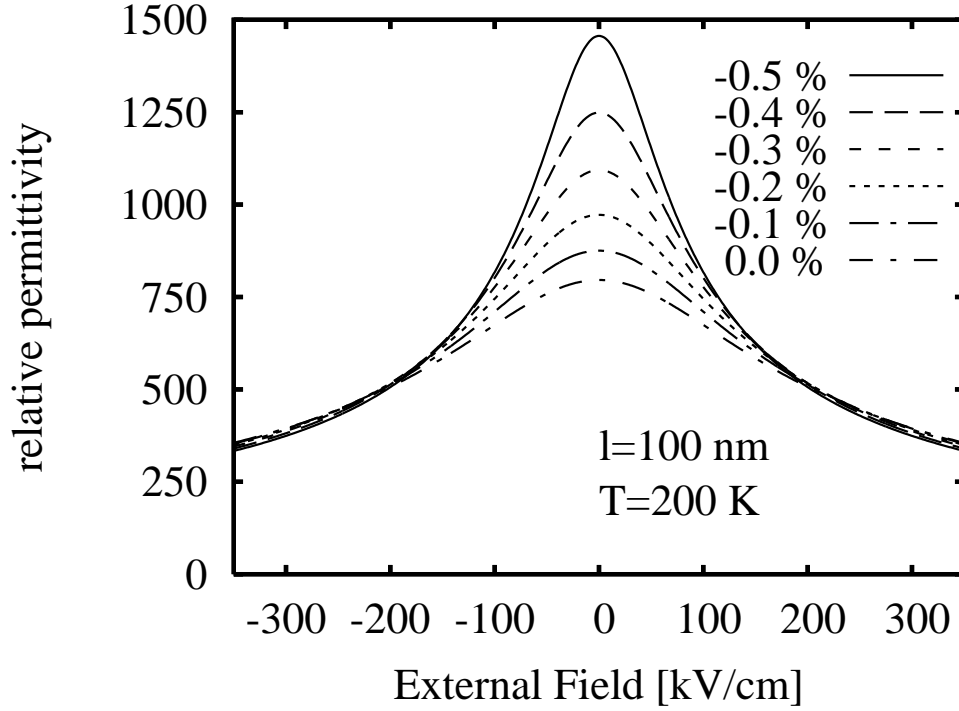
Figure 2.11: Calculated paraelectric relative permittivity as a function of external electric field E_{ext} and misfit strain $u_l = -0.5, -0.4, -0.3, -0.2, -0.1$ and 0.0% for 100 nm STO film at temperature $T = 200$ K. The permittivity data are shown in the limit of zero bias field W_l in order to make comparison with the ab-initio data in [116].

Our calculated relative permittivity as a function of temperature and film thickness at compressive strain $u_m = -0.9\%$ (STO on LSAT) with $E_{ext} = 0$ is plotted in Fig. 2.12. The permittivity is suppressed for thinner films and its maximum is shifted toward higher temperatures, displaying similar trends for both ϵ and T_{max} as for BST on SRO in Sec 2.4.1. T_{max} increases with decreasing l, but develops a peak at $l = 60$ nm and is again suppressed for very thin films due to depolarization effects. The screening length of LSAT is comparable to l_e for SRO, and thus so is l^*. The magnitude of ϵ is also comparable to that in BST films in Fig. 2.5; it results from similar values of the Landau coefficients and the value of the compressive strain in both films [see Table 2.1]. To our knowledge, there exists only one published dielectric measurement on strained STO with the polarization normal to the film-substrate interface; this experiment, performed on a $l = 50$ nm STO film grown on LSAT [$u_m = -0.9\%$ (Ref. [15])], yields $\epsilon_{max}^{exp} \approx 400$, which is in a good agreement with our calculated maximum value of permittivity, $\epsilon_{max}^{calc} = 364$ for this film/substrate combination.
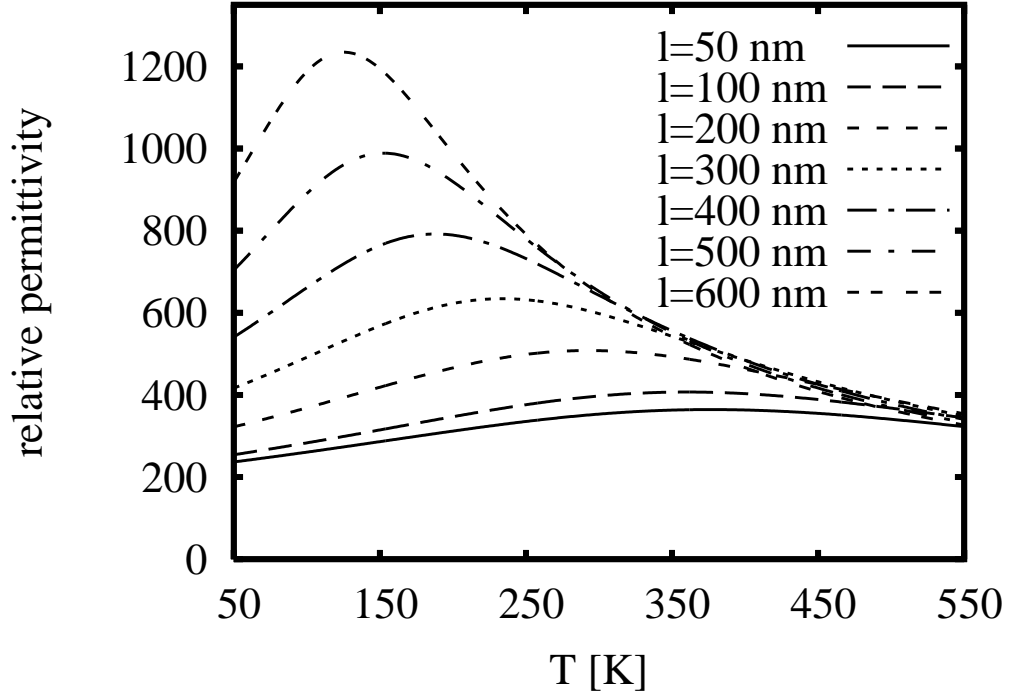
Figure 2.12: Calculated relative permittivity as a function of temperature for STO films of thicknesses $l = 50, 100, 200, 300, 400, 500$ and 600 nm at misfit compressive strain $u_m = -0.9\%$. The highest permittivity corresponds to the thickest film. Reduction of the permittivity for thin films is observed.

We investigate the effect of compressive strain on the relative permittivity in Fig. 2.13. We observe that increased compressive strain shifts the permittivity curve toward higher temperatures and larger shifts of T_{max} occur for thinner films.

We display the nonswitchable polarization as a function of film thickness and misfit strain at $T = 300$ K and $E_{ext} = 0$ in Fig. 2.14. Again, the polarization shows similar behavior as in BST films in Sec. 2.4.1; it decreases with increasing film thickness and is suppressed for very thin films (< 50 nm) due to depolarization effects. Increasing the strain results in higher polarization, in agreement with Fig. 2.10; this time, however, the polarization values change due to the effect of a nonzero bias field. In the inset, the temperature dependence of the nonswitchable polarization is plotted in $l = 100$ nm and $l = 500$ nm STO films at misfit strain $u_m = -0.9\%$ (STO on LSAT substrate). The polarization decreases with increasing temperature.

Unstrained bulk STO remains paralectric down to zero temperature. However, as previously
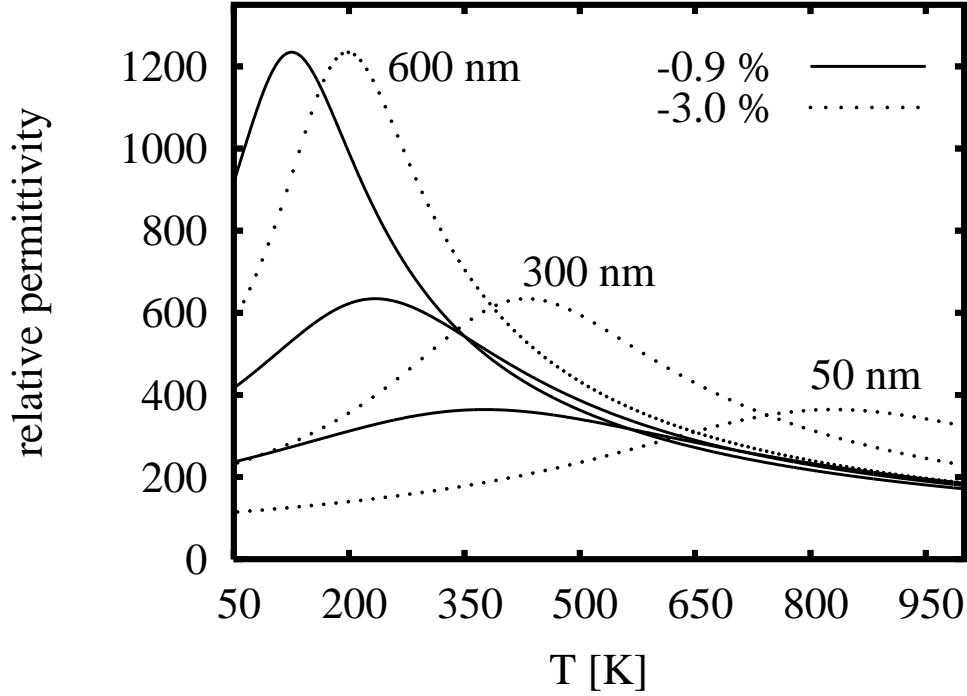
Figure 2.13: Calculated relative permittivity as a function of temperature for STO films of thicknesses $l = 50$, 300 and 600 nm at misfit strain $u_m = -0.9\%$ (solid) and $u_m = -3.0\%$ (dotted line). Higher values of misfit compressive strain shifts the permittivity curve towards to higher temperatures where the larger shifts of T_{max} are observed for the thinner films.

noted, a ferroelectric regime occurs for strained STO films. [15] We plot the transition temperature T_{ferro}, separating switchable and nonswitchable polarization regimes, as a function of film thickness and misfit strain at $E_{ext} = 0$ in Fig. 2.15. We predict a ferroelectric phase to occur for compressive strains larger than 2.0%, and note that ferroelectricity is recovered here for the thinnest STO films as one goes from a thick-film nonswitchable regime to a thin-film switchable one (at fixed T); e.g., ferroelectricity emerges at -2.0% strained films for thicknesses $30 \lesssim l \lesssim 160$ nm. This is distinct from the behavior previously described in BST films, where ferroelectricity is lost by making films thinner (see Fig. 2.4). T_{ferro} indicates a maximum at $l^* \approx 60$ nm, and this peak is due to depolarization effects [see Eq. (2.4)] that reduce the transition temperature to zero for the thinnest films. T_{ferro} decreases in thicker films ($l > 60$ nm) for values of compressive strain $u_m > 2.0\%$, as shown in Fig. 2.15. However, it increases with increasing film thickness for small values of compressive strain ($u_m \lesssim 1.5\%$), similarly to BST films on SRO substrates (with $u_m = -0.5\%$) in
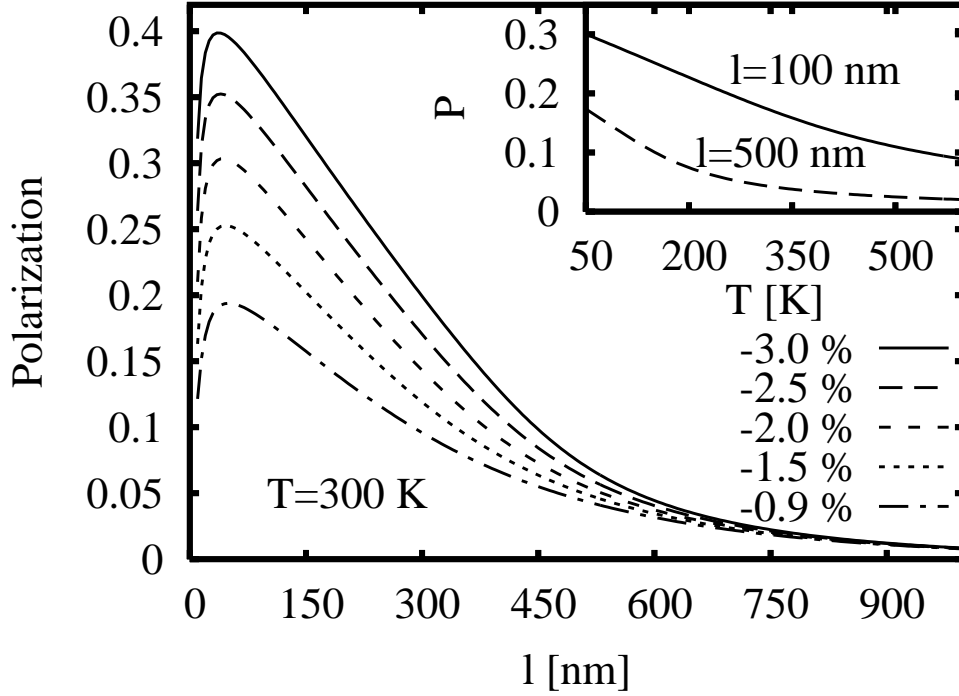
Figure 2.14: Calculated nonswitchable polarization $P[C/m^2]$ of STO films as a function of film thickness (l) for misfit strains $u_m = -3.0, -2.5, -2.0, -1.5$ and -0.9% at temperature 300 K. In the inset, the polarization as a function of temperature (T) is plotted for 100 (solid) and 500 nm (dashed line) films at misfit strain $u_m = -0.9\%$ and zero external field.

Fig. 2.4. We note here that although T_{ferro} increases, it has negative nonphysical value for these low strain values, and thin films remain in the nonswitchable regime down to zero temperature. As noted previously, the thickness dependence of this temperature scale arises from competition between strain and bias field contributions [see Eq. (2.14)]; the former dominates for large enough mistmatch strains ($u_m \gtrsim 2.0\%$), and in this case, T_{ferro} decreases with increasing film thickness.

2.5 Discussion

Next we explore the implications of our results and the origin of our model assumptions. We begin with a general discussion of the effective bias field in epitaxial perovskite oxide films. Both the inhomogeneous (see Fig. 2.16) and the segregated (see Fig. 2.3) strain models describe the thickness-dependent dielectric properties of ferroelectric films consistently with experiment, and thus, further measurements are required to determine the presence and/or absence of underlying
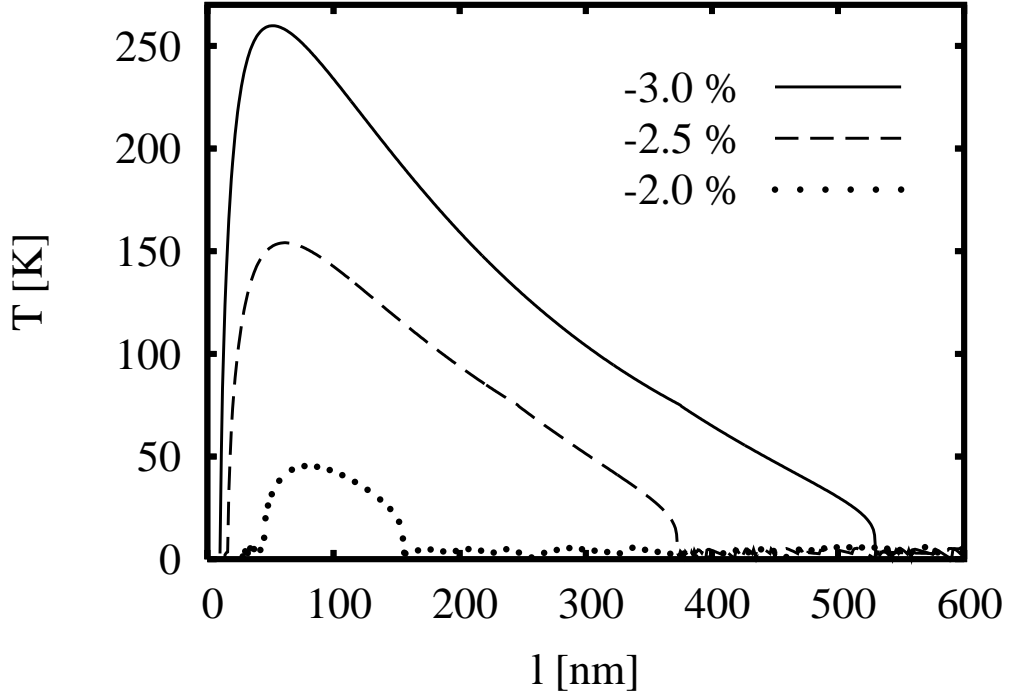
Figure 2.15: Transition temperature T_{ferro} separating switchable (below) and nonswitchable (above the temperature curve) polarization phases as a function of STO film thickness l and misfit strain $u_m = -3.0, -2.5$ and $-2.0\ \%$ for $E_{ext} = 0$. T_{ferro} becomes negative for compressive misfit strain values smaller than 1.5% for all film thicknesses, resulting in a nonswitchable polarization regime.

inhomogeneous strain throughout the film. These models each have effective bias fields, one that is spatially varying [81] and the other that is uniform, and it is exactly this feature that we exploit in a proposed benchtop experiment to distinguish these two scenarios.

An effective bias field breaks up-down symmetry at all temperatures. In a film above the zero-(external) field ($E_{ext} = 0$) ferroelectric transition temperature T_{ferro}, this results in a nonzero macroscopic polarization in zero external electric field [see Eq. (2.10)]. For the sake of complete-ness, we note that the Curie temperature T_c^* refers to the paraelectric-ferroelectric transition at zero total field ($E_l^T \equiv W_l + E_{ext} = 0$). While this polarization can vary with temperature, making the film pyroelectric, it should not be confused with a ferroelectric spontaneous polarization. The correct distinction between polar and ferroelectric films is made on the basis of switchability, as determined, for example, through a hysteresis measurement. In a nonswitchable polar film, there is

Inhogeneous Strain Model
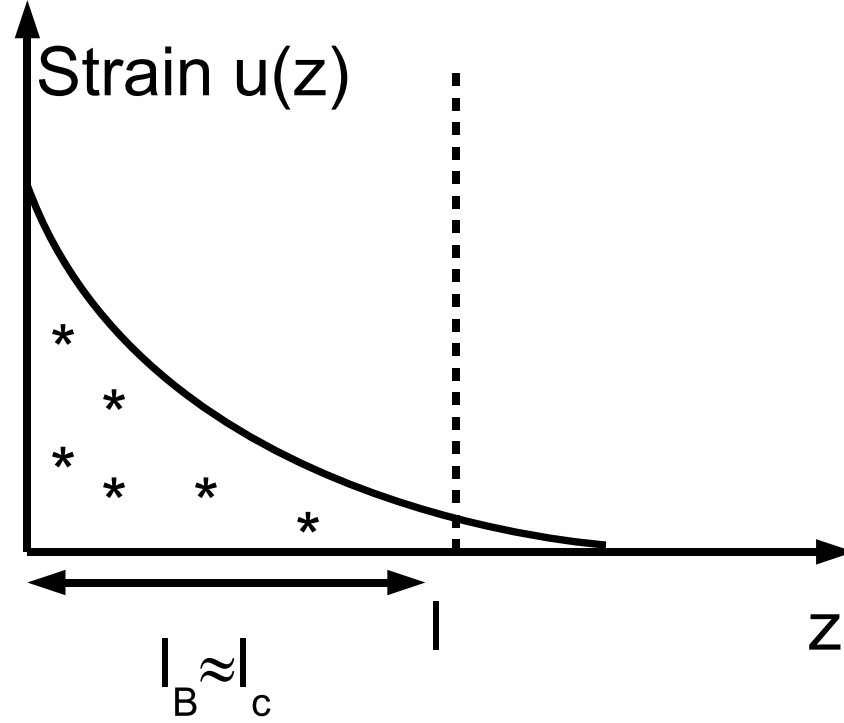
Figure 2.16: Schematic of the inhomogeneous strain model [81] where the effective bias field $W(z)$ is spatially-dependent due to flexoelectric coupling; here the characteristic length scales associated with the strain relaxation (l_c) and the buffer layer (l_B), where the elastic defects reside, are assumed comparable with the overall film thickness (l).

only one locally stable polarization state with $E_{ext} = 0$, and the system will show dielectric behavior in a finite external electric field. On the other hand, if there are two (or more) stable polarization states for the system with $E_{ext} = 0$ that can be switched by the application of an external electric field, then the film is ferroelectric, and it will exhibit a characteric ferroelectric hysteresis loop. An effective bias field W_l will lead to a lateral shift in the ferroelectric hysteresis loop, which can be used to determine the associated effective bias voltage across the film. Field offsets have been, indeed, experimentally observed in 100 nm PbZr$_{0.2}$Ti$_{0.8}$O$_3$ thin films. [120] We also remark that an effective bias field will make the two polarization states symmetry inequivalent with different energies.

The transition from nonswitchable to switchable ferroelectric phases usually occurs as a function of decreasing temperature at T_{ferro}. The detailed thickness dependence of T$_{ferro}$ depends on material-specific parameters, as can be seen in Figs. 2.4 and 2.15 for BST and STO thin films. More generally the l dependence of the dielectric properties enters via the strain relaxation [Eq. (2.1)], the bias [Eq. (2.2)], and the depolarization fields. For the strain relaxation, an exponential decay on a characteristic length scale of several hundred nanometers was observed experimentally. [106, 109] In our model, we assume the same exponential decay for the magnitude of the uniform effective bias field. These two quantities determine the thickness dependence of the quantities of interest in all but the very thinnest films, where the depolarization field term dominates, strongly suppressing T_{ferro}, the polarization, and T_{max}. In the case of the temperature T_{ferro} (see Figs. 2.4 and 2.15), the strain and effective bias contributions opppose each other [Eq. (2.14)], and depending on their relative strengths, $T_{ferro}(l)$ increases (BST case where W_l dominates) or decreases (situation for strained STO where u_l is greater) with increasing film thickness l.

A direct consequence of the strain contribution to T_{ferro} is that we predict that ferroelectricity can be strengthened as the films get thinner (u_l increases with decreasing l), resulting in a transition from a nonswitchable polar phase to a ferroelectric state below a critical thickness l_{CT}; more specifically, for STO measured at 100 K and compressive strain -2.5% (see Fig. 2.15), the critical thickness below which ferroelectricity appears is $l_{CT} = 200$ nm. This runs counter to the usual notion that ferroelectricity is suppressed as the film thickness decreases, disappearing below a critical thickness; we note that would be the case for BST on SRO (here, W_l dominates the expression for T_{ferro}) where our results displayed in Fig. 2.4 indicate a critical thickness of about 100 nm at temperature 60 K. This reentrant ferroelectricity as a function of decreasing l should be readily observable in an appropriate experiment for strained STO films, with the polarization normal to the film-substrate interface.

Both the strain and the effective bias contributions act to decrease $T_{max}(l)$ and P_l [related by Eq. (2.9)] as a function of increasing film thickness (l) (see Figs. 2.4, 2.7 and 2.14). By contrast, the depolarization contribution suppresses $T_{max}(l)$ and P_l with decreasing l. The dominance of

this depolarization term explains the observed shift of the peak of $T_{max}(l)$ to higher values of l^* for semiconducting substrates (e.g., PSS) (see Fig 2.6) that have longer screening lengths (l_e) than their metallic counterparts (e.g., SRO). Here, we recall that the depolarization contribution to the free-energy expansion is $\alpha_d \sim l_e/l$ [Eq. (2.4)]. We note that the thickness-dependent effect of the depolarization field on the relative permittivity has been noted before [95] with a similar term, $\alpha_d^{BL} = a/l$, where boundary conditions for the spatially varied polarization are proposed that incorporate the effects of a symmetry-breaking effective field. In this previous approach, [95] a then is a boundary-related characteristic length. Since the thickness dependence in both treatments is the same, one obtains similar results for the relative permittivity with appropriate choice of these length scales (l_e and a) although their physical origins are different. Here, we have extended this treatment to address the thickness dependence of other dielectric properties (e.g., polarization) as well, and we note that the previous inhomogeneous strain approach [81] did not include such depolarization effects for thin ferroelectric films.

The smearing of the sharp peak in the temperature-dependent dielectric response(Figs. 2.5, 2.6 and 2.12) in zero electrical field ($E_{ext} = 0$) is a signature of the presence of a finite effective bias field W; this point has been much discussed previously both here [see Eqs. (2.8) and (2.10)] and by others. [81, 95, 101, 108] W_l assumes larger values for thinner films [see Eq. (2.2)] and so pushes the permittivity to smaller values in thinner films [see Eq. (2.8)], in accordance with experiment (Fig. 2.1). In the bulk limit, both the strain and the bias field vanish and bulk behavior of the dielectric properties is recovered.

While there is general agreement that effective bias fields play an important role in the properties of perovskite thin films, [81, 95, 101, 108] their specific origins and their spatial natures in the films are less well understood. For example, an effective bias field can be produced by a spatially (z) dependent strain via a flexoelectric effect; [81] we will refer to this as the inhomogeneous strain model, and it is schematically depicted in Fig. 2.16. In this scenario, misfit dislocations are distributed roughly isotropically throughout the film and produce strain gradients. By contrast, in the segregated strain model presented here, the elastic defects are concentrated in a thin buffer layer

Benchtop Probe for the Segregated Strain Model
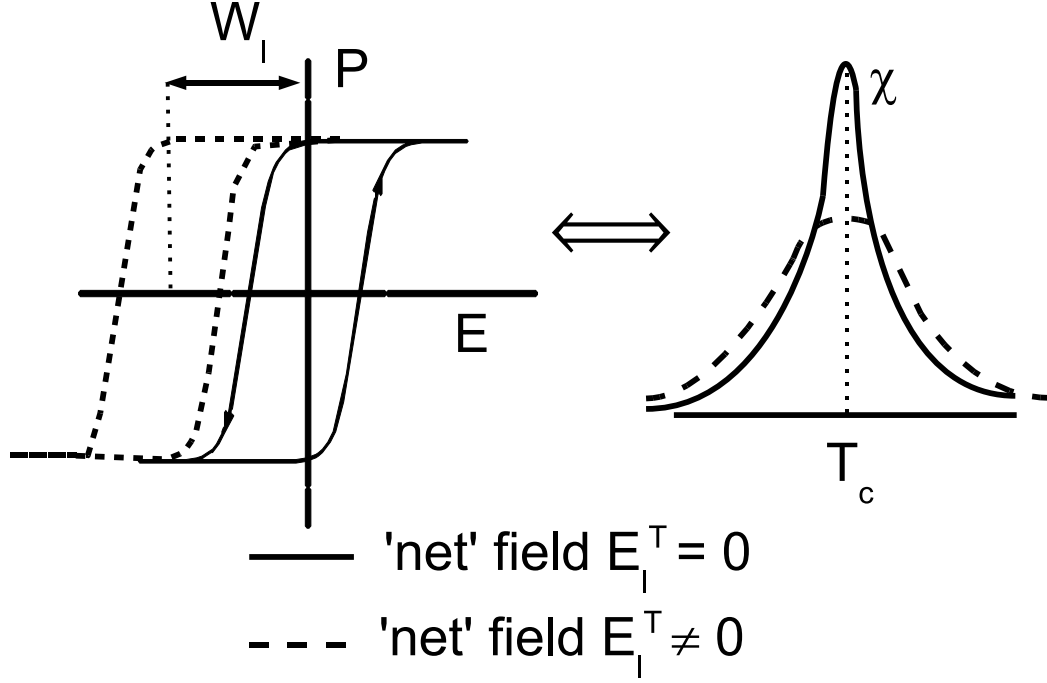
Figure 2.17: Schematic of a benchtop probe to test for the segregated strain model: the field offset (W_l) in the observed hysteresis loop can be tuned to zero by application of an electric field $E^*_{ext}(l) = -W_l$; in this case, the relative permittivity sharpens since the net (thickness-dependent) field $E_l^T = E^*_{ext}(l) + W_l = 0$.

near the film-substrate interface (see Fig. 2.2 and Fig. 2.3). This buffer layer itself breaks the up-down symmetry of the film, which then results in a nonzero effective field. To be more specific, it may be that an edge dislocation in the buffer layer produces a local polar distortion. This makes the buffer layer polar and produces a field in the uniform film. We then expect the strength of the effective bias field to be related to the areal density of dislocations, and thus to the magnitude of the homogeneous strain in the film.

As we have shown in Sec. 2.4.1, using the segregated strain model (see Figs 2.2 and 2.3) we recover the thickness-dependent dielectric properties of BST films consistent with those measured [106] and calculated using flexoelectric effects [81] within an inhomogeneous strain scenario (see Fig 2.16). Therefore, in order to determine which of these two models is applicable to a particular film, additional experimental characterization is necessary. The presence of strain gradients in

the BST films studied using flexoelectricity [81] was verified by x-ray analyses [121], though similar studies on different BST films (on different substrates) indicate the absence of such inhomogeneous strain. [122] Therefore it is clear that observations of thickness-dependent permittivities and polarizations are not enough to indicate the underlying strain profile of the ferroelectric film. Naturally, the presence and/or absence of strain gradients can be addressed directly by x-ray diffraction but this probe may not be always easily accessible or practical.

Here, we emphasize that the effective bias fields associated with these two strain models are spatially different (see Figs 2.16 and 2.3), and we will use this distinction to propose a benchtop experiment to distinguish between these two scenarios. In the inhomogeneous strain model, [81] the effective bias field is spatially nonuniform; more specifically, is proportional to the strain gradient via a flexoelectric coupling, and thus, has an exponentially decaying spatial profile within the film (see Fig 2.16). By contrast, in the segregated strain model (see Fig 2.3), the effective bias field is uniform from the edge of the buffer layer to the surface. Assuming that this effective bias field W_l is uniform in the majority of the film, one can tune an external electric field to the right value, $E_{ext}^*(l) = -W_l$, to create a net zero-field condition $[E_T(l) = E_{ext}^*(l) + W_l]$ where the specific value of the necessary external field would be thickness-dependent. Therefore there would exist an external field value $E_{ext}^*(l)$ when the hysteresis loop would no longer have a field offset; at this value of the applied external field, a sharp peak in the temperature dependence of the relative permittivity should be observed (Fig 2.17). We emphasize that this must be a unipolar hysteresis experiment, with single top and bottom electrodes; many measurements are performed across two top electrodes, namely, two series capacitors, where one would always be uncompensated. Another probe of the spatial uniformity of W would be to measure T_{ferro} as a function of E_{ext}; for a uniform effective bias field, there would be a sharp peak in T_{ferro}, as shown in Fig. 2.8. This pronounced peak would not be present for a spatially varying effective bias field $W(z)$ since the latter would have varying magnitude in the sample and no particular value of applied (uniform) E_{ext} could completely compensate for it everywhere in the film. Physically, we note that $W(z)$ could arise from coupling of the polarization to gradients in the strain, [81] in chemical composition, and

in temperature. [95, 118, 123] There do exist graded ferroelectric structures where such spatially varying quantities are explicitly present by design. Here, a charge offset is often observed in the charge-voltage hysteresis loops, [118] and this could serve as an indicator of underlying gradients in ferroelectric films if a suitable "charge origin" could be chosen as a reference.

We emphasize that we expect different films, with varying compositions, substrates, and growth conditions, to have diverse strain and effective bias field profiles. The inhomogeneous scenario may describe some, while others may be better modelled by the segregated strain approach; still others may exhibit intermediate behavior. By carefully monitoring growth conditions, it should be possible to control the density and spatial distribution of strain-relieving defects; in some case, it may even be feasible to kinetically inhibit them to obtain uniform coherently strained films. [15] We emphasize that in each case, the strain and effective bias field distributions must be carefully characterized for a full interpretation of the measured thickness-dependent dielectric behavior, and we have presented simple proposals for benchtop measurements to ascertain the importance of strain gradients in the films.

2.6 Summary

In conclusion, we have demonstrated that a segregated strain model (cf. Fig 2.2) describes the observed thickness-dependent dielectric properties of ferroelectric films as well as a previous model of inhomogeneous strain. [81] Therefore such thickness-dependent behavior is not signatory of underlying strain gradients, and more measurements must be performed to determine the strain profile in the film. If the effective bias field is spatially uniform, it can be compensated by the application of an applied external electric field $E^*_{ext}(l) = -W_l$, whose value will be dependent on the overall film thickness l. Benchtop experiments performed with $E_{ext} = E^*_{ext}(l)$ will yield bulk-like sharp dielectric responses. However, such compensation will not be possible if the effective bias field is spatially varying, since then its effects cannot be cancelled by the application of an external uniform field.

We have compared our results with experiment (BST on SRO) whenever possible and have also

made predictions for measurements on strained STO films with out-of-plane polarization. Agreement with existing *ab initio* calculations, when appropriate, has been good. The possibility of reentrant ferreoelectricity in strained STO films has also been discussed and we hope that this will be explored experimentally in the near future.

Our phenomenological study of planar films suggests that their thickness-dependent dielectric properties are not indicative of underlying inhomogeneous strain and are consistent with other strain profiles. We view this project as the beginning of a broader study of the physical consequences of boundary-induced effects in ferroelectrics of increasingly complex host topologies. The next step is to explore cases where the strain gradients will be induced by geometry, examples include curved films and cylindrical shells. Because of the coupling between the elastic and the electrical degrees of freedom in these systems, we expect tunable strain gradients to stabilize novel polarization configurations with rich phase behavior, and here, flexoelectric effects should definitely be investigated. More complex host geometries and boundary conditions are expected to favor more novel orderings and dielectric properties; the possibility of identifying and characterizing these features in three-dimensional ferroelectrics on the nanoscale could also be useful in the design of future ferroelectric memories. [124]

Chapter 3

Quantum Critical Paraelectrics and the Casimir Effect in Time

3.1 Introduction

The role of temperature in the vicinity of a quantum phase transition is distinct from that close to its classical counterpart, where it acts as a tuning parameter across the transition [see Eq.(1.6)]. Near a quantum critical point (QCP), temperature provides a low energy cutoff for quantum fluctuations; the associated *finite* time-scale is defined through the uncertainty relation $\Delta t \sim \frac{\hbar}{k_B T}$. This same phenomenon manifests itself as a boundary condition in the Feynman path integral; it is in this sense that temperature plays the role of a *finite-size effect in time* at a quantum critical point. [125–129] The interplay between the scale-invariant quantum critical fluctuations and the temporal boundary condition imposed by temperature is reminiscent of the Casimir effect,[130–132] where neutral metallic structures attract each other [133–137] due to zero-point vacuum fluctuations.

This chapter is organized as follows. In Sec. 3.2, we explore the observable ramifications of temperature as a temporal Casimir effect, applying it to the example of a quantum ferroelectric critical point (QFCP) where detailed interplay between theory and experiment is possible below, at and above the upper critical dimension. Our work is motivated by recent experiments on the quantum paraelectric (QPE) SrTiO$_3$ (STO) where $1/T^2$ behavior is measured in the dielectric susceptibility near the QFCP.[30–32] In Sec. 3.3, we show how this result is simply obtained using finite-size scaling (FSS) in time; more generally we present similar derivations of several measurable quantities, recovering results that have been previously derived using more technical diagrammatic,[138–141] large N [142], and renormalization group (RG) methods.[143, 144] In particular, we present a simple interpretation of finite-temperature crossover functions near quantum critical points previously found using ϵ-expansion techniques,[144] and link them to ongoing low-temperature experiments on quantum paraelectric materials. In Sec. 3.4, we illustrate these ideas using a Gaussian theory

to characterize the domain of influence of the QFCP and we present the full phase diagram. Next in Sec. 3.5, we expand upon previous work by tuning away from the QFCP, studying deviations from scaling; here we find that coupling between the soft polarization and long-wavelength acoustic phonon modes is relevant and can lead to a shift of phase boundaries and to a reentrant quantum ferroelectric (QFE) phase. Finally in Sec. 3.6, we end with a discussion of our results and with questions to be pursued in future work.

3.2   The Casimir Effect

The Casimir effect results from the interplay of zero-point fluctuations and boundary conditions, and leads to the attraction between two parallel conducting plates in a vacuum.[130, 145, 146] It was one of the first predicted, observable consequences of vacuum fluctuations. Because the Casimir force scales inversely proportionally to the fourth power of the plate separation a, it is only measurable when a is quite small (micron regime). Recently, the Casimir phenomenon has assumed a new importance in the design of nanoscale devices.[133–137, 147] Generalizations of the Casimir effect to critical systems with external constraints continue to be fruitful [131, 132, 148–150]. In this section, we revisit the Casimir effect, recovering previously derived results [130, 151–155], and show how it is related to the critical fluctuations of the polarization field in quantum paraelectrics.

3.2.1   The Casimir Coefficient

The Casimir effect results from the effect of boundary conditions on the zero-point fluctuation modes of the electromagnetic field. We will consider the simplest case of two parallel conducting plates. The energy, $\Delta\mathcal{E}$, is the finite difference between the zero-point energies with and without the plates,[130, 151–154] and the force is then the spatial derivative of $\Delta\mathcal{E}$. The component of the electric field parallel to the conducting plates must vanish. There are two sets of modes that satisfy this condition: the transverse electric (TE) and transverse magnetic (TM) modes where the electric or magnetic field are respectively parallel to the plates.[156] The electric field for the transverse

electric field modes is given by

$$\vec{E}^{\mathrm{TE}}(\vec{x}, z) = \sum_{\vec{q}_\perp, n>0} E_{\vec{q}n}(\hat{z} \times \hat{q}_\perp) e^{i\vec{q}_\perp \cdot \vec{x}} \sin\left(\frac{n\pi}{a} z\right), \qquad (n > 0) \tag{3.1}$$

where $\vec{x}$ and z are the co-ordinates parallel and perpendicular to the plates respectively, n is an integer, and $E_{\vec{q}n}$ is the Fourier amplitude of the fields. There is no $n = 0$ TE mode. The corresponding magnetic field is calculated using Faraday's equations $\vec{\nabla} \times \vec{E} = -\partial \vec{B}/\partial t$, or $\vec{B} = \dfrac{1}{i\omega}\vec{\nabla} \times \vec{E}$. The magnetic field for the TM field modes is given by

$$\vec{B}^{\mathrm{TM}}(\vec{x}, z) = \sum_{\vec{q}_\perp, n>0} B_{\vec{q}n}(\hat{z} \times \hat{q}_\perp) e^{i\vec{q}_\perp \cdot \vec{x}} \cos\left(\frac{n\pi}{a} z\right), \qquad (n \geq 0). \tag{3.2}$$

We note that there is one extra $n = 0$ TM mode. The corresponding electric fields are computed from Maxwell's displacement current equation $\vec{\nabla} \times \vec{B} = \dfrac{1}{c^2}\dfrac{\partial \vec{E}}{\partial t}$ or $\vec{E} = -\dfrac{c^2}{i\omega}(\vec{\nabla} \times \vec{B})$. The Fourier modes of these fluctuations thus involve a discrete set of wavevectors,

$$\vec{q}_n = (\vec{q}_\perp, q_{zn}), \tag{3.3}$$

where $q_{zn} = n\pi/a$ and n is an integer, leading to a discrete set of normal mode frequencies $\omega_{\vec{q}_\perp n} = c\sqrt{\vec{q}_\perp^2 + q_{zn}^2}$ [see Fig. 3.1], where c is the speed of light.

The zero-point energy of the fields inside the plates is given by

$$\mathcal{E}_C = \sum_{\vec{q}_\perp} \frac{\hbar\omega_{\vec{q}_\perp,0}}{2} + 2 \sum_{\vec{q}_\perp, n>0} \frac{\hbar\omega_{\vec{q}_\perp,n}}{2}, \tag{3.4}$$

where the first term is the zero point energy of the $n = 0$ TM mode, and the second term counts the zero point energy of the TM and TE modes with $n > 0$. We may rewrite these two terms as a sum over all n, both positive and negative, as follows

$$\mathcal{E}_C = \frac{\hbar c}{2} \sum_{n=-\infty}^{\infty} \sum_{\vec{q}_\perp} \sqrt{q_\perp^2 + q_{zn}^2}. \tag{3.5}$$
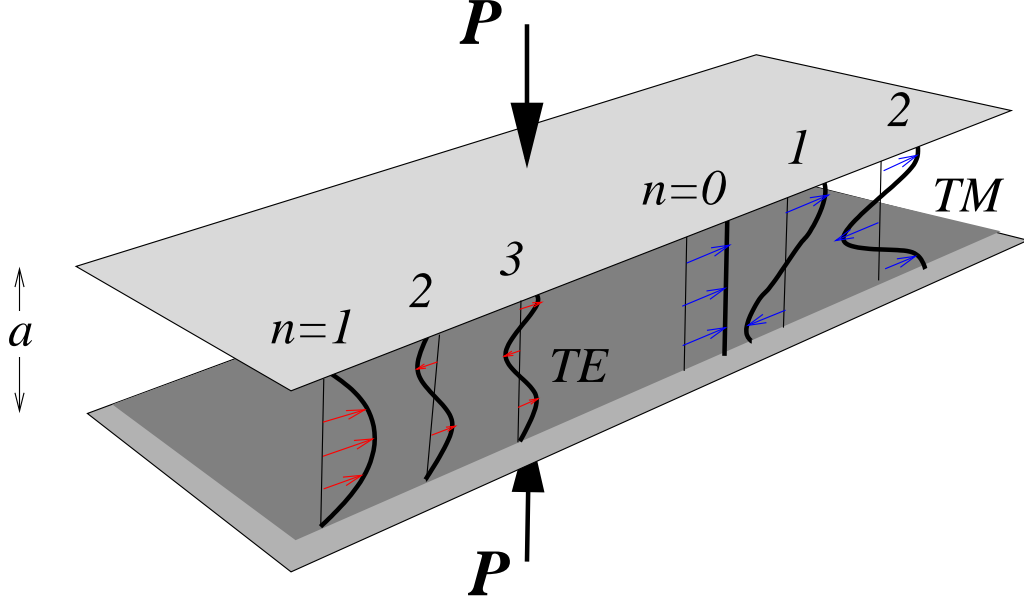
Figure 3.1: Schematic of the Casimir effect indicating that the normal modes of the electromagnetic field between two conducting plates occupy a discrete set of wavevectors. In the transverse electric (TE) modes the electric field lies parallel to the plates and $n \geq 1$. In the TM modes the magnetic field lies parallel to the plates and $n \geq 0$. The modification of the frequencies of the zero-point fluctuations by boundary conditions changes the energy of the system, creating a pressure on the plates.

In the continuum limit we let $\sum_{\vec{q}_\perp} \to A \int \frac{d^2 q_\perp}{(2\pi)^2}$, where A is the area of the plates, to obtain

$$\mathcal{E}_C = A \frac{\hbar c}{2} \sum_{n=-\infty}^{\infty} \int \frac{d^2 q_\perp}{(2\pi)^2} \sqrt{q_\perp^2 + q_{zn}^2}. \tag{3.6}$$

The quantity $\mathcal{E}_C/A$ determined from Eq. (3.6) is dimensionally of the form $[\mathcal{E}_C/A] = \hbar c[L^{-3}]$. Because a is the only length scale in the system, it follows that the change in the zero-point energy must have the form

$$\frac{\Delta \mathcal{E}_c}{A} = \mathcal{K} \frac{\hbar c}{a^3}. \tag{3.7}$$

The fact that this Casimir energy is sensitive to arbitrary interplate separation, a, is a direct consequence of the gaplessness, and thus the scale-free nature of the photon field.

The traditional calculation of $\mathcal{K}$ in the Casimir energy Eq. (3.7) is performed using a regularization procedure enforced by a zeta function.[130, 151, 153] Here, we present an alternative derivation

in which we calculate the necessary sums by exploiting the structure of the Bose function and the residue theorem of complex analysis. This approach is central to the Matsubara formalism[157] used to study many-body systems at finite temperature. Therefore let us take a brief diversion to describe the technique in general before applying it specifically towards the calculation of the Casimir coefficient.

3.2.2 The Matsubara Method

We begin by noting that the Bose function

$$n_B(z) = \frac{1}{e^{\hbar z / k_B T} - 1} \tag{3.8}$$

has poles on the imaginary axis [see Fig. 3.2] at $z = i\nu_n$, where $\nu_n = n2\pi k_B T / \hbar$, because

$$e^{i\hbar\nu_n / k_B T} = e^{2\pi ni} = 1. \tag{3.9}$$

Next we take

$$z = i\nu_n + \delta, \tag{3.10}$$

where δ is small so that z is slightly off the imaginary axis so that

$$n_B(i\nu_z + \delta) = \frac{1}{e^{\hbar\delta / k_B T} - 1} \approx \frac{k_B T}{\hbar\delta}, \tag{3.11}$$

from which we see that $k_B T$ is the residue at each of the poles $z = i\nu_n$ of $n_B(z)$, so that

$$n_B(z) = \sum_n \frac{k_B T}{\hbar(z - i\nu_n)}. \tag{3.12}$$

If we have a function, $F(z)$, that does not have poles on the imaginary axis, we can use the
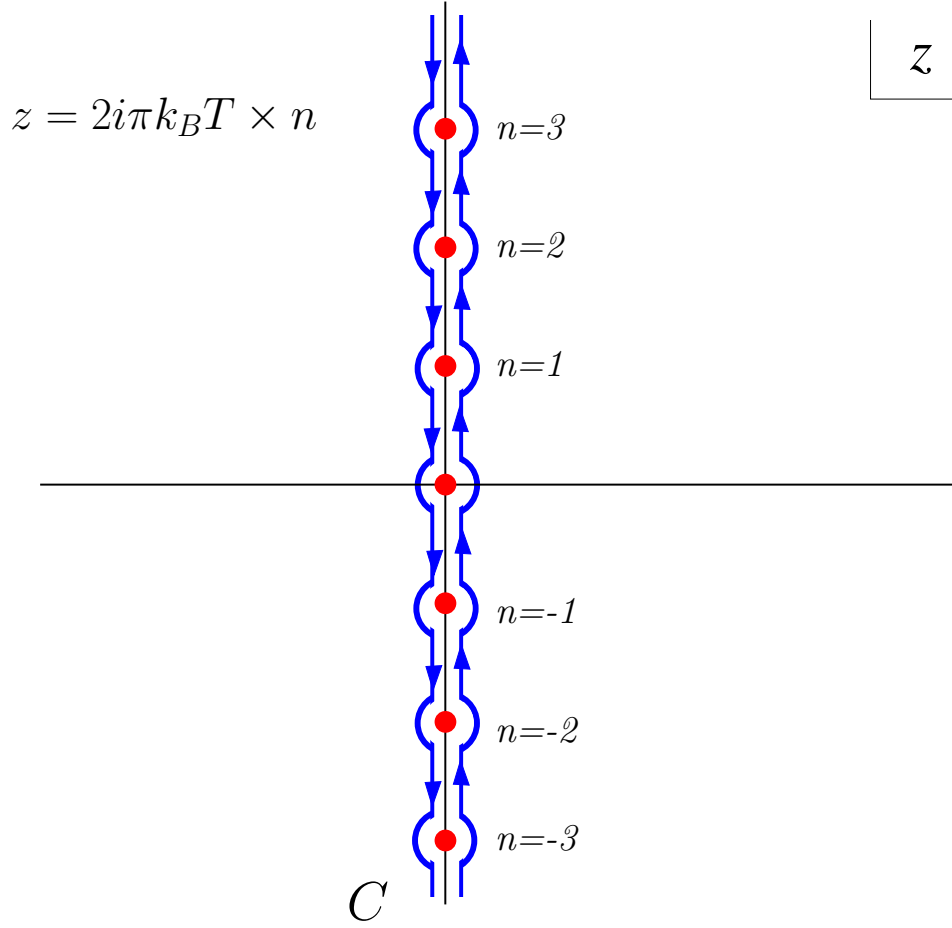
Figure 3.2: Contour integration path $\mathcal{C}$ used to sum over the Matsubara frequencies.

residue theorem and Eq. (3.12) to write

$$\oint_{\mathcal{C}} dz F(z) n_B(z) = 2\pi i \sum_n \frac{k_B T}{\hbar} F(i\nu_n),$$ (3.13)

where $\mathcal{C}$ is a contour that encircles the imaginary axis in a clockwise sense, as shown in Fig. 3.2.
Equation (3.13) can be rearranged to read

$$\sum_n F(i\nu_n) = \frac{\hbar}{k_B T} \oint_{\mathcal{C}} \frac{dz}{2\pi i} F(z) n_B(z),$$ (3.14)

which is a key result in the Matsubara approach used to evaluate sums that emerge in the study of
many-body systems at finite temperatures.[157]

We will now apply Eq. (3.14) to the specific case of the Casimir coefficient. To do so, we must identify the summations that we need to calculate. We begin with the zero-point energy per unit area (3.6)

$$\frac{\mathcal{E}_C}{A} = \frac{\hbar c}{2} \sum_n \int \frac{d^2 q_\perp}{(2\pi)^2} \sqrt{q_\perp^2 + q_{zn}^2}. \tag{3.15}$$

We are interested only in the *change* in the zero point energy as a result of the plates. In the limit of infinite plate separation ($a \to \infty$) the discrete interval in q_{zn}, $\Delta q_{zn} = \pi/a$, becomes infinitesimal, and the sum over n in Eq. (3.15) can be replaced by an integral $\sum_n = \sum_n \frac{\Delta q}{\pi/a} = \frac{a}{\pi} \int dq_z$. Therefore the change in the zero-point energy per unit area due to the presence of the plates is given by

$$\frac{\Delta \mathcal{E}_C}{A} = \frac{\mathcal{E}_C}{A} - \left. \frac{\mathcal{E}_C}{A} \right|_{a \to \infty} = \hbar c a \int \frac{d^2 q_\perp}{(2\pi)^2} \, I(q_\perp, a), \tag{3.16}$$

where

$$I(q_\perp, a) = \frac{1}{2a} \sum_n \sqrt{q_\perp^2 + q_{zn}^2} - \int \frac{dq_z}{2\pi} \sqrt{q_\perp^2 + q_z^2}. \tag{3.17}$$

By making this subtraction, we remove the ultraviolet divergences in the zero-point energy. By using the Matsubara method, we can reexpress the sum in Eq. (3.17) as

$$\frac{1}{2ac} \sum_n \sqrt{(cq_\perp)^2 + (cq_{zn})^2} = \frac{1}{\hbar c^2 \beta_C} \sum_n F(i\nu_n), \tag{3.18}$$

where

$$F(z) = \sqrt{c^2 q_\perp^2 - z^2}. \tag{3.19}$$

We associate the discrete wavevectors, q_{zn}, with a "Matsubara frequency" $cq_{zn} \equiv \nu_n$. Then

$$cq_{zn} = cn\frac{\pi}{a} \equiv n \left(\frac{2\pi k_B T_C}{\hbar} \right), \tag{3.20}$$
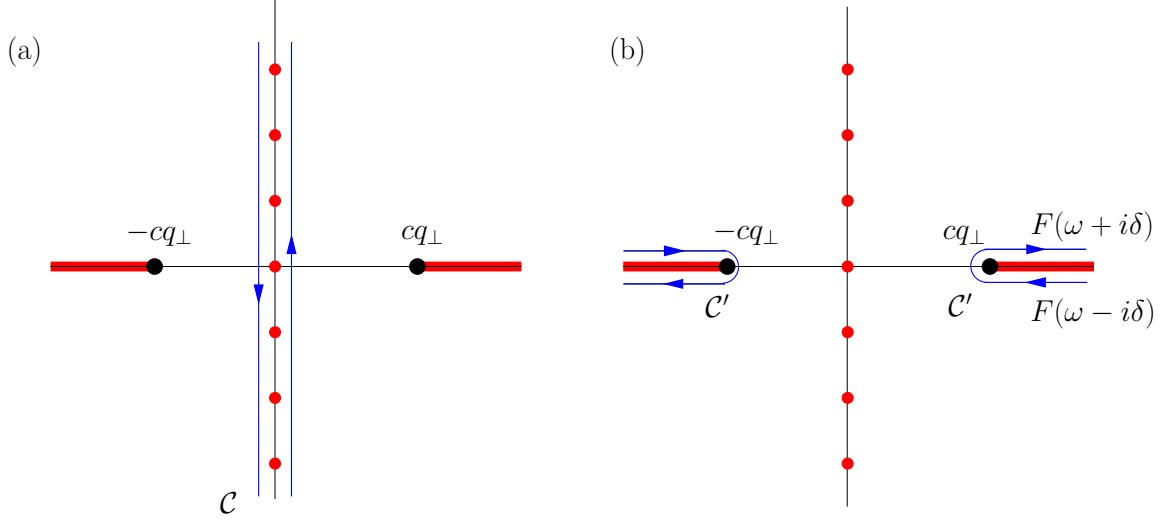
Figure 3.3: (a) Contour integration path $\mathcal{C}$ used to calculate $\frac{1}{\hbar\beta_C}\sum_n F(i\nu_n)$ in Eq. (3.23), where $F(z) = \sqrt{c^2 q_\perp^2 - z^2}$, showing branch cuts in $F(z)$ at $z = \pm c q_\perp$. (b) Distortion of the contour into contour C' that wraps around the branch cuts of $F(z)$. The integrand of the integral along the branch cuts is the difference $F(\omega + i\delta) - F(\omega - i\delta)$ between the value of $F(z)$ above and below the branch cut.

where the effective Casimir temperature is given by

$$k_B T_C = \frac{\hbar c}{2a}, \tag{3.21}$$

so that

$$\beta_C = \frac{1}{k_B T_C} \equiv \frac{2a}{\hbar c}. \tag{3.22}$$

We note that T_C scales inversely with the plate separation ($T_C \sim 1/2a$).

Following the Matsubara approach, the sum in Eq. (3.18) can now be rewritten as a contour integral[157] around the poles at $z = i\nu_n$ of the Bose function $n_B(z, \beta_C)$ yielding

$$\frac{1}{\hbar\beta_C}\sum_n F(i\nu_n) = \int_C \frac{dz}{2\pi i} F(z) n_B(z, \beta_C). \tag{3.23}$$

The second term in $I(q_\perp, a)$, Eq. (3.17), corresponds to the $a \to \infty$, or $\beta_C \to \infty$ limit of the

first term, and thus we may write

$$I(q_\perp, a) = \lim_{\beta' \to \infty} \left\{ \frac{1}{c^2} \int_C \frac{dz}{2\pi i} F(z) \left[n_B(z, \beta_C) - n_B(z, \beta') \right] \right\}. \tag{3.24}$$

The subtraction of the $\beta_C \to \infty$ limit of the integrand in Eq. (3.24) regulates the overall integral at large z, guaranteeing that the integrand around a contour at infinity vanishes. This condition permits us to evaluate the integral by distorting the contour around the branch cuts in $F(z)$ that extend from $z = \pm cq_\perp$ to infinity, as shown in Fig. (3.6). We then obtain

$$I(q_\perp, a) = \frac{1}{c^2} \left(\int_{-\infty}^{-cq_\perp} + \int_{cq_\perp}^{\infty} \right) \frac{d\omega}{2\pi i} [F(\omega + i\delta) - F(\omega - i\delta)] [n_B(\omega, \beta_C) - \{\beta_C \to \infty\}]. \tag{3.25}$$

To evaluate the branch cut, we note for $F(\omega \pm i\delta) = \sqrt{(cq_\perp)^2 - (\omega \pm i\delta)^2}$,

$$F(\omega + i\delta) - F(\omega - i\delta) = -2i\sqrt{\omega^2 - (cq_\perp)^2} \, \text{sgn}(\omega), \tag{3.26}$$

is an odd function of ω, which permits us to replace $n_B(\omega)$ by its odd part $n_B(\omega) + \frac{1}{2}$ to obtain

$$I(q_\perp, a) = \frac{1}{c^2} \left(\int_{-\infty}^{-cq_\perp} + \int_{cq_\perp}^{\infty} \right) \frac{d\omega}{2\pi i} [F(\omega + i\delta) - F(\omega - i\delta)] \left[\{n_B(\omega, \beta_C) + \frac{1}{2}\} - \{\beta_C \to \infty\} \right]. \tag{3.27}$$

Because the integrand is an even function of ω, we can replace this integral by twice the integral over positive ω to obtain

$$\begin{aligned} I(q_\perp, a) &= -\frac{2}{c^2} \int_{cq_\perp}^{\infty} \frac{d\omega}{\pi} \sqrt{\omega^2 - c^2 q_\perp^2} \left[\left(n_B(\omega, \beta_C) + \frac{1}{2} \right) - \{\beta_C \to \infty\} \right] \\ &= -\frac{2}{c^2} \int_{cq_\perp}^{\infty} \frac{d\omega}{\pi} \sqrt{\omega^2 - c^2 q_\perp^2} \, n_B(\omega, \beta_C). \end{aligned} \tag{3.28}$$

The change in zero point energy is then given by

$$\frac{\Delta \mathcal{E}_C}{A} = -2\hbar^2 \beta_C \int_{\omega > q_\perp} \frac{d^2 q_\perp \, d\omega}{(2\pi)^3} n_B(\omega, \beta_C) \sqrt{\omega^2 - c^2 q_\perp^2}, \tag{3.29}$$

where we have made the substitution $2a/c = \hbar\beta_C$. By carrying out the integral over $q_\perp$, we obtain

$$\frac{\Delta\mathcal{E}_C}{A} = -\frac{\hbar^2\beta_C}{6\pi^2c^2}\int d\omega\,\omega^3 n_B(\omega,\beta_C).$$ (3.30)

Rescaling the integral in Eq. (3.30) by changing variables to $x = \hbar\omega/k_BT$ and replacing $\beta_C = 2a/\hbar c$, we obtain

$$\frac{\Delta\mathcal{E}_C}{A} = -\frac{1}{6\pi^2\hbar^2\beta_C^3 c^2}\overbrace{\int dx\frac{x^3}{e^x-1}}^{\frac{\pi^4}{15}} = -\frac{\pi^2}{720}\frac{\hbar c}{a^3}$$ (3.31)

in numerical agreement with previous derivations.[130, 151–154] The associated force per unit area is then

$$\frac{F}{A} = \frac{d\Delta\mathcal{E}_c}{da} = \frac{\pi^2}{240}\frac{\hbar c}{a^4} = 1.3\times10^{-3}\frac{1}{(a/\mu m)^4}N/m^2$$ (3.32)

indicating that measurements of the Casimir force must be performed at plate separations at or below the micrometer length scale. [133–137, 147] When the two conducting plates are parallel, the force is attractive, but it can be repulsive in other situations.[158, 159]

3.2.3   The Casimir Effect and Black-Body Radiation

With $\beta_C^{-1} = k_BT_C = \hbar c/2a$ [Eq. (3.22)], the Casimir energy density [Eq. (3.30] becomes

$$\frac{\Delta E_C}{Aa} = -\frac{(k_BT_C)^4}{3\pi^2c^3\hbar^3}\int dx\,x^3 n(x),$$ (3.33)

and is similar to the thermal energy density of black-body radiation [12, 155] in a volume $V = aA$ at a finite temperature T_C [160]. The similarity between the Casimir and the blackbody energy density is testament to their common origin as boundary-condition effects. Traditionally we think of black body radiation as resulting from an excitation of thermal modes. Our calculation shows that the Casimir effect and blackbody radiation are both consequences of boundary conditions and the *redistribution* of zero-point fluctuation modes in the vacuum.

Recent experiments have observed the Casimir effect between parallel plates with a one micron separation ($a = 1\,\mu$m).[133–137, 147] The corresponding "Casimir temperature" for these experiments is

$$T_C = \frac{\hbar c}{2ak_B} \sim 1000\,\text{K}. \tag{3.34}$$

The Casimir effect at these length scales couples to the same photons that predominate in the blackbody spectrum at 1000 K. The boundary conditions imposed by the two phenomena on the electromagnetic field are almost identical.

More generally, zero-point fluctuations play a major role at quantum phase transitions.[126, 127, 129] The effect of finite temperature in the vicinity of a [$T = 0$] quantum critical point is the temporal analog of the Casimir phenomenon, a "Casimir effect in time," where temperature imposes temporal constraints on critical zero-point fluctuations. As we will see, there is an intimate connection between a finite temporal dimension and a nonzero temperature in a quantum system, [125–129] and this connection has many observable consequences on thermodynamic quantities for quantum critical systems at nonzero temperatures. Heuristically, this relation can be understood within the framework of the Heisenberg uncertainty principle

$$\Delta t \sim \frac{\hbar}{k_B T}, \tag{3.35}$$

where a thermal energy fluctuation leads to an upper cutoff in time, the Planck time, that is inversely proportional to the temperature. More formally, finite-temperature emerges in a path integral framework as a periodic boundary effect in imaginary time [see Sec. 3.2.4], which becomes particularly important near a quantum critical point where there exist quantum fluctuations on all spatial and temporal scales. Here, finite-temperature corresponds to the redistribution of quantum zero-point fluctuations due to the imposition of external constraints, and thus is analogous to the Casimir effect for two parallel metallic plates in vacuum. Running this argument the other way, we note that the removal of temporal modes by periodic finite boundary conditions generates a temperature [and thus entropy and thermal energy] in a system near a quantum critical point.

3.2.4 The Casimir Effect in Space and in Time

The Casimir effect is a boundary condition response of the electromagnetic vacuum, as we discuss in Sec. 3.2.1. The gapless nature of the photon spectrum means that the zero-point electromagnetic fluctuations are scale-invariant; the vacuum is literally in a quantum critical state. However, once the boundary conditions are introduced, the system is tuned away from criticality and develops a finite correlation length, ξ. The Coulomb interaction between two charges, the correlation function of the electromagnetic potential inside the cavity, is changed from the vacuum to the cavity as

$$V(q)_{free} \sim \langle \delta\phi_q \delta\phi_{-q} \rangle = \frac{e^2}{q^2} \qquad \rightarrow \qquad V(q)_{cavity} \sim \frac{e^2}{q_\perp^2 + \xi^{-2}} \qquad \xi = \frac{a}{\pi} \qquad (3.36)$$

where the plates have removed field modes and have introduced a finite ξ [proportional to the only length scale in the system, the interplate separation a]. In an analogous way, the partition function of a quantum system at finite temperatures is described by a Feynman path integral over the configurations of the fields in Euclidean space time [161] where temperature introduces a cutoff in the temporal direction. In Fig. 3.4 we present a visual comparison of the Casimir effect in space and in time. In both cases, the finite boundary effects induce the replacement of a continuum of quantum mechanical modes by a discrete spectrum of excitations.

In the quantum paraelectric of interest here, the path integral is taken over the space time configurations of the polarization field $P(\vec{x}, \tau)$,

$$Z = \sum_{\{P(x,\tau)\}} \exp\left[-\frac{S_E[P]}{\hbar} \right], \qquad (3.37)$$

where

$$S_E[P] = \int_0^{\hbar/k_B T} d\tau d^3x \, \mathcal{L}_E[P] \qquad (3.38)$$

and $\mathcal{L}_E[P]$ is the Lagrangian in Euclidean space time. The action per unit time is now the Free energy F of the system [see Table 3.1]. The salient point is that finite temperature imposes a *boundary condition in imaginary time* and the allowed configurations of the bosonic quantum fields

$$E(\vec{x}) = E_{\vec{k}n} e^{i\vec{q}_\perp \cdot \vec{x}} \sin\left(\frac{\pi n}{a}z\right)$$

$$P_n(\vec{x}, \tau) = P_n(\vec{x})e^{-i\nu_n \tau}$$
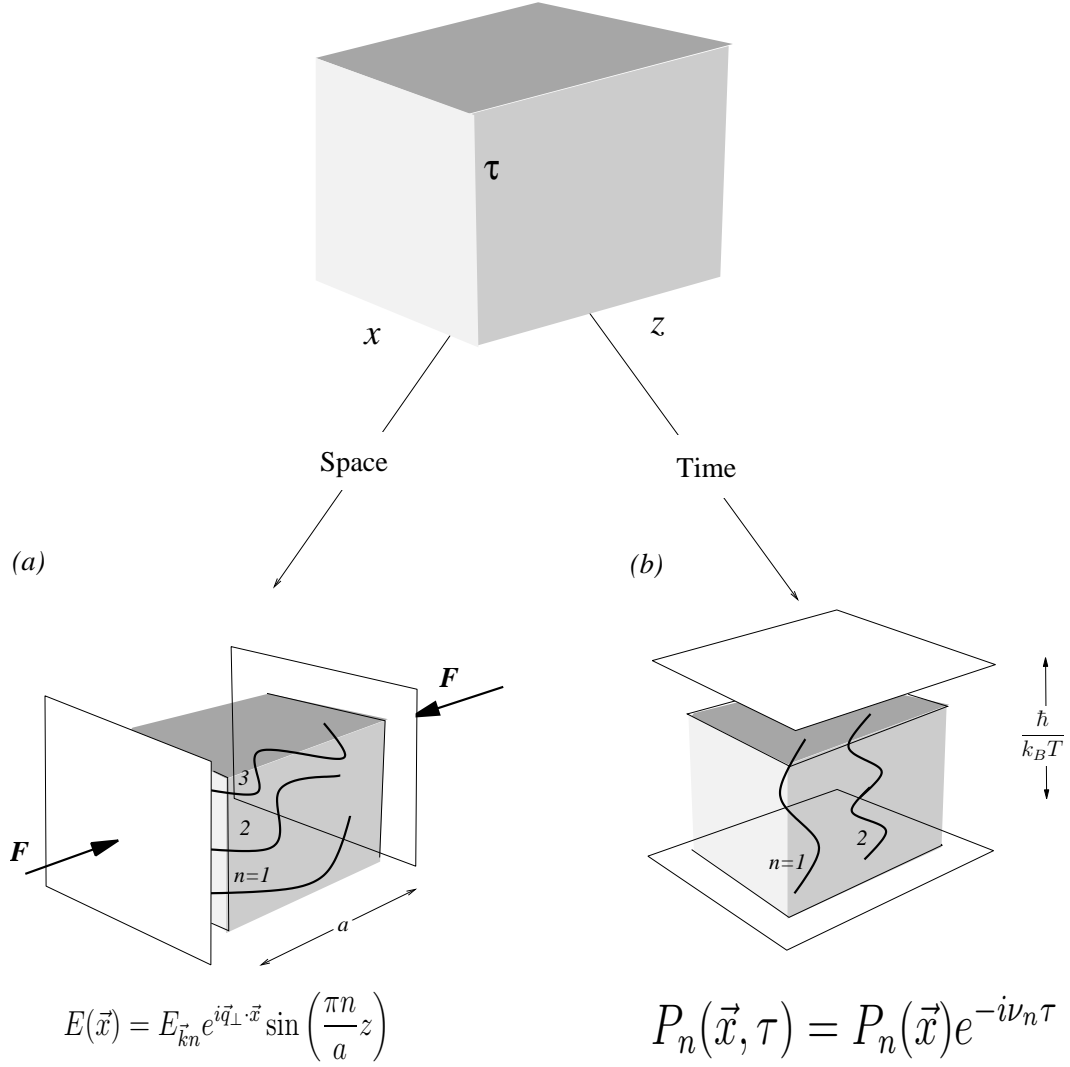
Figure 3.4: Casimir effect in space and time. (a) Imposition of spatial boundaries on the quantum critical electromagnetic field yields the conventional Casimir effect. (b) Imposition of temporal boundary conditions on a quantum critical paraelectric generates the effect of nonzero temperature.

are periodic in the imaginary time interval $\tau \in [0, \hbar\beta]$ ($\beta \equiv \frac{1}{k_B T}$) so that $\vec{P}(\vec{x}, \tau) = \vec{P}(\vec{x}, \tau + \hbar\beta)$, which permits the quantum fields are thus decomposed in terms of a discrete set of Fourier modes

$$P_n(\vec{x}, \tau) = \sum_{\vec{q},n} P(\vec{q}, i\nu_n)e^{i(\vec{q}\cdot\vec{x} - \nu_n\tau)} \tag{3.39}$$

where

$$\nu_n = n\left(\frac{2\pi k_B T}{\hbar}\right) \tag{3.40}$$

Table 3.1: Casimir effect and quantum criticality.

	Casimir effect	Finite-temperature effects near quantum criticality
Boundary condition	Space	Time
"S matrix"	$U = e^{-iE\bar{t}/\hbar}$	$Z = e^{-\beta F}$
Path Integral	$U = \int D[\phi] \exp\left[iS[\phi]/\hbar\right]$	$Z = \int D[P] \exp\left[-S_E[P]/\hbar\right]$
Action/time	E	$S_E/\beta\hbar = F$
Time interval	$\bar{t}(\to \infty)$	$\beta\hbar$
Spatial interval	a	∞
Discrete wavevector/frequency	$q_{zn} = (\pi/a)\,n$	$\nu_n = (2\pi k_B T/\hbar)\,n$

are the discrete Matsubara frequencies [see Eq. (3.20)]; we recall that at $T = 0$ the (imaginary) frequency spectrum is a continuum. The response and correlation functions in (discrete) imaginary frequency

$$\chi_E(\vec{q}, i\nu_n) = \langle P(\vec{q}, i\nu_n) P(-\vec{q}, -i\nu_n)\rangle \tag{3.41}$$

can be analytically continued to yield the retarded response function

$$\chi_E(\vec{q}, i\nu_n) \to \chi_E(\vec{q}, \omega) = \chi_E(\vec{q}, z)|_{z=\omega+i\delta} \tag{3.42}$$

where ω is a real frequency; for writing convenience we will subsequently drop the E subscript in χ, e.g., $\chi(\vec{q}, \omega) \equiv \chi_E(\vec{q}, \omega)$.

Like the parallel plates in the traditional Casimir effect, temperature removes modes of the field. In this case it is the frequencies not the wavevectors that assume a discrete character, namely,

$$q = (\vec{q}, \omega) \to (\vec{q}, i\nu_n), \tag{3.43}$$

where ν_n are defined in Eq. (3.40).

The Casimir analogy must be used with care. In contrast to the noninteracting nature of the

low-energy electromagnetic field, the modes at a typical QCP are interacting. In the conventional

Casimir effect, the finite correlation length is induced purely through the discretization of momenta

perpendicular to the plates. By contrast, at an interacting QCP, the discretization of Matsubara fre-

quencies imposed by the boundary condition generates the thermal fluctuations in the fields in real

time. These are fed back via interactions to generate a temperature-dependent gap in the spectrum

and a finite correlation time. Despite the complicated nature of this feedback, provided the under-

lying system is critical, temperature acting as a boundary condition in time will set the scale of the

finite correlation time

$$\xi_\tau = \frac{\hbar}{\kappa k_B T},\tag{3.44}$$

where κ is a constant. In cases where the quantum critical physics is universal, such as ferroelectrics

in dimensions below $d = 3$, we expect the coefficient κ to be also universal and independent of

the underlying strength of the mode-mode coupling. The "temporal confinement" of the fields

in imaginary time thus manifests itself as a finite response time in the real-time correlation and

response functions.

For the quantum paraelectric at the QFCP, the imaginary time correlation functions are scale-

invariant

$$\chi(\vec{q}, i\nu) = \left. \langle P(\vec{q}, i\nu)P(-\vec{q}, -i\nu) \rangle \right|_{T=0} \sim \frac{1}{\nu^2 + c_s^2 q^2}.\tag{3.45}$$

At a finite temperature this response function acquires a finite correlation time

$$\chi(\vec{q}, i\nu_n) \sim \frac{1}{\nu_n^2 + c_s^2 q^2 + \xi_\tau^{-2}}\tag{3.46}$$

where

$$\xi_\tau^{-2} = 3\gamma_c \left\{ \langle P^2 \rangle_{T \neq 0} - \langle P^2 \rangle_{T=0} \right\}\tag{3.47}$$

is determined by mode-mode interactions, where γ_c is the coupling constant describing the quartic

interactions between the modes, to be defined in Sec. 3.4. We note, as shall be shown explicitly in

Sec. 3.4, that for dimensions d such that $1 < d < 3$, the feedback will be sufficiently strong such

that ξ_τ will be *independent* of the coupling constant γ_c; by contrast for $d > 3$ the feedback effects are weak so that there will be a γ_c dependence of ξ_τ. The case $d = d_c^u = 3$ is marginal and will be discussed as a distinct case. At a temperature above a quantum critical point, the energy scale

$$\Delta(T) = \alpha k_B T \tag{3.48}$$

will set the size of the gap in the phonon dispersion relation. Here $\Delta(T) \sim \hbar \xi_\tau^{-1}$ and $\alpha = O(1)$ is a constant of proportionality.

Reconnecting to our previous discussion, we remark that real-time response functions from expressions like Eq. (3.46) are obtained by analytic continuation to real frequencies $i\nu_n \to \omega$. Since $\xi_\tau \sim \frac{1}{T}$, the dielectric susceptibility in the approach to the QFCP has the temperature dependence

$$\chi(T) = \left. \chi(q, i\nu_n) \right|_{q=0, \nu=0} \sim \xi_\tau^2 \propto \frac{1}{T^2}, \tag{3.49}$$

in contrast to the Curie form ($\chi \sim \frac{1}{T}$) associated with a classical paraelectric; this $1/T^2$ temperature-dependence was previously derived from a diagrammatic resummation,[138, 139], from analysis of the quantum spherical model[142] and from renormalization-group studies.[143, 144] We note that this $1/T^2$ behavior in the dielectric susceptibility of the quantum paraelectric has been observed experimentally.[31, 32, 162] We summarize in Table 3.1 the link between the conventional Casimir effect and finite-temperature behavior in the vicinity of a QCP.

3.3 Finite-Size Scaling in Time

The spatial confinement of order parameter fluctuations near a classical critical point has been studied as a "statistical mechanical Casimir effect", [131, 148, 149] and here we extend this treatment to study the influence of temperature near a QCP using FSS in imaginary time. This scaling approach is strictly valid in dimensions less than the upper critical dimension. Quantum critical ferroelectrics in $d = 3$ lie at the marginal dimension ($D = d + z = 4$), so the scaling results are valid up to logarithmic corrections, which we discuss later [see Sec. 3.6]; here $z = 1$ refers to a linear
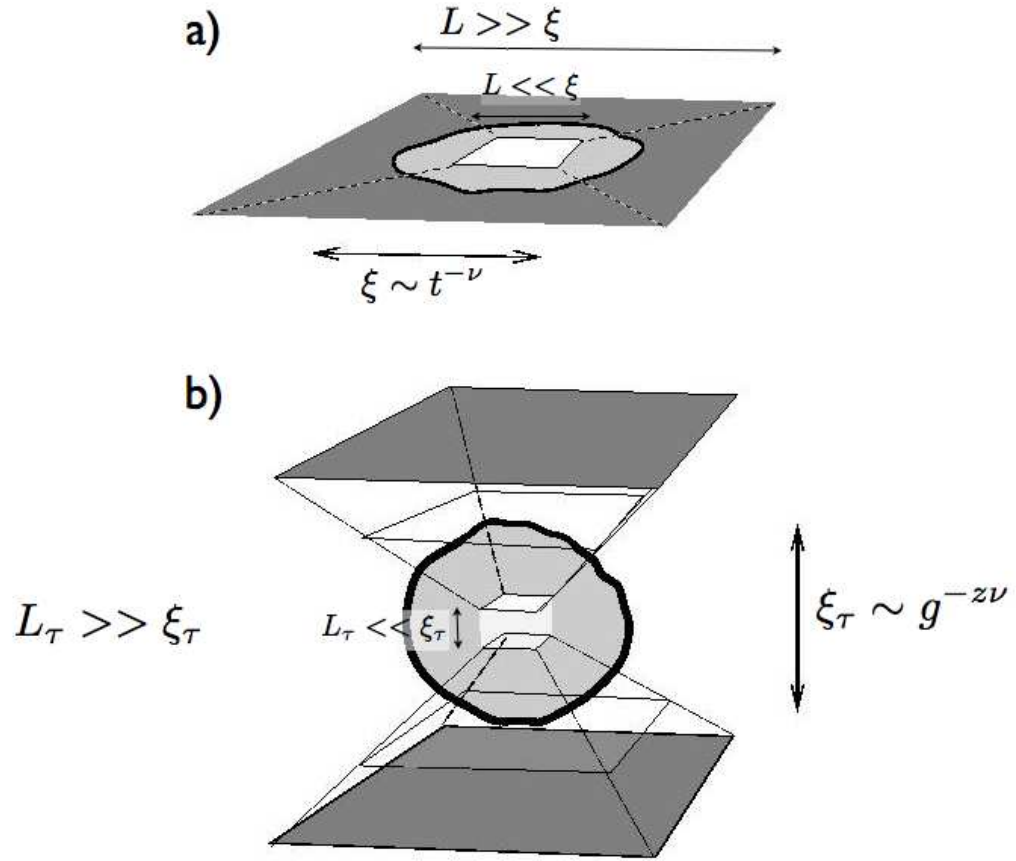
Figure 3.5: Schematic of finite-size effects (a) at a classical and at a (b) quantum critical point where the appropriate lengths are defined in the text.

dispersion relation, $\omega = c_s q$.

Following the standard FSS procedure,[125, 163, 164] we impose boundaries on the system near its critical point. For a classical system with tuning parameter $t = \frac{T - T_c}{T_c}$ and correlation length ξ, we confine it in a box of size L and then write the standard FSS scaling form

$$\chi = t^{-\gamma} f\left(\frac{L}{\xi}\right) \tag{3.50}$$

for the susceptibility.[125, 163–165] Similar reasoning can be used when a system is near its QCP. Here temperature is no longer a tuning parameter, this role is taken over by an external tuning field g. Temperature now assumes a new role as a boundary condition in time. Introducing a fixed L_τ [see Fig. 3.5(b)] associated with a finite T, while replacing $t \to g$, the quantum critical version of

Eq. (3.50) is

$$\chi = g^{-\gamma}\Phi\left(\frac{L_\tau}{\xi_\tau}\right),$$

(3.51)

where g is the tuning parameter. The dispersion relation $\omega = c_s q^z$ yields $[\xi_\tau] = [\xi^z]$; this combined with $\xi \sim g^{-\tilde{\nu}}$ leads to $\xi_\tau \sim g^{-z\tilde{\nu}}$. We therefore write

$$\chi = g^{-\gamma}\Phi\left(\frac{L_\tau}{g^{-z\tilde{\nu}}}\right),$$

(3.52)

where $\Phi(x) \sim x^p$ is a crossover function where p is determined by the limiting values of $\Phi(x)$; when $x \to 0$, we expect $\chi = \chi(L_\tau)$, whereas we should recover the zero-temperature result ($\chi \sim g^{-\gamma}$) when $x \to \infty$. Therefore we obtain

$$\chi \sim g^{-\gamma}\left(\frac{L_\tau}{g^{-z\tilde{\nu}}}\right)^{\frac{\gamma}{z\tilde{\nu}}} \sim L_\tau^{\frac{\gamma}{z\tilde{\nu}}} \sim T^{-\frac{\gamma}{z\tilde{\nu}}}$$

(3.53)

and the temperature-dependence ($L_\tau \propto 1/T$) emerges naturally from FSS arguments. Therefore a ($T = 0$) quantum critical point can influence thermodynamic properties of a system at finite T just as a finite-size system displays aspects of classical critical phenomena despite its spatial constraints. A schematic overview of the finite-size scaling arguments we have presented here is displayed in Fig. 3.6.

The FSS approach can also yield the T-dependences of the specific heat and the polarization of a quantum critical paraelectric. At a finite-temperature phase transition, to obtain the specific-heat capacity of a finite size box with $L << \xi$, we write $f \sim t^{2-\alpha}F(L/\xi) \sim t^{2-\alpha}\left(\frac{L}{t^{-\nu}}\right)^{-(2-\alpha)/\tilde{\nu}} \sim L^{-(2-\alpha)/\tilde{\nu}}$. In a similar spirit, applying the quantum FSS analogies ($L \to L_\tau$, $t \to g, \xi \to \xi_\tau^z = g^{-z\tilde{\nu}}$), we obtain

$$f_{qm}(L_\tau) \sim g^{2-\alpha}\left(\frac{L_\tau}{g^{-z\tilde{\nu}}}\right)^{-\frac{(2-\alpha)}{z\tilde{\nu}}} \sim L_\tau^{-\frac{2-\alpha}{z\tilde{\nu}}} \sim T^{\frac{2-\alpha}{z\tilde{\nu}}}$$

(3.54)

so that the T-dependent specific heat is

$$c_v(T) = T\partial^2 f_{qm}/\partial T^2 \sim T^{\frac{2-\alpha}{z\tilde{\nu}}-1}$$

(3.55)

Classical to Quantum Scaling

T

g

Classic	Quantum
t	g

$$\xi \sim t^{-\tilde{\nu}} \qquad \xi_\tau \sim g^{-z\tilde{\nu}}$$

$$\chi = t^{-\gamma}\Phi\left(\frac{L}{\xi}\right) \qquad \chi = g^{-\gamma}\tilde{\Phi}\left(\frac{L_\tau}{\xi_\tau}\right)$$

$$L << \xi \qquad\qquad L_\tau << \xi_\tau$$

$$\chi \sim L^{\gamma/\tilde{\nu}} \qquad \chi \sim L_\tau^{\gamma/z\tilde{\nu}} \sim T^{-\frac{\gamma}{z\tilde{\nu}}}$$
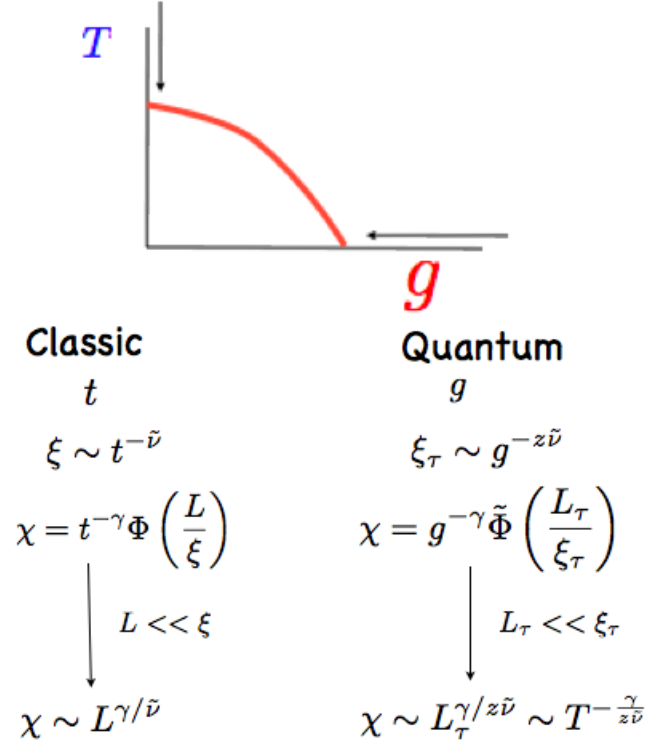
Figure 3.6: Overview of the finite-size scaling at classical and quantum critical points; here $\tilde{\nu}$ is the exponent associated with the spatial correlation length since ν has already been used in the text as a frequency.

in the vicinity of a QCP. Similarly the T dependence of the polarization is $P(T) \sim T^{\frac{\beta}{z\tilde{\nu}}}$ and we note that $P(E) = \partial f_{qm}/\partial E|_{g=0} \sim E^{1/\delta}$ is T independent, since finite-temperature scaling does not affect field behavior.

Simple scaling relations at classical and quantum criticality are summarized in Fig. 3.6. The key notion is that at a QCP, finite T effects correspond to the limit $L_\tau << \xi_\tau$; in this case L_τ becomes the effective correlation length in time, and the T dependences follow. We note that we expect this finite-size approach to work for dimensions $d < d_c^u$ where there will be logarithmic corrections to scaling in the upper critical dimension d_c^u.

Let us now be more specific with exponents for the quantum paraelectric case. At criticality the observed T dependence of the paraelectric susceptibility (χ) can be found by a soft-mode analysis,

Table 3.2: Observables for a $D = 4$ QPE in the vicinity of a QFCP.

Observable	T dependences (g=0)	g dependences (T=0)
Polarization	$P \sim T^1$	$P \sim g^{1/2}$
Susceptibility	$\chi \sim T^{-2}$	$\chi \sim g^{-1}$
	$P \sim E^{1/3}$	
	$\chi(\omega, T) = \left(1/\omega^2\right) F\left(\omega/T\right)$	

[43, 91] and therefore the exponents for the quantum paraelectric are those of the quantum spherical model.[142] For the case of interest ($D = d + z = 3 + 1 = 4$), the quantum spherical model has exponents $\tilde{\nu} = 1/(D - 2) = 1/2$ and $\gamma = 2/(D - 2) = 1$, so that $\gamma_{th} = \frac{\gamma}{z\tilde{\nu}} = 2$ and we recover the $\chi^{-1} \sim T^2$ scaling found earlier. Other specific T dependences are displayed in Table 3.2. For $d = 3$, we have $g \sim T^2$; this relation was experimentaly observed [30, 84] in STO. Finally we note that the FSS that we have discussed suggests the "$\frac{\omega}{T}$" scaling form

$$\chi(\omega, T) = \frac{1}{\omega^2} F\left(\frac{\omega}{T}\right) \tag{3.56}$$

that is similar to that observed in other systems at quantum criticality;[166, 167] this was previously derived by more technical methods.[144] Predictions for experiment are summarized in Table 3.2. We note that since we are in the upper critical dimension, there will be logarithmic corrections to this scaling but we do not expect these to be experimentally important for the temperature dependences described here; however they will be considered later in Sec. 3.6.

3.4 Gaussian Theory: Illustration of Temperature as a Boundary Effect

3.4.1 Gap Equation

In this section we use the self-consistent Gaussian theory to illustrate how the $\chi(T)$ found via FSS in time appears from a more microscopic approach; we also study the crossover behavior between the

classical and the quantum critical points. This approach is equivalent to the self-consistent one-loop approximation[168] that is used in the context of metallic magnetism.

The soft-mode treatment has been described extensively elsewhere;[43, 91, 168] here we briefly outline the derivation of the gap equation. The Lagrangian in Euclidean space time, $\mathcal{L}_E$ in Eq. (3.38), for displacive ferroelectrics is the ϕ^4 model:

$$\mathcal{L}_E \to \frac{1}{2}\left[(\partial_\tau P)^2 + (\nabla P)^2 + rP^2\right] + \frac{\gamma_c}{4}P^4, \tag{3.57}$$

which determines the partition function. Notice that in writing Eq. (3.57), we have chosen rescaled units in which the characteristic speed of the soft mode $c_s = 1$. In a self-consistent Hartree theory, interaction feedback is introduced via its renormalization of quadratic terms; this procedure is equivalent to replacing $\mathcal{L}_E$ by the Gaussian Lagrangian

$$\mathcal{L}_G = \frac{1}{2}P\left[-\partial_\tau^2 - \nabla^2 + r + \Sigma\right]P \tag{3.58}$$

where

$$\Sigma = 3\gamma_c\langle P^2\rangle \tag{3.59}$$

is the Hartree self-energy [see Fig. 3.7]. We note that this mode-mode coupling theory is exact for the "spherical model" generalization of ϕ^4 theory in which the order parameter has N components and N is taken to infinity.

The Green's function can now be determined from Dyson's equation, shown diagrammatically in Fig. 3.7, and takes the form

$$G(q) \equiv G(\vec{q}, i\nu_n) = \left[(i\nu_n)^2 - q^2 - r - \Sigma\right]^{-1}, \tag{3.60}$$

so the action is diagonalized in this basis. The poles of $G(\vec{q}, \omega)$ determine the dispersion relation ω_q
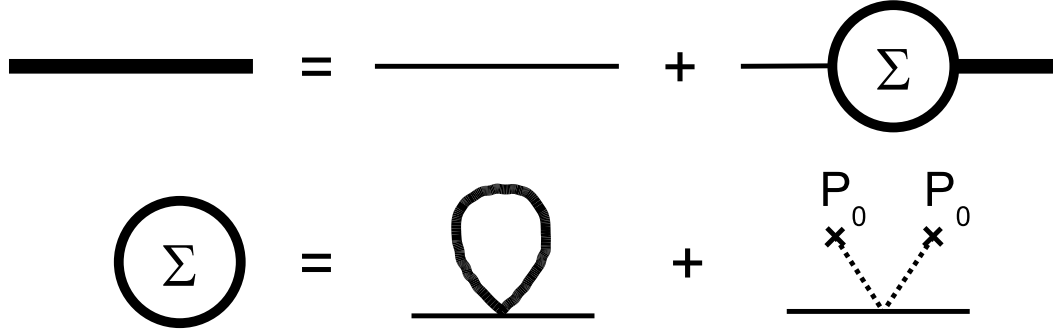
Figure 3.7: Diagrammatic representation of (a) the Dyson equation and (b) the Gaussian self-energy where $P_0 = 0$ in the paraelectric state (and is finite in the ferrelectric phase).

for the displacive polarization modes

$$\omega_q^2 = q^2 + \Delta^2, \tag{3.61}$$

where here we have introduced the gap function

$$\Delta^2(r, T) = r + \Sigma(r, T). \tag{3.62}$$

This quantity vanishes at both quantum and classical critical points where there are scale-free (gapless) fluctuations. At the quantum critical point where $T_c = 0$, $\Delta(r_c, 0) = r_c + \Sigma(r_c, T = 0)$, so that we can eliminate $r_c = -\Sigma(r_c, T = 0)$, to obtain

$$\Delta^2(r, T) = \Omega_0^2 + [\Sigma(r, T) - \Sigma(r_c, 0)], \tag{3.63}$$

where $\Omega_0^2 = (r - r_c) = g$.

The amplitude of the polarization fluctuations is given by

$$\langle P^2 \rangle = -G(0, 0) = -\frac{1}{\beta V} \sum_q G(q) e^{iqx}|_{x=0}, \tag{3.64}$$

so the self-consistency Eq. (3.59) condition $\Sigma = 3\gamma_c \langle P^2 \rangle$ can now be written

$$\Sigma(r,T) = (-3\gamma_c)T \sum_n \int \frac{d^d q}{(2\pi)^d} G(q, i\nu_n), \tag{3.65}$$

where $\Sigma(r,T)$ is the temperature-dependent self-energy. By converting the discrete Matsubara summation to a contour integral, deformed around the poles $z = \pm\omega(q)$ in the dispersion relation, we can convert this expression to the form

$$\Sigma(r,T) = 3\gamma_c \int \frac{d^d q}{(2\pi)^d} \frac{\left[n_B(\omega_q) + \frac{1}{2}\right]}{\omega_q}, \tag{3.66}$$

where we denote $n_B(\omega) \equiv n_B(\omega, \beta) = 1/(e^{\beta\omega} - 1)$. At the quantum critical point ($r = r_c$ and $T = 0$), we have $\omega_q = q$ and $n(\omega_q) = 0$ so that

$$\Sigma(r_c, 0) = 3\gamma_c \int \frac{d^d q}{(2\pi)^d} \frac{1}{2q}, \tag{3.67}$$

and using Eq. (3.63), we can write the gap function as

$$\begin{aligned}
\Delta^2 &= \Omega_0^2 + 3\gamma_c \int \frac{d^d q}{(2\pi)^d} \left(\frac{\left[n_B(\omega_q) + \frac{1}{2}\right]}{\omega_q} - \frac{1}{2q} \right), \\
\omega_q &= \sqrt{q^2 + \Delta^2}.
\end{aligned} \tag{3.68}$$

3.4.2 T Dependence of the Gap at the QCP

In the paraelectric phases, we can use the temperature-dependent gap to determine the dielectric susceptibility χ. Writing

$$\chi = \chi(q, \omega)\Big|_{\vec{q}, \omega=0} = \langle P(q)P(-q) \rangle \Big|_{q=0} = -G(\vec{q}, \omega)\Big|_{\vec{q}, \omega=0}, \tag{3.69}$$

we use Eqs. (3.60) and (3.62) to express it as

$$\chi^{-1}(r,T) = \Delta^2(r,T). \tag{3.70}$$

At the quantum critical point $\Omega_0^2 = 0$, so the gap equation Eq. (3.68) becomes

$$\Delta^2(r_c, T) = 3\gamma_c \int_0^{q<q_{max}} \frac{d^dq}{(2\pi)^d} \left\{ \frac{\left[n_B(\omega_q) + \frac{1}{2}\right]}{\sqrt{q^2 + \Delta^2}} - \frac{1}{2q} \right\}, \tag{3.71}$$

where we have inputted the dispersion relation, Eq. (3.61), for ω_q in Eq. (3.71). We notice that both thermal and quantum fluctuations contribute to this expression.

Even though the mean-field gap equation is only formally exact in the spherical mean-field limit, it is sufficient to illustrate the qualitative influence of T on the gap at the QCP. In order to explore the cutoff dependence of Eq. (3.71), we note that in the ultraviolet limit of interest, the last two terms can be expressed as

$$\frac{1}{2} \left\{ \frac{1}{\omega_q} - \frac{1}{q} \right\} = -\frac{\Delta^2}{4q^3}, \tag{3.72}$$

where there is complete cancellation when $\Delta = 0$ exactly at the QCP. However just slightly away from it, when Δ is finite, Eq. (3.72) leads to a q_{max}^{d-3} scaling dependence of the integral in Eq. (3.71); therefore the cutoff is required to ensure that Eq. (3.71) is finite in dimensions $d > 3$. However, in dimensions $d < 3$, this integral is convergent in the ultraviolet and the upper cutoff in Eq. (3.71) can be entirely removed. Thus, for $d < 3$, the only scale in the problem is temperature itself. The integral is also convergent in the infrared provided $d > 1$. The spatial dimensions $d = 1$ and $d = 3$ correspond to space time dimensions $D = d + 1 = 2$ and $D = d + 1 = 4$, which are the well-known lower and upper critical dimensions of the ϕ^4 theory. This provides us with a dimensional window $1 < d < 3$ where inverse temperature acts as a cutoff in time. In this range, the temperature dependence of the gap

$$\Delta(T) = \alpha_d T \tag{3.73}$$

is independent of the strength of the coupling constant γ_c and the cutoff, a feature that can be illustrated already within mode-coupling theory. Recalling that $\Delta(T) = \frac{\alpha}{L_\tau}$ and $\alpha \equiv \alpha_d$ [see Eq. (3.48) and Fig. 3.4], we note that confirmation of Eq. (3.73) is consistent with our earlier discussion [see after Eq. (3.47)] that ξ_τ is independent of coupling constant; in this dimensional window,
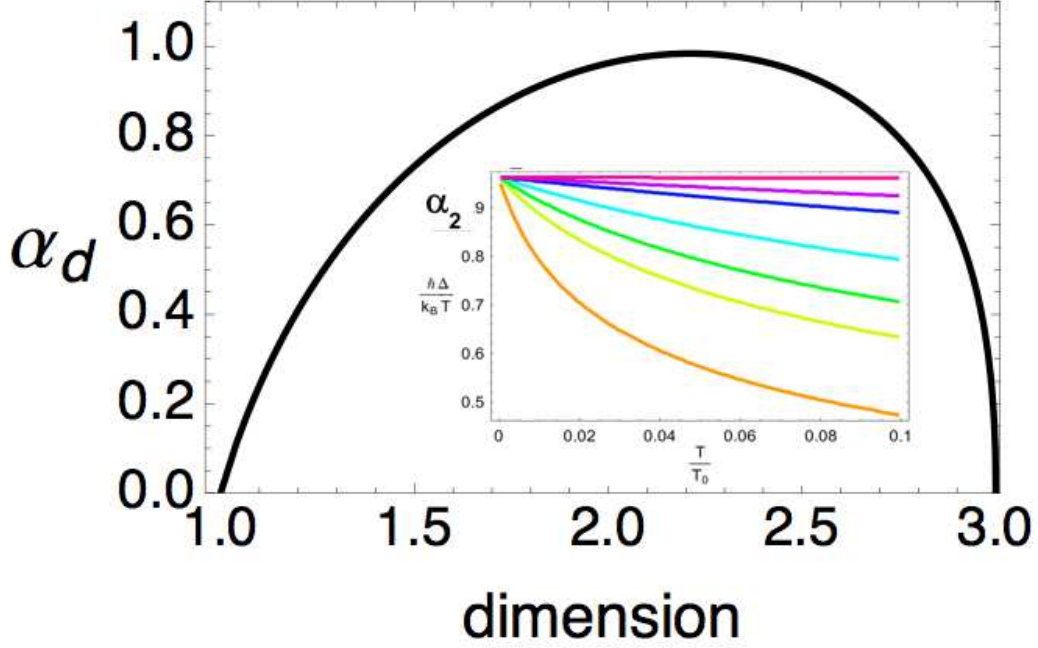
Figure 3.8: Dependence of $\alpha_d(T \to 0)$ on dimensionality d. Inset: T dependence of Δ/T for $d = 2$ and coupling constants in the range $0.01 < \frac{\gamma_c(d=2)}{q_{max}} < 5.0$; here T_0 is the temperature scale where $\xi \sim a$ and we note that $\lim_{T \to 0} \alpha_2$ is independent of γ_c.

temperature is a boundary effect in (imaginary) time and is the only temporal scale in the problem.

In order to calculate α_d, we rewrite the gap equation at criticality as

$$\frac{\Delta^2}{T^2} = \alpha^2 = \frac{3\gamma_c}{T^2}\Gamma_d \int_0^\infty \frac{q^{d-1}dq}{(2\pi)^d} \left\{ \frac{\left[n_B(\omega_q) + \frac{1}{2}\right]}{\omega_q} - \frac{1}{2q} \right\}, \tag{3.74}$$

where $\Gamma_d q^{d-1}dq$ ($\Gamma_d = \frac{2\pi^{d/2}}{\Gamma(d/2)}$) is the d-dimensional volume measure. Rescaling $\Delta = \alpha_d T$ and $q = uT$, we obtain

$$F_d[\alpha] = T^{3-d}\alpha_d^2/\gamma_c \tag{3.75}$$

where

$$F_d[\alpha] = \frac{3}{(2\sqrt{\pi})^d \Gamma(d/2)} \int_0^\infty u^{d-1} du \left\{ \frac{\coth(\frac{1}{2}\sqrt{u^2 + \alpha^2})}{\sqrt{u^2 + \alpha^2}} - \frac{1}{u} \right\}. \tag{3.76}$$

Notice that for $d = 3 - \epsilon$ [$d \to 3$], Eq. (3.76) contains a singularity of $O(\alpha^2/\epsilon)$. Therefore we split

off the singular part of Eq. (3.76) as follows

$$F_d[\alpha] = \frac{3}{(2\sqrt{\pi})^d \Gamma(d/2)} \left[\int_0^\infty u^{d-1} du \left(\frac{\coth(\frac{1}{2}\sqrt{u^2 + \alpha^2}) - 1}{\sqrt{u^2 + \alpha^2}} \right) \right.$$

$$+ \overbrace{\int_0^\infty u^{d-1} du \left(\frac{1}{\sqrt{u^2 + \alpha^2}} - \frac{1}{u} \right)}^{\frac{\alpha^{d-1}}{2\sqrt{\pi}} \Gamma(\frac{d}{2}) \Gamma(\frac{1-d}{2})} \left. \right], \tag{3.77}$$

yielding

$$F_d[\alpha] = \frac{3}{(2\sqrt{\pi})^d \Gamma(d/2)} \left[\int_0^\infty u^{d-1} du \left(\frac{\coth(\frac{1}{2}\sqrt{u^2 + \alpha^2}) - 1}{\sqrt{u^2 + \alpha^2}} \right) \right.$$

$$\left. - \frac{12}{(2\sqrt{\pi})^{d+1}} \alpha^{d-1} \left(\frac{\Gamma\left(\frac{5-d}{2}\right)}{(d-1)(3-d)} \right) \right], \tag{3.78}$$

provided ($1 \leq d \leq 3$). The first term in this expression is a smooth positive function of d and α,

whereas the second is a singular negative function of d with poles at $d = 1$ and $d = 3$. For $d < 3$,

the temperature prefactor on the right-hand side of Eq. (3.75) vanishes $T \to 0$, so a consistent

solution requires α_d to satisfy

$$F_d[\alpha_d] = 0. \tag{3.79}$$

In Fig. 3.8 we display the dependence of α_d on dimensionality $1 < d < 3$. We notice that α_d

goes to zero as the dimension approaches the lower critical dimension $d_c^l = 1$, and α_d vanishes in

the vicinity of $d \sim 3$ as $\alpha_d \sim \sqrt{3 - d}$, consistent with previous ϵ calculations [144]. At a small

finite temperature, we can expand around $\alpha = \alpha_d + \delta\alpha(T)$, to obtain

$$\Delta(T) = \alpha_d T + \left(\frac{\alpha_d^2}{\gamma_c F'[\alpha_d]} \right) T^{4-d}. \tag{3.80}$$

Thus in dimensions $d < 3$, the dominant low-temperature behavior is independent of γ_c, the strength

of the mode-mode coupling, which enters into the subleading temperature dependence. The temperature dependence of the gap in two dimensions is shown in the inset of Fig. 3.8, where we see that $\lim_{T \to 0} \alpha_2 \equiv 0.96$ is the same for all couplings.

For $d = 3$, the linear coefficient of $\Delta(T)$ depends on γ_c, becoming independent of γ_c in the limit that $\gamma_c \to \infty$; here we have neglected logarithmic corrections in α_3. We remark that here we are presenting and expanding a previous analysis[142], noting that the γ_c independence of α_d for $d \leq 3$ can be understood via the insight that temperature is a boundary effect in time. According to Eqs. (3.75) and (3.76), we write $\alpha_3^2 = \gamma_c F_3[\alpha]$ and solve for α_3 in the limit of upper cutoff $u_{max} = q_{max}/T \equiv 2\pi T_0/T >> \alpha_3$,

$$\alpha_3(T, \gamma_c) \sim \sqrt{\frac{\gamma_c}{1 + \gamma_c(\frac{3}{8\pi^2}) \ln(\frac{4\pi T_0}{T})}}. \tag{3.81}$$

In the limit of strong coupling, $\alpha_3 \sim \left[\ln(\frac{4\pi T_0}{T}) \right]^{-1/2}$ is γ_c independent. For weak coupling, the situation relevant here, α_3 is indeed a function of γ_c but remains independent of temperature so that $\Delta \sim T$ according to Eq. (3.73); temperature dependences derived here should therefore be in agreement with those found from a scaling perspective whenever direct comparison is possible.

3.4.3 Temperature-Dependent Dielectric Susceptibility

To provide an explicit illustration of the above calculations, we now use Eqs. (3.68) and (3.70) to numerically determine the temperature-dependent paraelectric susceptibility in the approach to the quantum critical point (QCP) in $d = 3$. We obtain $\chi^{-1}(T) = \Delta^2 \sim T^2$ for the approach $r = r_c$ in agreement with previous results and discussion. We note that a similar analysis in the vicinity of the classical phase transition leads to the expected Curie susceptibility $[\chi^{-1}(T \to T_c^+ >> 0) \sim T]$ since in this (high) temperature regime the Bose function in Eq. (3.71) scales as $\frac{T}{\omega}$. We also remark that if we assume that $\omega \equiv \tilde{\omega}_0$ with no q dependence then we recover the Barrett[169] expression $\chi^{-1} \sim A + B \coth \frac{\hbar \tilde{\omega}_0}{k_B T}$; because the disperson is constant and q independent this approach is not applicable near quantum criticality where the gap vanishes and the q dependence

becomes important.

One more point needs to be considered before we proceed with our self-consistent Hartree theory. In the self-consistent Hartree theory (SCHT) of the ferroelectric phase, the polarization field P_0 acquires a nonzero value. P_0 enters the Lagrangian $\mathcal{L}_E$ in Eq. (3.57) as $P = P_0 + \delta P$, where δP are fluctuations of the polarization field around its mean value, P_0 [$P_0 = 0$ in the paraelectric phase]. The self energy Eq. (3.59) becomes

$$\Sigma = 3\gamma_c \langle P^2 \rangle = 3\gamma_c \left(P_0^2 + \langle \delta P^2 \rangle \right) \tag{3.82}$$

as indicated diagrammatically in Fig. 3.7. The equilibrium value P_0 is easily obtained by introducing an electric field into the Lagrangian by replacing $\mathcal{L}_E \to \mathcal{L}_E + E \cdot P$, then seeking the stationary point $\delta S / \delta P_0 = 0$ which gives $\langle r P_0 + 3\gamma_c \delta P^2 P_0 + \gamma_c P_0^3 - E \rangle = 0$, or

$$r + \Sigma - 2\gamma_c P_0^2 = \frac{E}{P_0} = 0 \tag{3.83}$$

at zero electric field. According to Eq. (3.62), $\Delta^2(r,T) = r + \Sigma(r,T)$, so that the spectral gap in the ferroelectric phase is

$$\Delta_f^2(r,T) = 2\gamma_c P_0^2(r,T) > 0. \tag{3.84}$$

In Fig. 3.9(a) we plot the calculated temperature-dependent spectral gap $\Delta(r,T)$ for three different values of r as indicated in its schematic inset. As expected, for the quantum critical (QC) regime [2] the spectral gap closes exactly at $T = 0$ leading to a linear dispersion relation, $\omega = q$ at the QCP. We note that in the quantum paraelectric (QPE), Δ [or χ^{-1}] is constant. In the quantum ferroelectric (QFE) again Δ is constant; though there exists a classical paraelectric-ferroelectric transition at $T = T_c$ where $\chi^{-1} \sim (T - T_c)$. The static dielectric susceptibility in the vicinity of the QCP (low T) is presented in the same three r regimes in Fig. 3.9(b) where we see that in the QPE regime $\chi(T \to 0)$ saturates, at the QCP $\chi(T) \sim T^{-2}$ and diverges as $T \to 0$. In the QFE, the susceptibility also saturates at low temperatures, though the Curie law is recovered in the vicinity
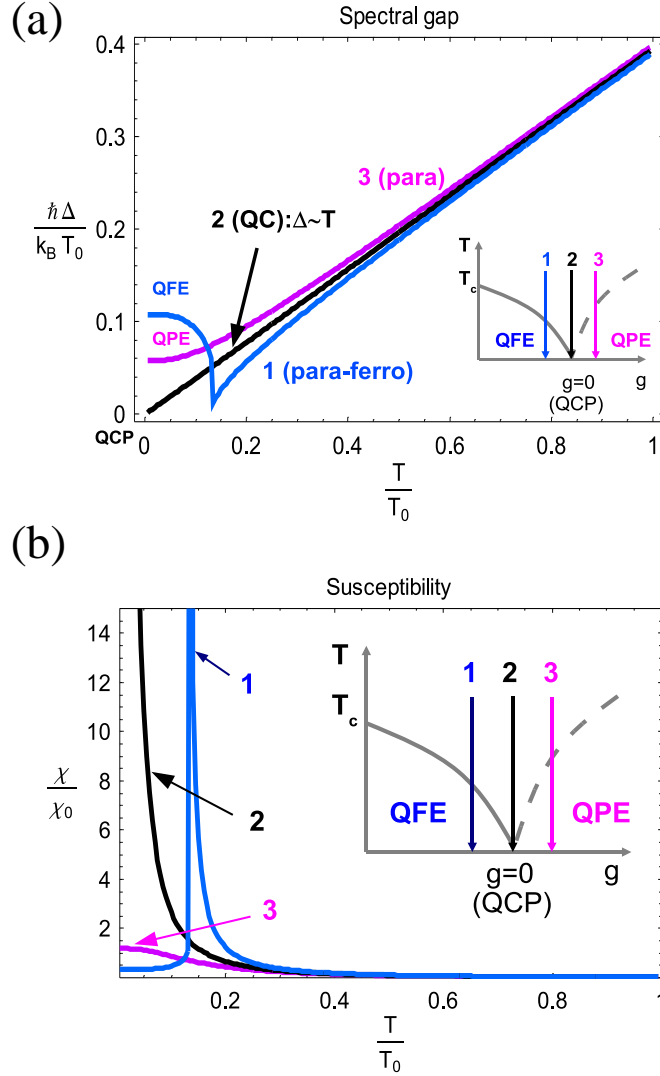
Figure 3.9: Temperature dependence of the a) spectral gap and b) the dielectric susceptibility for three temperature scans defined in the schematic inset; here $g = r - r_c$.

of the classical transition at $T = T_c$.

Fig. 3.10 shows the phase diagram that results from the self-consistent Hartree theory. This figure serves to emphasize how the strictly zero-temperature QCP gives rise to a quadratic power-law dependence of the inverse susceptibility on temperature over a substantial region of the $T - g$ phase diagram.

The crossover temperature, T_0, between Curie ($\chi^{-1} \sim T$) and quantum critical ($\chi^{-1} \sim T^2$)

Quantum Phase Diagram

as determined by $\dfrac{dln\chi^{-1}}{dln\left[(T-T_c)/T_0\right]}$
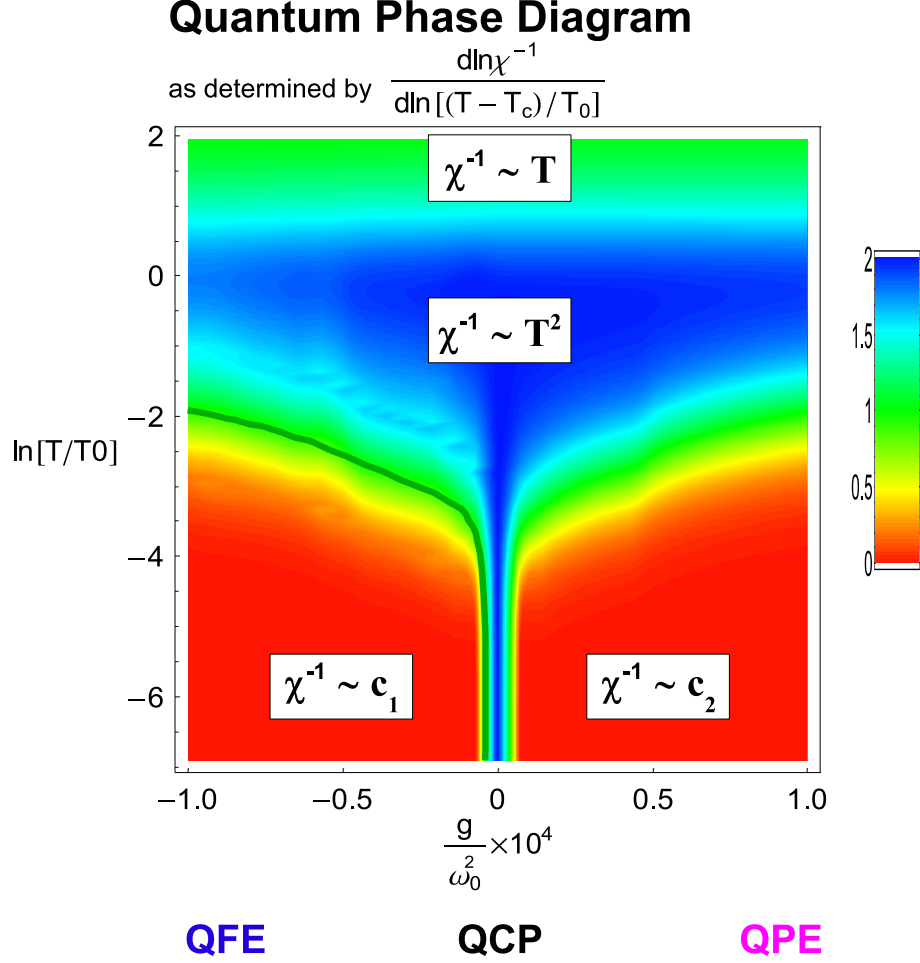
Figure 3.10: T-g phase diagram as determined by a self-consistent analysis of the dielectric susceptibilty. The power law exponents are depicted in different colors via the function $\frac{dln\chi^{-1}}{dln(T-T_c)/T_0}$. This expression selects the exponent 2 (blue region) for $\chi^{-1} \sim T^2$ [$T_c \equiv 0$ for QCP], exponent 1 (green region) for classical Curie behavior $\chi^{-1} \sim (T - T_c)$ and exponent 0 (red region) for a constant susceptibility.

behavior in the susceptibility is defined by the expression

$$T_0 \approx \frac{\hbar\omega_0}{2\pi k_B}, \tag{3.85}$$

where $\omega_0 = \frac{c_s}{a}$ is the characteristic soft-mode frequency, c_s is the soft-mode velocity, and a is the lattice spacing. Here we have assumed a simple band structure $\omega(q) = \omega_0 \sin qa$ such that $c_s = \left.\frac{d\omega}{dq}\right|_{q=0} = (\omega_0 a) \cos qa\big|_{q=0}$ so so that $\omega_0 = \frac{c_s}{a}$ as stated above. The factor of 2π in the denominator of Eq. (3.85) results from the observation that the separation of the poles of the Bose and

Fermi functions in the complex frequency plane is $\Delta\nu_n = 2\pi k_B T$, which sets the natural conversion factor between temperature and frequency to be $2\pi k_B$. T_0 also corresponds to the temperature when the correlation length is comparable to the lattice constant ($\xi \sim a$); here the correlation length $\xi \equiv \frac{c_s}{\Omega_0} \sim g^{-1/2}$ [see Eq. (3.52)]. Neutron-scattering measurements[170] of the dispersion relation indicate that the soft-mode velocity in STO is $c_s \approx 10^4 m/s$ and the lattice constant has been measured [15] to be $a_{STO} = 3.9 \times 10^{-10}m$; therefore $T_0 \approx 30K$. We note that with O^{18} substitution, the ambient pressure Curie temperature[30] is $T_c \sim 25K$. Using the values of c_s and a_{STO} from above, we get $\omega_0 \approx 2.6 \times 10^{13} Hz$ in SrTiO$_3$. The typical frequency $\Omega_0 = g^{1/2}$ [spectral gap at zero temperature] at which one observes the change in behavior in the dielectric susceptibility [exponent 2, blue region] is thus from Fig. 3.10, $\Omega_0 \approx 10^{-2}\,\omega_0 = 2.6 \times 10^{11} Hz$. Indeed, Raman scattering on ferroelectric SrTi^{18}O$_3$ [$T_c = 25K$] shows that the zero temperature Raman shift [171] is about $10\,cm^{-1}$ which translates into $\Omega_0 \approx 3 \times 10^{11} Hz$, in good agreement with our calculation.

3.5 Coupling to Long-Wavelength Acoustic Modes

3.5.1 Overview

In a conventional solid, broken translational symmetry leads to three acoustic Goldstone modes. At a ferroelectric QCP, these three modes are supplemented by one or more optical zero modes. This coexistence of acoustic and optic zero modes is a unique property of the ferroelectric QCP, and in this section we examine how their interaction influences observable properties.

The gap of the optical modes in a ferroelectric is sensitive to the dimensions of the unit cell and couples linearly to the strain field. This leads to an inevitable coupling between the critical optical mode and the long-wavelength acoustic phonons that must be considered. To address this issue, we consider the effect of a coupling η between the soft polarization and the strain field created by a single long-wavelength acoustic phonon mode. Softening of the polar transverse optic (TO) mode near the QCP enhances the effect of this coupling. Using dimensional analysis we find that the coupling between the TO and LA mode is marginally relevant in the physically important dimension

$d = 3$, and thus can not be ignored. The main result of the analysis is that the acoustic phonons act to soften and reduce the quartic interaction between the optic phonons. Beyond a certain threshold $\eta > \eta_c$, this interaction becomes attractive, leading to the development of a reentrant paraelectric phase at finite temperatures. We note that such a coupling to acoustic phonons has been considered previously,[139] and here we are rederiving and extending prior results in a contemporary framework.

3.5.2 Lagrangian and Dimensional Analysis

We introduce the coupling of the polarization ($P(\vec{x}, \tau)$) and the acoustic phonon ($\phi(\vec{x}, \tau)$) fields as a coupling of the polarization to strain $-\eta \nabla \phi P^2$; we then write the Lagrangian [139] as

$$\mathcal{L}_E[P, \phi] = \mathcal{L}_E[P] + \frac{1}{2} \left[(\partial_\tau \phi)^2 + \tilde{c}^2 (\nabla \phi)^2 \right] - \eta \nabla \phi P^2, \tag{3.86}$$

where $\mathcal{L}_E[P]$ is our previous Lagrangian without acoustic coupling given in Eq. (3.57). Here the constant η is the coupling strength to the acoustic phonon; the latter's dynamics are introduced in the bracketed terms of Eq. (3.86). Since we are using units in which the velocity of the soft optical phonon is one, $\tilde{c} = \frac{c_a}{c_s}$ is the ratio of the acoustic to the soft optical phonon velocities. We will discuss the restoration of dimensional constants in Eq. (3.86) when we make comparison to experiment in Sec. 3.5.6.

We begin with a dimensional analysis of the couplings to assess their relative importance in the physically important dimension $d = 3$. In order to do so, we introduce the RG flow by rescaling length, time, momentum, and frequency

$$x' = \frac{x}{\Lambda}, \quad \tau' = \frac{\tau}{\Lambda}, \quad q' = q\Lambda, \quad \nu' = \nu\Lambda, \tag{3.87}$$

with constant $\Lambda > 1$ representing flow away from the infrared (IR) limit of the QCP, that is flow from small to large momentum and frequency. In terms of the rescaled variables x' and τ', the

action Eq. (3.38) with Lagrangian Eq. (3.86) in $d+1$ dimensions becomes

$$
\begin{aligned}
S[P,\phi] &= \int_0^\beta d\tau \int d^d x \mathcal{L}_E[P,\phi] \\
&= \int_0^{\beta/\Lambda} d\tau' \int d^d x' \Lambda^{d+1} \Big\{ \frac{1}{2}\Lambda^{-2}\Big[(\partial_{\tau'}P)^2 + (\nabla'P)^2 + (\partial_{\tau'}\phi)^2 + (\nabla'\tilde{c}\phi)^2 \Big] \\
&\quad + \frac{1}{2}\Omega_0^2 P^2 + \frac{1}{4}\gamma_c P^4 - \eta\Lambda^{-1}\nabla'\phi P^2 \Big\}.
\end{aligned}
\tag{3.88}
$$

We emphasize that we write $\Omega_0^2 = r - r_c$ as the coefficient of the P^2 term in the Lagrangian $L_E[P]$ [Eq. (3.57)], entering Eq. (3.86) in Eq. (3.88), since our RG flow starts from the QCP ($r = r_c$). Rescaling P, ϕ, Ω_0^2, γ_c and η, so that the action Eq. (3.88) assumes its initial form, we write

$$
P' = P\Lambda^{\frac{d-1}{2}}, \quad \phi' = \phi\Lambda^{\frac{d-1}{2}}, \quad (\Omega_0^2)' = \Omega_0^2\Lambda^2, \quad \gamma_c' = \gamma_c\Lambda^{3-d}, \quad \eta' = \eta\Lambda^{2-\frac{d+1}{2}}, \tag{3.89}
$$

which leads to

$$
S[P,\phi] = \int_0^{\beta/\Lambda} d\tau' \int d^d x' \mathcal{L}_E[P',\phi'].
\tag{3.90}
$$

Now the fields, the mass term, and the coupling constants flow to new values leaving the action unperturbed. We remark that the upper cuttoff in the imaginary time dimension is replaced by infinity as the temperature $T \sim \frac{1}{\beta}$ approaches zero.

Analyzing the RG expressions in Eq. (3.89), we find that the Ω_0^2 term grows as we flow away from the QCP IR limit; therefore it is a relevant perturbation parameter independent of dimension d. This is consistent with the fact that $\Omega_0^2 = r - r_c = g$ *tunes* the system away from the QCP. Similarly we find that couplings γ_c and η grow (relevant) in dimension $d < 3$, decrease (irrelevant) in dimension $d > 3$, and do not change (marginally relevant) in $d = 3$. We see that in this case ($d = 3$) the coupling to acoustic phonons (η') is equally important as the mode-mode coupling (γ_c') and thus has to be included to the Gaussian model.

Let us now briefly summarize what we know about γ_c before we proceed to the discussion of the acoustic coupling η. In Sec. 3.4.2 we found that the spectral gap Δ is independent of γ_c for dimensions $1 < d < 3$ in the zero-temperature limit [see Fig. 3.8]. This is in agreement with
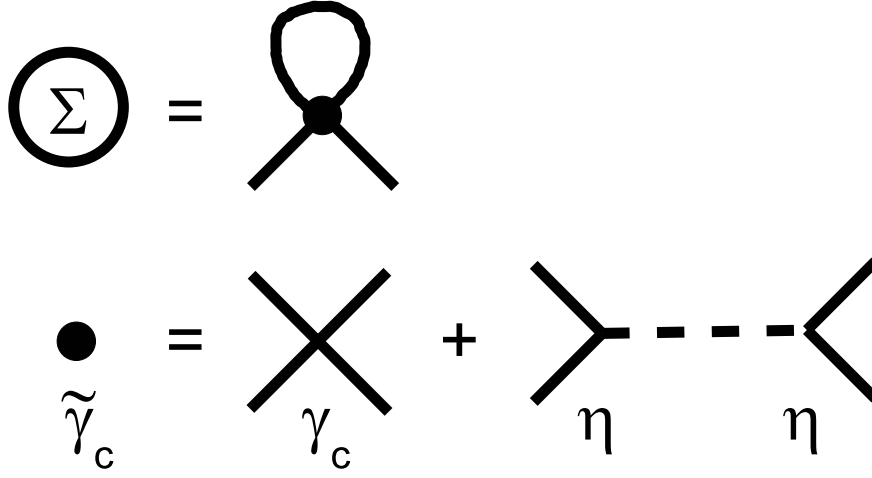
Figure 3.11: Diagrammatic representation of the self-energy that includes coupling to both optical and acoustic phonons. Here $\tilde{\gamma}_c$ is the renormalized coupling, including the exchange of an acoustic phonon.

the above results, where γ_c is a relevant perturbative parameter; more precise analysis [125] shows γ_c flowing to the nontrivial Wilson-Fisher fixed point γ_c^*. Here all the system properties become functions of $\gamma_c^* + \delta\gamma_c \approx \gamma_c^*$, and so are γ_c independent. On the other hand, in dimensions $d > 3$ and $d = 3$, γ_c flows to zero (with logarithmic corrections in the marginal case). In these cases the system properties are functions of $\delta\gamma_c$ and thus are γ_c dependent; we have already seen an example of this behavior in the specific case of the $d = 3$ spectral gap.

3.5.3 Gap Equation

We are now ready to explore how the system's low-temperature behavior changes in the presence of acoustic phonons in dimension $d = 3$. Let us look first at the LA phonon field ϕ. Following the procedure of Sec. 3.4.1, we find the acoustic Green's function and dispersion relation from Eq. (3.86) to be

$$D(q) \equiv D(\vec{q}, i\nu_n) = [(i\nu_n)^2 - \tilde{c}^2 q^2]^{-1}, \tag{3.91}$$

$$\omega_a(q) = \tilde{c}q. \tag{3.92}$$

We emphasize the P^2 dependency of the new interaction term, $-\eta\nabla\phi P^2$, in the Lagrangian

Eq. (3.86). Therefore it contributes to the polarization self-energy as an additional term inside the brackets of Eq. (3.58). This new contribution arises due to nonzero second-order perturbation and is schematically shown in Fig. 3.11, where the solid line represents the soft polarization TO Green's function Eq. (3.60) and the dashed line represents the LA Green's function Eq. (3.91). We note that the interaction represented by a *dot* in the self-energy consists of a contribution each from the coupling γ_c and η. Thus we can write the polarization self-energy Σ as a sum of these two terms

$$
\begin{aligned}
\Sigma(r,T) &= \Sigma_{\gamma_c}(r,T) + \Sigma_\eta(r,T) \\
&= (-3\gamma_c)T\sum_n \int \frac{d^3q}{(2\pi)^3} G(q,i\nu_n) \\
&+ 4\eta^2 T\sum_n \int \frac{d^3q}{(2\pi)^3} q^2 G(q,i\nu_n)D(q,i\nu_n),
\end{aligned}
\tag{3.93}
$$

where Σ_{γ_c} is the Hartree self-energy Eq. (3.65) previously calculated in Sec. 3.4.1. We remark that the q^2 term in the integral for Σ_η arises due to form of the interaction ($\nabla\phi$). Converting the Matsubara summation to a contour integral, deformed around the poles $z_p = \pm\omega_p(q)$ and $z_a = \pm\omega_a(q)$ in the dispersion relations of the polarization Eq. (3.61) and acoustic phonon Eq. (3.92) modes, respectively, we can rewrite Σ_η in the form [139]

$$
\Sigma_\eta(r,T) = -4\eta^2 \int \frac{d^3q}{(2\pi)^3} q^2 \left\{ \frac{[n_B(\omega_p(q)) + \frac{1}{2}]}{\omega_p[\omega_a^2 - \omega_p^2]} + \frac{[n_B(\omega_a(q)) + \frac{1}{2}]}{\omega_a[\omega_p^2 - \omega_a^2]} \right\}.
\tag{3.94}
$$

At the quantum critical point, where $r = r_c$ and $T = 0$, the dispersion $\omega_p(q) = q$ and $n_B(\omega_p) = n_B(\omega_a) = 0$ so that

$$
\Sigma_\eta(r_c,0) = -4\eta^2 \int \frac{d^3q}{(2\pi)^3} \frac{1}{2\tilde{c}(\tilde{c}+1)q}.
\tag{3.95}
$$

Using Eq. (3.63), we write the gap function [as in Sec. 3.4.1] as

$$
\begin{aligned}
\Delta^2 &= \Omega_0^2 + \Delta_{\gamma_c}^2 + \Delta_\eta^2, \\
\Delta_{\gamma_c}^2 &= 3\gamma_c \int \frac{d^3q}{(2\pi)^3} \left(\frac{[n_B(\omega_p(q)) + \frac{1}{2}]}{\omega_p} - \frac{1}{2q} \right),
\end{aligned}
$$
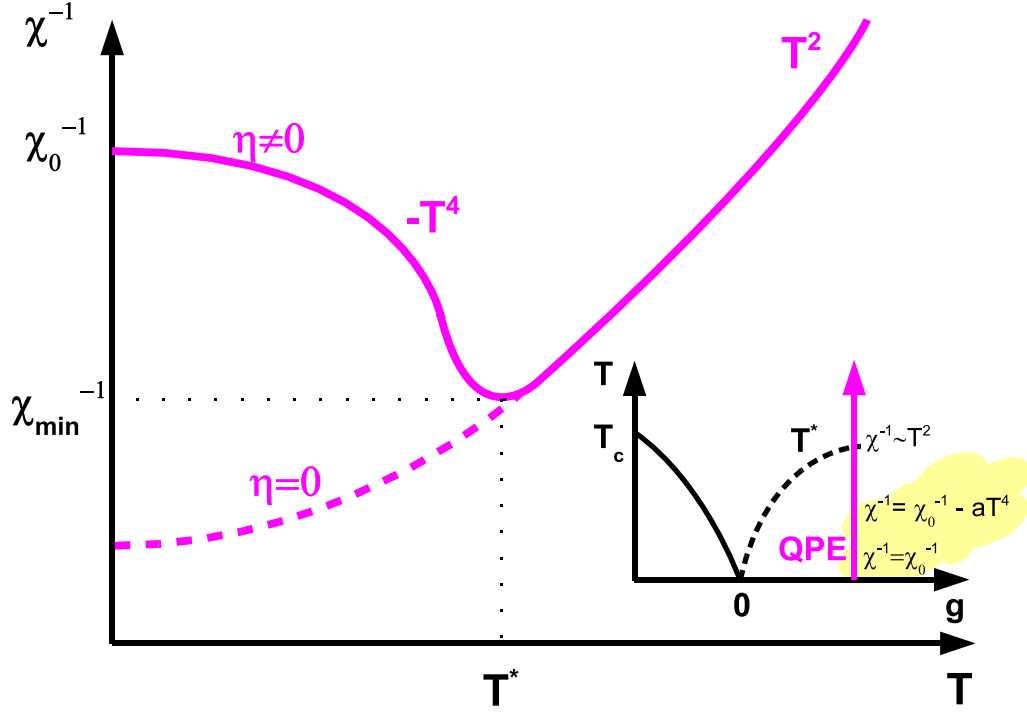
Figure 3.12: Schematic temperature dependence of the static dielectric susceptibility where coupling to a long-wavelength acoustic phonon is included in the calculation; inset indicates phase trajectory and region of corrections due to acoustic coupling deep in the QPE phase (yellow).

$$\Delta_\eta^2 \;=\; -4\eta^2 \int \frac{d^3q}{(2\pi)^3}\, q^2 \left(\frac{\left[n_B(\omega_p(q)) + \frac{1}{2}\right]}{\omega_p[\omega_a^2 - \omega_p^2]} + \frac{\left[n_B(\omega_a(q)) + \frac{1}{2}\right]}{\omega_a[\omega_p^2 - \omega_a^2]} - \frac{1}{2\tilde{c}[\tilde{c}+1]q^3} \right),$$

$$(3.96)$$

where $\Delta_{\gamma_c}^2$ has been already defined in Eq. (3.68).

We emphasize that the γ_c and η terms in Eq. (3.96) have opposite signs in their contribution to the spectral gap Δ. The negative coefficient of η^2 reflects the fact that it emerges from second-order perturbation theory; physically it is due to thermally enhanced virtual excitations caused by coupling between polarization TO and LA phonon modes.

3.5.4   Deep in the Quantum Paraelectric Phase

Let us first explore the effect of the acoustic coupling η deep in the QPE region of the phase diagram [see inset of Fig. 3.12]. Here $g >> 0$ and $\Delta >> T \approx 0$. In this regime, we write

$$\chi^{-1} = \Delta^2 = \Omega_0^2 + D(\Delta) - A(\eta)\frac{T^4}{\Delta^2}, \tag{3.97}$$

with

$$A(\eta) = \frac{4\eta^2}{\tilde{c}} \int \frac{d^3u}{(2\pi)^3} u\, n_B(\tilde{c}u), \tag{3.98}$$

where derivations of $A(\eta)$ and $D(\Delta)$ are presented in Sec. 3.7; for our purposes, the key point is to note that $\lim_{\Delta\to 0} D(\Delta) = 0$. Setting $A(\eta) \sim \eta^2 = 0$, we recover a constant expression for χ as a function of temperature in the QPE phase consistent with our previous derivations from Sec. 3.4. For $\eta \neq 0$, the dielectric susceptibility acquires different low-temperature behavior. The quartic temperature term in Eq. (3.97), $-A(\eta)\frac{T^4}{\Delta^2}$, drives the inverse susceptibility at low temperatures; such a "bump" in the susceptibility [or "well" in the inverse susceptibility, see Fig. 3.12] due to acoustic phonon coupling has been considered previously [139]. It is then natural to inquire whether a finite η could eventually drive the inverse susceptibility to zero (or negative) values. Here we show that this is not the case. We start by looking for a solution of Eq. (3.97) with $\chi^{-1} = \Delta^2 = 0$, and show that such a solution does not exist. Indeed at $\eta^2 = 0$, χ^{-1} in the QPE phase is nonzero as we saw in Sec. 3.4. At $\eta^2 \neq 0$, growth of last term in Eq. (3.97) exceeds all bounds and cannot equate a constant term Ω_0^2 [notice that $D(\Delta)|_{\Delta=0} = 0$]. The inverse susceptibility therefore remains positive deep in the QPE phase with $\chi^{-1}_{min} \neq 0$.

We note that when the temperature increases so that $\Delta \sim T$ and we are no longer in the QPE phase [red in Fig. 3.10], we enter the "tornado" region of the QCP influence [blue in Fig. 3.10] where $\chi^{-1} \sim \Delta^2 \sim T^2$, as was shown in Sec. 3.4. At this point the quadratic temperature dependence dominates and coupling to the acoustic phonons becomes negligible; as a result a turn-over in the inverse susceptibility from $-T^4$ to $+T^2$ dependence occurs [see Fig. 3.12].

3.5.5 Quantum Critical Temperature-Dependent Dielectric Susceptibility

We already know that there exists a classical phase transition at T_c for $g < 0$ and $\eta = 0$; for $\eta \neq 0$ could this line of transitions enter the $g > 0$ part of the phase diagram and result in a reentrant quantum ferroelectric phase near the $g = 0$ QCP? In order to explore this possibility, we study the temperature-dependent susceptibility near the QCP [at $g = 0$] and find that unstable behavior is possible. Next we follow the line of transitions, where $\chi^{-1} = \Delta^2 = 0$ and show that its behavior is changed for $\eta > \eta_c$.

We begin with $\chi(T)$ in the vicinity in the quantum critical regime where $g = 0$ [trajectory 2 in Fig. 3.9]; here $\Omega_0^2 = g = 0$ and $q \sim \omega \sim T \gtrsim 0$ at low temperatures. Taking $\eta = 0$, the spectral gap Eq. (3.96) becomes

$$\Delta_{\gamma_c}^2 = \frac{3\gamma_c}{2\pi^2} \int dq\, q\, n_B(q/T) \equiv \tilde{\alpha}\gamma_c T^2 = \frac{\gamma_c T^2}{4} \tag{3.99}$$

and we recover the quadratic temperature dependence, $\chi_{\gamma_c}^{-1} = \Delta_{\gamma_c}^2 \sim T^2$, that was derived in Sec. 3.4.2.

With $\eta \neq 0$, the η contribution to the gap becomes

$$\Delta_\eta^2 = -\frac{4\eta^2}{2\pi^2} \int dq\, \frac{q}{\tilde{c}^2 - 1} \left(n_B(q/T) - \frac{n_B(\tilde{c}q/T)}{\tilde{c}} \right) \equiv -\tilde{\beta}\eta^2 T^2. \tag{3.100}$$

For both cases $\tilde{c} \lessgtr 1$, the expression under the integral in Eq. (3.100) is positive [see Sec. 3.8 for specifics], which results in a negative coefficient for Δ_η^2. Adding both γ_c and η terms in the gap equation Eq. (3.96), we write the expression for the dielectric susceptibility

$$\chi^{-1} = \Delta^2 = (\tilde{\alpha}\gamma_c - \tilde{\beta}\eta^2)T^2 = (\frac{\gamma_c}{4} - \tilde{\beta}\eta^2)T^2, \tag{3.101}$$

where $\tilde{\alpha}$ and $\tilde{\beta}$ are explicitly calculated in Sec. 3.9. When the coefficient of T^2 is zero, namely,
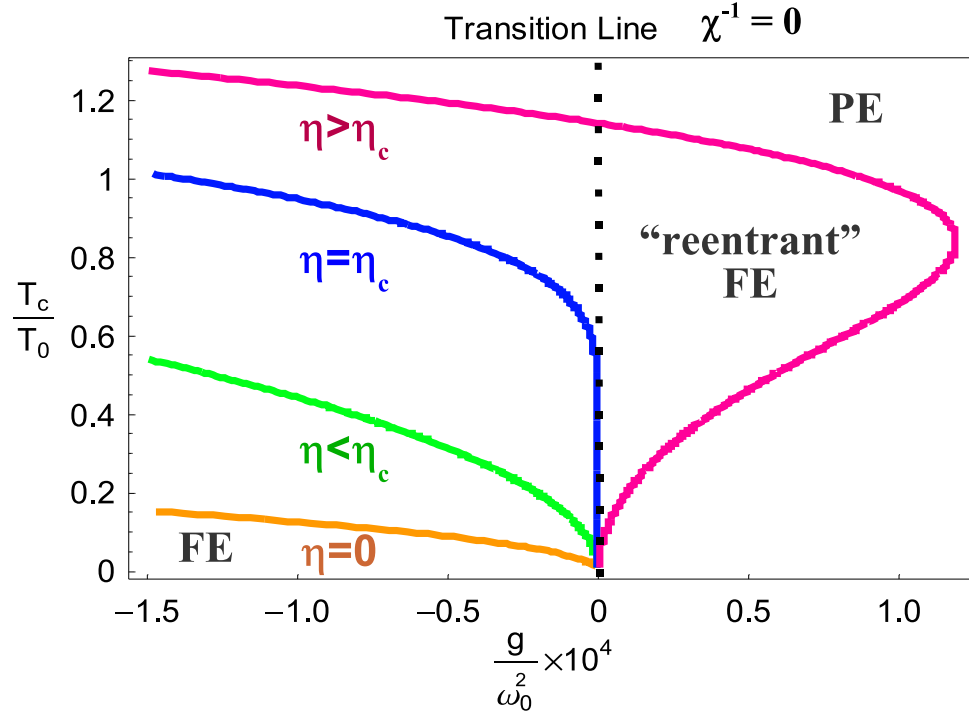
Figure 3.13: The transition line $T_c(g)$ for different values of η, the acoustic coupling constant; for $\eta > \eta_c$ a reentrant quantum ferroelectric (FE) phase emerges. The phase boundaries result from numerical solution of the gap equation $[\Delta(\eta \neq 0) = 0]$ discussed in the text; the parameters used here are as follows: $\gamma_c = 1, \tilde{c} = 0.9$, $\eta_c = 0.62$, and $\{\eta > \eta_c, \eta < \eta_c\} = \{0.63, 0.59\}$.

when

$$\eta = \eta_c = \sqrt{\frac{\gamma_c}{4\tilde{\beta}}} = \sqrt{\frac{3}{4}\left(\frac{\tilde{c}^3(\tilde{c}^2 - 1)}{\tilde{c}^3 - 1}\right)\gamma_c}, \tag{3.102}$$

the phase boundary line $[\chi^{-1} = 0]$ becomes vertical in the approach to the QCP; when $\eta > \eta_c$, it "meanders" to the right leading to reentrant behavior.

3.5.6 Details of the Phase Boundary ($\chi^{-1} = 0$)

We now follow the phase transition line, defined by $\chi^{-1} = 0$ $[\Delta = 0]$ out to finite temperatures. From Sec. 3.4 we know that there is a classical ferroelectric-paraelectric phase transtion at $g < 0$ at Curie temperature $T_c(g)$; it is depicted as a solid line in Fig. 3.9, where the dielectric susceptibility diverges, $\chi = \Delta^{-2} \to \infty$. Our results in Sec. 3.4 are for $\eta = 0$, and we study the effect of $\eta > \eta_c > 0$ on this transition line.

To do this, we look for a solution to the gap equation Eq. (3.96), when $\Delta(T_c, \eta) = 0$, which yields the transition line $T_c(g, \eta)$. When the spectral gap closes, the dispersion relations of the TO soft polarization and the LA acoustic modes both become linear $[\omega_p(q) = q$ and $\omega_a(q) = \tilde{c}q]$. Inserting these values into Eq. (3.96) and setting $\Delta = 0$, we obtain

$$
\begin{aligned}
-2\pi^2 \Omega_0^2 &= 3\gamma_c \int_0^{q_{max}} dq \, q \, n_B(q/T_c) - \frac{4\eta^2}{(\tilde{c}^2 - 1)} \int_0^{q_{max}} dq \, q \left\{ n_B(q/T_c) - \frac{n_B(\tilde{c}q/T_c)}{\tilde{c}} \right\} \\
&= T_c^2 \left\{ 3\gamma_c \int_0^{u_{max}} du \, u \, n_B(u) - \frac{4\eta^2}{(\tilde{c}^2 - 1)} \int_0^{u_{max}} du \, u \left\{ n_B(u) - \frac{n_B(\tilde{c}u)}{\tilde{c}} \right\} \right\}
\end{aligned}
$$
(3.103)

for the equation determining $T_c(g)$. At low temperatures, we note that we recover the scaling relation $\Omega_0^2 = g \sim T_c^2$ since both integrals become proportional to T_c^2 ($u_{max} = \frac{q_{max}}{T_c} \gg 1$). At high temperatures $n_B(u) \approx \frac{1}{u}$, so the right-hand side of Eq. (3.103) becomes proportional to T_c, and we recover the classical behavior $g \sim T_c$.

Fig. 3.13 shows the $T_c(g)$ transition line. For $\eta > \eta_c \approx 0.6$, the transition line "wanders" into the $g > 0$ region, leading to a reentrant quantum ferroelectric phase. Such reentrance suggests the possibility of nearby coexistence and a line of first-order transitions ending in a tricritical point, but the confirmation of this phase behavior requires a calculation beyond that presented here and will be the topic of future work.

In order to make direct comparison with experiment, we must now restore dimensions to our coupling constant and more generally to our Lagrangian Eq. (3.86). We start by explicitly restoring all physical coefficients to the Lagrangian as follows:

$$
\begin{aligned}
\beta F &= \int \frac{d^3 \tilde{x} d\tau}{\hbar} L \\
L &= \frac{\alpha}{2} \left[(\partial_\tau \tilde{P})^2 + c_s^2 (\nabla \tilde{P})^2 \right] + \frac{r_D}{2} \tilde{P}^2 + \frac{\gamma_D}{4} \tilde{P}^4 - \eta_D (\nabla . \tilde{\phi}) \tilde{P}^2 + \frac{\rho}{2} \left[(\partial_\tau \tilde{\phi})^2 + c_a^2 (\nabla \tilde{\phi})^2 \right],
\end{aligned}
$$
(3.104)

where c_s and c_a are the soft optical and acoustic phonon velocities, respectively, and where $\tilde{P}$ and

$\tilde{\phi}$ are the unrescaled physical polarization and phonon displacement fields. Then by writing

$$\frac{\tilde{x}}{c_s} = x, \qquad \frac{c_s^3 \alpha}{\hbar}\tilde{P}^2 = P^2, \qquad \frac{c_s^3 \rho}{\hbar}\tilde{\phi}^2 = \phi^2 \tag{3.105}$$

we obtain Eq. (3.86), the rescaled Lagrangian,

$$\begin{aligned}
\beta F &= \int d^3\tilde{x}d\tau \mathcal{L}_E(P, \phi), \\
\mathcal{L}_E(P, \phi) &= \frac{1}{2}\left[(\partial_\tau P)^2 + (\nabla P)^2\right] + \frac{r}{2}P^2 + \frac{\gamma}{4}P^4 - \eta(\nabla\phi)P^2 + \frac{1}{2}\left[(\partial_\tau \phi)^2 + \tilde{c}^2(\nabla\phi)^2\right],
\end{aligned} \tag{3.106}$$

where

$$\frac{c_s^2}{\hbar}L = \mathcal{L}_E, \quad r = \frac{r_D}{\alpha}, \qquad \gamma = \frac{\hbar}{c_s^3\alpha^2}\gamma_D, \qquad \eta = \frac{1}{\alpha c_s^{5/2}}\sqrt{\frac{\hbar}{\rho}}\,\eta_D, \qquad \tilde{c} = \frac{c_a}{c_s}. \tag{3.107}$$

In the dimensionless units used in this section, we found that

$$\eta_c = \sqrt{\frac{\tilde{\alpha}}{\tilde{\beta}}}\gamma_c = \sqrt{\frac{3}{4}\left(\frac{\tilde{c}^3(\tilde{c}+1)}{\tilde{c}^2 + \tilde{c} + 1}\right)\gamma_c}, \tag{3.108}$$

where $\tilde{\alpha} = \frac{1}{4}$, $\tilde{\beta} = \left(\frac{\tilde{c}^2+\tilde{c}+1}{3\tilde{c}^3(\tilde{c}+1)}\right)$. Using Eq. (3.107), we can now rewrite this critical coupling in dimensionful terms as follows

$$\begin{aligned}
\eta_{cD} &= \sqrt{\frac{\rho}{\hbar}}\alpha c_s^{5/2}\eta_c \\
&= \sqrt{\frac{\rho}{\hbar}}\alpha c_s^{5/2}\sqrt{\frac{3}{4}\left(\frac{\tilde{c}^3(\tilde{c}+1)}{\tilde{c}^2 + \tilde{c} + 1}\right)}\sqrt{\frac{\hbar}{c_s^3\alpha^2}\gamma_{cD}} \\
&= c_s\sqrt{\rho\gamma_{cD}}\sqrt{\frac{3}{4}\left(\frac{\tilde{c}^3(\tilde{c}+1)}{\tilde{c}^2 + \tilde{c} + 1}\right)}. \tag{3.109}
\end{aligned}$$

For SrTiO$_3$, the acoustic [172, 173] and the soft-mode [170] velocities have been measured to be $c_a \approx 8000m/s$ and $c_s \approx 10000m/s$, respectively, so that $\tilde{c} = 0.8$; the crystal mass density is $5.13g/cm^3 = 5.13 \times 10^3 kg/m^3$. The value of γ_c has been measured [31, 32] using ferroelectric

Arrott plots of E/P vs P^2 to be $\epsilon_0 \gamma_{cD} = 0.2 \quad m^4/C^2$. Inputting all these numbers and $\eta_c = 0.6$ into our dimensionful expression for η_{cD}, we obtain

$$\eta_{cD}^{STO} = 5.74 \times 10^{10} Jm/C^2 \tag{3.110}$$

as the dimensionful critical coupling to be compared with experiment.

Next we estimate the experimental value of η in SrTiO$_3$ as [174] $\eta^{STO} \approx \frac{Q}{s}$ where Q and s are the typical magnitudes of the electrostrictive constants and the elastic compliances [92, 174], respectively; here we use the values [174] $Q = 0.05 \quad \frac{m^4}{C^2}$ and $s = 3 \times 10^{-12} \quad \frac{ms^2}{kg}$. Thereofore we obtain

$$\eta_{STO} = 1.7 \times 10^{10} Jm/C^2 \tag{3.111}$$

so that from our analysis we observe that $\eta_{STO} < \eta_{cD}^{STO}$ for the SrTiO$_3$ system. However, there are two points of uncertainty here that we should emphasize: (i) we use experimental values for SrTi^{16}O$_3$ as they are not yet available for SrTi^{18}O$_3$; (ii) we use values of Q and s at room temperature, and these quantities need to be determined at low temperatures. Despite the roughness of our estimate, it is reasonable to assume η is not changed dramatically by the issues raised in (i) and (ii). We encourage further experimental investigations of SrTi^{18}O$_3$ at low temperatures to clarify this situation.

3.5.7 Translational-Invariance as Protection against Damping Effects and Singular Interactions

Our analysis of the effects of acoustic coupling has been limited to a Hartree treatment of the leading self-energy. This approach neglects two physical effects: (i) damping, the process by which a soft-mode phonon can decay by the emission of an acoustic phonon and (ii) the possibility of singular interactions induced by the exchange of acoustic phonons.

Similar issues are of great importance in magnetic quantum phase transitions in metals, where

the coupling of the magnetization to the particle-hole continuum of electrons introduces damping [175–177]. For example, in the simplest Hertz-Moriya treatment of a ferromagnetic quantum critical point, damping by the electron gas gives rise to a quadratic Lagrangian of the form

$$S_M = \sum_{q,\nu} \left[q^2 + r + \frac{|\nu|}{q} \right] |M(q,\nu)|^2, \tag{3.112}$$

where the term linear in $|\nu|$ is a consequence of damping by the particle-hole continuum. This term plays a vital role in the quantum critical behavior; by comparing the dimensions of the q^2 term with the damping term, we see that $[\nu] \equiv q^3$, which means that the temporal dimension scales as $z = 3$ spatial dimensions under the renormalization group. This has the effect of pushing the upper critical dimension down from $4 - 1 = 3$ to $4 - z = 1$ dimensions. In addition to this effect, the coupling to the electron-hole continuum also introduces non-local interactions between the magnetization modes, casting doubt on the mapping to a ϕ^4 field theory.

Fortunately, translational invariance protects the ferroelectric against these difficulties. Translational invariance guarantees that the soft mode can not couple directly to the displacement of the lattice; instead it couples to the strain, the gradient of the displacement, according to the interaction $H_I = -\eta \nabla \phi P^2$. When we integrate out the acoustic phonons, the induced interaction between the soft-mode phonons takes the form

$$V(q,\nu) = -4\eta^2 \frac{q^2}{\nu^2 + \tilde{c}^2 q^2}, \tag{3.113}$$

where the numerator results from the coupling to the strain, rather than the displacement. The presence of the q^2 term in the numerator removes the "Coulomb-type" $1/q^2$ divergence at small q, protecting the soft-mode interactions from the development of a singular long range component.

A similar effect takes place with the damping. To see this, we need to examine the imaginary part of the self-energy appearing in the Gaussian contribution to the action, Eq. (3.58),

$$S_G = \sum_{q,\nu} \frac{1}{2} \left[\nu^2 + q^2 + r + \Sigma_\eta(q) \right] |P(\vec{q},\nu)|^2. \tag{3.114}$$

Damping results from the imaginary part of self-energy, $\Sigma''_n(q, \omega)$. To compute the damping, we generalize Σ_η given in Eq. (3.94) to finite frequency, obtaining

$$\Sigma_\eta(q, z) = 2\eta^2 \int \frac{d^3k}{(2\pi)^3} k^2 \left\{ \frac{[n_p + \frac{1}{2}]}{\omega_p[(z - \omega_p)^2 - \omega_a^2]} + \frac{[n_a + \frac{1}{2}]}{\omega_a[(z - \omega_a)^2 - \omega_p^2]} + (z \leftrightarrow -z) \right\},$$

(3.115)

where we have used the short-hand $\omega_a \equiv \omega_a(k)$, $\omega_p \equiv \omega_p(\vec{q} - \vec{k})$, $n_a = n_B[\omega_a(k)]$, and $n_p = n_B[\omega_p(\vec{q} - \vec{k})]$. The imaginary part of this expression at zero temperature, for positive ν, is then given by

$$Im[\Sigma_\eta(q, \nu - i\delta)] = \pi\eta^2 \int \frac{d^3k}{(2\pi)^3} \frac{k^2}{\omega_p \omega_a} \delta(\omega - \omega_a - \omega_p).$$

(3.116)

We can determine the small q, ω behavior of this damping rate by simple dimensional analysis. The dimension of the right-hand side is $[q^5]/[\omega^2] \sim q^2$, so the damping rate must have the form

$$Im\Sigma(q, \nu) \sim \eta^2 \nu^2 F\left(\frac{q}{|\nu|}, \frac{\Delta}{|\nu|}\right),$$

(3.117)

where a more careful analysis of the integral reveals that $F\left(\frac{q}{|\nu|}, \frac{\Delta}{|\nu|}\right)$ is not singular at either small momentum or frequency. The most important aspect of this result is that the scattering phase space grows quadratically with frequency and momentum, so that it does not dominate over the other terms in the action Eq. (3.114). The scaling dimension of frequency remains the same as that of momentum, and thus the upper-critical spatial dimension remains as $d = 3$.

3.6 Discussion

3.6.1 Logs, Dipolar Interactions, and the Barrett Formula

Before summarizing our results, let us briefly touch on a number of topics closely related to our work which we have not yet discussed; more specifically they include logarithmic corrections in the upper critical dimension, dipolar interactions and the use of the Barrett formula for quantum

paraelectrics. As we have already noted in Sec. 3.5.2, the polarization mode-mode interaction γ_c and coupling to the acoustic phonons η, are both marginally relevant in the dimension of physical interest $d = 3$. Thus logarithmic corrections to the scaling relations [Sec. 3.3] have to be included; we have already seen their appearance in the expression for α_3 in Eq. (3.81). The correction to scaling of the free energy near the classical ferro-paraelectric phase transition in four dimensions is [125]

$$f_{cl}(t, \gamma_c) = f_0(t, \gamma_c)[1 + 9\gamma_c \, ln(t_0/t)]^{1/3}, \tag{3.118}$$

where $t = |\frac{T - T_c}{T_c}|$ is the reduced temperature, $f_0(t, \gamma_c) = t^2 \Phi\left(\frac{E/E_0}{|t/t_0|^{3/2}}\right)$ is the scaling form of the free energy with a universal scaling function Φ, t_0 is the reduced Debye temperature for the soft mode Eq. (3.85) and γ_c is the polarization mode-mode coupling at QCP. Since $\chi = \frac{\partial^2 f}{\partial E^2}|_{E=0}$, we have

$$\chi = \chi_0[1 + 9\gamma_c \, ln(t_0/t)]^{1/3}, \tag{3.119}$$

where $\chi_0 \sim t^{-1}$. By applying the quantum-classical analogy [Sec. 3.3], we write at the upper critical dimension, $d_c^u = 3$ ($d + z = 4$; $z = 1$),

$$f_{qm}(g, \gamma_c) = f_0(g, \gamma_c)[1 + 9\gamma_c \, ln(g_0/g)]^{1/3}, \tag{3.120}$$

where $g_0 \equiv \omega_0^2$ is the Debye frequency for the soft mode squared, $f_0(g, \gamma_c)$ has the same form as before, and g is the tuning parameter. By setting $\chi = \frac{\partial^2 f}{\partial E^2}|_{E=0}$, the dielectric susceptibility becomes

$$\chi = \chi_0[1 + 9\gamma_c \, ln(g_0/g)]^{1/3}, \tag{3.121}$$

where $\chi_0 \sim g^{-1} \sim T^{-2}$. The temperature dependence of χ with logarithmic corrections is then found by making the subsitution $g \sim T^2$ in Eq. (3.121), and these results are identical to those found previously using diagrammatic techniques[138]. An analogous procedure can be used to find the logarithmic corrections to other thermodynamic quantitites.

We note that here we assume the upper critical [spatial] dimension $d_c^u = 3$; however if we

include uniaxial dipole-dipole interactions, we will have $d_c^u = 2$. Basically this is because when all dipoles point in the [same] z-direction, the TO polarization frequency Eq. (3.61) becomes [178]

$$\omega^2(q) = q^2 + \Delta^2 + \beta \frac{q_z^2}{q^2}, \tag{3.122}$$

where β is a constant, and we derive Eq. (3.122) in Sec. 3.10. We note that the last term of Eq. (3.122) is specific to the uniaxial [e.g., tetragonal] case and is not present for isotropic dipolar interactions. Applying simple scaling, we obtain

$$\tilde{q}_{x(y)} = \frac{q_{x(y)}}{b}, \quad \tilde{q}_z = \frac{q_z}{b^k}, \tag{3.123}$$

where the constants b, $b^k > 1$ represent flow to the infrared (IR) limit of the QCP. We show in Sec. 3.10 that in order for Eqs. (3.122) and (3.123) to be satisfied simultaneously, k must equal 2 so that q_z "counts" for effectively *two* dimensions ($d_{eff}^{space} = d + 1$), so that for a quantum uniaxial ferroelectric the total effective dimension is $d_{eff} = d_{eff}^{space} + z = (d+1) + z = d + 2$ with $d_c^u = 2$ since then we obtain $d_{eff} = 4$.

At this time, it is not known whether SrTi^{18}O$_3$ is cubic or tetragonal at low temperatures. In any case, we expect the samples under study to be structurally multidomain so that averaging over long length scales will make them effectively cubic; thus uniaxial dipolar interactions do not need to be considered. The observed T^2 behavior of χ in the vicinity of the QCP supports this contention [i.e., $d_{eff}^{space} = 3$]; for $d_{eff}^{space} = 4$, a different T dependence [$\chi^{-1} \sim T^3$] is expected[142] for a QPE so that a reexamination of the underlying model would be necessary to match experiment. Until details of the samples are known, this situation cannot be ascertained. We note that such T^2 dependence of the inverse susceptibility has also been observed[162] in mixed crystal ferroelectrics KTa$_{1-x}$Nb$_x$O$_3$ and Ka$_{1-y}$Na$_y$TaO$_3$ where uniaxial dipolar interactions are not important, and we encourage further low-temperature studies of these systems.

A consistent discrepancy between the observed low-temperature dielectric susceptibility and the Barrett formula[169] has been observed in the quantum paraelectric phase. [43, 162] Here we

emphasize that the discrepancy occurs when the system gets very close to the QCP; thus it provides a measure of the tuning distance to the QCP. Because the optical polarization mode softens as the system approaches the QCP, with the gap vanishing completely here, the momentum dependence in the dispersion relation Eq. (3.61) becomes important. It is exactly for this reason that the Barrett formula, that assumes a constant dispersion relation, $\omega = \tilde{\omega}_0$, breaks down close to the QCP.

The Barrett formula [169] works well deep in the QPE phase [Sec. 3.5.4], where the gap is much bigger than temperature. One such example is $KTaO_3$ (KTO), which remains paraelectric down to zero temperature, but in contrast to $SrTiO_3$ (STO) shows a much lower value of the zero temperature dielectric susceptibility [$\chi_{KTO} \approx 4000$, $\chi_{STO} \approx 24000$] [43, 49]. The closer the system is tuned to the QCP, the smaller is the spectral gap and the bigger the dielectric susceptibility. Therefore, STO sits much closer to the QCP than KTO, and indeed KTO shows a nice fit to the Barrett formula [49]. Notice that by plugging $\tilde{\omega}_0$ into Eq. (3.68), we get the Barrett expression,

$$
\begin{aligned}
\chi^{-1} = \Delta^2 &= \Omega_0^2 + \frac{3\gamma_c}{4\pi^2} \left(\frac{\coth(\tilde{\omega}_0/2T)}{\tilde{\omega}_0} \frac{q_{max}^3}{3} - \frac{q_{max}^2}{2} \right) \\
&= \frac{1}{M} \left(\frac{T_1}{2} \coth(T_1/2T) - T_0 \right),
\end{aligned}
\tag{3.124}
$$

where $T_1 \equiv \tilde{\omega}_0$, and M and T_0 are fitting constants.

3.6.2 Summary and Open Questions

Let us now summarize the main results of this chapter. Here our aim has been to characterize the finite-temperature properties of a material close to its quantum ferroelectric critical point; we have rederived and extended previous theoretical results using scaling methods and self-consistent Hartree theory. In the process we have made an analogy between temperature as a boundary effect in time and the Casimir effect, and have used this to shed light on both problems. Using simple finite-size scaling, we have presented straightforward derivations of finite-temperature observables for direct comparison with experiment, and our approach has yielded a scaling form $\chi(\omega) = \frac{1}{\omega}F(\frac{\omega}{T})$ which serves as an additional probe of T_0, the soft-mode Debye temperature-scale where we expect

crossover between Curie (T) and Quantum Critical (T^2) behavior in χ^{-1}. We emphasize that this scaling method is useful in this system where z is low [$z = 1$]; otherwise if z is higher, the system is usually well above its upper critical dimension where this approach is inappropriate. Next we have used self-consistent Hartree methods to determine the $T - g$ phase diagram and the crossover between classical and quantum behavior. In particular we see the influence of the quantum critical point on the susceptibility at finite temperatures, and we can put in materials parameters to determine the size of its basin of attraction. Finally we include coupling to an acoustic phonon and find that it affects the transition line; for such couplings greater than a threshhold strength there is a reentrant quantum ferroelectric phase.

Naturally these results suggest a number of open questions and here we list a few:

(i) The presence of a reentrant phase suggests the possibility of nearby phase coexistence, a tricritical point, and a line of first order transitions. This is a particularly appealing scenario given that recent experiments[179] suggest coexistence of QPE and QFE in SrTi^{18}O$_3$ and is a topic we plan to pursue shortly.

(ii) If indeed there is a tricritical point and a line of first-order phase transitions, could there also be a metaelectric critical point in the $g - E$ plane analogous to the metamagnetic situation[180, 181] in some metallic systems? There is indication that an analogous metaelectric critical point occurs in a multiferroic system,[182] so this is a question driven by recent experiment.

(iii) What happens when we add spins to a system near its quantum ferroelectric critical point? Would the resulting multiferroic have particularly distinctive properties?

(iv) Similarly, what type of behavior do we expect if we dope a quantum parelectric in the vicinity of a QCP? There is by now an extensive body evidence that electronically mediated superconductivity is driven by the vicinity to a magnetic quantum critical point, a phenomenon of "avoided criticality", whereby superconductivity in the vicinity of a naked magnetic quantum critical point[183, 184]. In such systems, the metallic transport properties develop strange metallic properties that have been termed "non-Fermi liquid behavior"[185, 186]. This raises the important question, as to what, if any, is the ferroelectric counterpart to this behavior? In particular, how does

the presence of a soft mode affect the semimetallic properties of a doped quantum critical ferroelectric, and does a doped ferroelectric quantum critical point also develop superconductivity via the mechanism of avoided criticality?

We believe that we have only begun to explore the rich physics associated with the quantum ferroelectric critical point, a simple setting for studying many issues associated with quantum criticality that emerge in much more complex materials. Furthermore the possibility of detailed interplay between theory and experiment is very encouraging.

3.7 Appendix A: $D(\Delta)$ and $A(\eta)$

We derive expressions for $D(\Delta)$ and $A(\eta)$ [Eq. (3.98)] using the gap equation Eq. (3.96) deep in the QPE region (D), where $g >> 0$ and $\Delta >> T \approx 0$. Collecting all "$\frac{1}{2}$"-terms under integrals of $\Delta_{\gamma_c}^2$ and Δ_η^2 in Eq. (3.96), we obtain the expression for $D(\Delta)$,

$$
\begin{aligned}
D(\Delta) &\equiv \frac{3}{2}\gamma_c \int \frac{d^3q}{(2\pi)^3} \left(\frac{1}{\omega_p} - \frac{1}{q} \right) \\
&\quad -2\eta^2 \int \frac{d^3q}{(2\pi)^3} q^2 \left(\frac{1}{\omega_a[\omega_p^2 - \omega_a^2]} - \frac{1}{q^3\tilde{c}[1-\tilde{c}^2]} \right) \\
&\quad -2\eta^2 \int \frac{d^3q}{(2\pi)^3} q^2 \left(\frac{1}{\omega_p[\omega_a^2 - \omega_p^2]} - \frac{1}{q^3[\tilde{c}^2 - 1]} \right) \\
&\equiv \frac{3\gamma_c}{4\pi^2} I_1 - \frac{\eta^2}{\tilde{c}\pi^2} I_2 - \frac{\eta^2}{\pi^2} I_3, \\
I_1 &= \int_0^{q_{max}} dq\, q^2 \left(\frac{1}{\sqrt{\Delta^2 + q^2}} - \frac{1}{q} \right), \\
I_2 &= \int_0^{q_{max}} dq\, q^3 \left(\frac{1}{\Delta^2 + q^2[1 - \tilde{c}^2]} - \frac{1}{q^2[1 - \tilde{c}^2]} \right), \\
I_3 &= \int_0^{q_{max}} dq\, q^4 \left(\frac{1}{\sqrt{\Delta^2 + q^2}[-\Delta^2 + q^2[\tilde{c}^2 - 1]]} - \frac{1}{q^3[\tilde{c}^2 - 1]} \right).
\end{aligned}
\tag{3.125}
$$

Notice that $\lim_{\Delta\to 0} D(\Delta) = 0$, since all three integrals I_1, I_2 and I_3 become zero at zero gap. We split the integrals I_i ($i = 1,2,3$) into two parts, $I_i = \int_0^{n\Delta} + \int_{n\Delta}^{q_{max}}$, where $n\Delta >> \Delta$. Since $q >> \Delta$ in the second integral part, we neglect its Δ dependence and get a zero contribution. Thus, only the first integral part contributes, and $D(\Delta)$ becomes a function of Δ only, with no temperature dependence.

Next we show that the second Bose-Einstein $n_B[\omega_a(q)]$ term under the integral of Δ_η^2 in Eq. (3.96) results in the form $A(\eta)$ in equation Eq. (3.98),

$$
\begin{aligned}
-4\eta^2 \int \frac{d^3q}{(2\pi)^3} q^2 \frac{n_B[\omega_a(q)]}{\omega_a[\omega_p^2 - \omega_a^2]} &= -4\eta^2 \int \frac{d^3q}{(2\pi)^3} q^2 \frac{n_B[\omega_a(q)]}{\tilde{c}q[\Delta^2 + q^2(1 - \tilde{c}^2)]} \\
&\approx -\frac{4\eta^2}{\tilde{c}} \frac{T^4}{\Delta^2} \int \frac{d^3u}{(2\pi)^3} u\, n_B(\tilde{c}u) \equiv -A(\eta)\frac{T^4}{\Delta^2}, \quad (3.126)
\end{aligned}
$$

where $u = q/T$. Notice that we approximate $\Delta^2 >> q^2(1 - \tilde{c}^2)$ in the second line of Eq. (3.126). For low momenta, this is indeed the case. For large momenta, $q >> \Delta >> T \approx 0$, we neglect Δ in Eq. (3.126) and the integral becomes

$$
-\frac{4\eta^2}{2\pi^2 \tilde{c}(1 - \tilde{c}^2)} \int dq\, q n_B(\tilde{c}q). \tag{3.127}
$$

In the limit $q >> T$, $n_B(\tilde{c}q) \approx e^{-\tilde{c}q/T}$ and Eq. (3.127) becomes exponentially small $[\sim T^2 e^{-\tilde{c}q/T}]$ and can be neglected. Similarly, we neglect the rest of the terms in the gap function Eq. (3.96) with Bose-Einstein thermal distribution $n_B[\omega_p(q)]$. Deep in the QPE phase $\Delta >> T$, so that $n_B[\omega_p(q)] \approx e^{-\Delta/T}$ at low momenta, or $n_B[\omega_p(q)] \approx e^{-q_{large}/T}$ at large momenta. In both cases $\Delta, q_{large} >> T$, the integrals containing $n_B[\omega_p(q)]$ become exponentially small and are negligible.

3.8   Appendix B: Integral Eq. (3.100) is Positive for $\tilde{c} \lessgtr 1$

We also show that the expression under the integral in Eq. (3.100) is positive for the two cases, $\tilde{c} \lessgtr 1$. First, assuming that $\tilde{c} < 1$, $\tilde{c}q < q$ [positive q's] and $n_B(\tilde{c}q/T) > n_B(q/T)$ we write

$$
\begin{aligned}
\left\{ n_B(q/T) - \frac{n_B(\tilde{c}q/T)}{\tilde{c}} \right\} \frac{1}{\tilde{c}^2 - 1} &> \left(1 - \frac{1}{\tilde{c}}\right) n_B(\tilde{c}q/T)\frac{1}{\tilde{c}^2 - 1} \\
&= \frac{1}{\tilde{c}(\tilde{c} + 1)} n_B(\tilde{c}q/T) \geq 0, \tag{3.128}
\end{aligned}
$$

which we note is positive. Similarly, for $\tilde{c} > 1$, $\tilde{c}q > q$, and $n_B(\tilde{c}q/T) < n_B(q/T)$, we write

$$
\left\{ n_B(q/T) - \frac{n_B(\tilde{c}q/T)}{\tilde{c}} \right\} \frac{1}{\tilde{c}^2 - 1} > \left(1 - \frac{1}{\tilde{c}}\right) n_B(q/T)\frac{1}{\tilde{c}^2 - 1}
$$

$$= \frac{1}{\tilde{c}(\tilde{c}+1)} n_B(q/T) \geq 0 \qquad (3.129)$$

which is also positive. Therefore the integral in Eq. (3.100) is positive in both cases.

3.9 Appendix C: $\tilde{\alpha}$ and $\tilde{\beta}$ are Constants

To evaluate the quantities $\tilde{\alpha}$ and $\tilde{\beta}$ in Eqs. (3.99) and (3.100), we make a change of variables to $u = q/T$, and $u = \tilde{c}q/T$, respectively. The expressions for these two constants then become

$$
\begin{aligned}
\tilde{\alpha} &= \frac{3}{2\pi^2} \int_0^{q_{max}/T} du\, u\, n_B(u) = \frac{1}{4}, \\
\tilde{\beta} &= \frac{2}{\pi^2(\tilde{c}^2-1)} \left[\int_0^{q_{max}/T} -\frac{1}{\tilde{c}^3} \int_0^{\tilde{c}q_{max}/T} \right] du\, u\, n_B(u) = \frac{1}{3(\tilde{c}^2-1)} \left(1 - \frac{1}{\tilde{c}^3}\right), (3.130)
\end{aligned}
$$

where we have taken the limits of integration to infinity and used the result $\int_0^\infty du\, u n_B(u) = \frac{\pi^2}{6}$.

3.10 Appendix D: Dipole-Dipole Interactions in Uniaxial Ferroelectrics

The interaction energy between two dipoles $\vec{p}_i$ and $\vec{p}_j$ siting on two sites $\vec{r}_i$ and $\vec{r}_j$, respectively, is

$$W_{ij}(\vec{r}) = \frac{\vec{p}_i \cdot \vec{p}_j - 3(\vec{n} \cdot \vec{p}_i)(\vec{n} \cdot \vec{p}_j)}{4\pi\epsilon_0 |\vec{r}|^3}, \qquad (3.131)$$

where $\vec{n}$ is a unit vector in the direction of the vector $\vec{r} \equiv \vec{r}_j - \vec{r}_i$. From Eq. (3.131), we find the total dipole-dipole interaction potential to be

$$W(\vec{r}) = \frac{1}{4\pi\epsilon_0} \sum_{i,j,a,b} p_i^a p_j^b \left(\frac{\delta_{ab}}{r^3} - \frac{3r^a r^b}{r^5} \right), \qquad (3.132)$$

where $r \equiv |\vec{r}|$, and a, b label vector coordinates. After we perform a Fourier transform, the interaction potential becomes

$$W(\vec{q}) = \frac{1}{\epsilon_0} \sum_{a,b} p_{\vec{q}}^a p_{-\vec{q}}^b \frac{q_a q_b}{q^2}, \qquad (3.133)$$

where $q \equiv |\vec{q}|$ refers to the momentum dependence of $W(\vec{q})$. Assuming that all dipoles point in the same (z) direction in the uniaxial case, we find that the dipole potential

$$W(\vec{q}) \sim \frac{q_z^2}{q^2}. \tag{3.134}$$

$W(\vec{q})$ contributes to Lagrangian Eq. (3.86), $L_E[P, \Phi] \rightarrow L_E[P, \Phi] + W$, so that the TO polarization frequency Eq. (3.61) then reads [178]

$$\omega^2(q) = c_s^2 q^2 + \Delta^2 + \beta \frac{q_z^2}{q^2}, \tag{3.135}$$

where we introduce constant of proportionality β.

We show that Eqs. (3.122) and (3.123) lead to the conditon $k = 2$. Let us assume that $k > 1$. Then

$$
\begin{aligned}
\tilde{q}^2 &= \tilde{q_x}^2 + \tilde{q_y}^2 + \tilde{q_z}^2 = \frac{q_x^2 + q_y^2}{b^2} + \frac{q_z^2}{(b^2)^k} \approx \frac{q^2}{b^2}, \\
\frac{\tilde{q}_z^2}{\tilde{q}^2} &\approx b^{2-2k} \frac{q_z^2}{q^2}.
\end{aligned}
\tag{3.136}
$$

Since we also rescale frequency $\omega(q)$ [Eq. (3.122)] by a constant, expressions $\tilde{q}^2$ and $\frac{\tilde{q}_z^2}{\tilde{q}^2}$ are to be proportional. This leads then to the condition

$$k = 2. \tag{3.137}$$

Chapter 4

Multiferroic BiFeO$_3$-BiMnO$_3$ Nanocheckerboard From First Principles

4.1 Introduction

Artificially structured oxides present intriguing opportunities for material design. With dramatic advances in epitaxial growth techniques allowing atomic-scale control, experimental and theoretical attention has focused on strained-layer superlattices [16–18, 20–26]. Properties significantly different from those in the bulk have been observed, leading to the possibility of designing new materials at the nanoscale with enhanced functionalities [187–189]. Recently, progress has been reported in the synthesis of artificially structured oxides with lateral "nanocheckerboard" (or nanopillar) patterning. In particular, the length scale of this checkerboard ordering can be controlled by synthetic processes and stoichiometry, offering promise for applications such as ultrahigh-density magnetic recording media [190–195].

One functionality of particular current interest is multiferroicity: the combination of ferromagnetism and ferroelectricity, with coupling between the spontaneous polarization and the magnetization. Room temperature multiferroic materials with high magnetoelectric couplings are desirable, because they can support novel functionalities in electronic devices [34, 196]. Magnetostructural and magnetoelectric couplings have been observed in a number of materials, including bulk [197, 198] and layered [199] manganites, epitaxial EuTiO$_3$ [200], EuSe/PbSe$_{1-x}$Te$_x$ multilayers [201], and SrRuO$_3$/SrTiO$_3$ oxide interfaces [202].

Because of the distinct natures of ferroelectric and ferromagnetic ordering, it has proved difficult to find a single-phase room temperature multiferroic material with large polarization, large magnetization, and large magnetoelectric and/or magnetoelectric coupling [36]. Most current multiferroic devices are based on nanocomposites [37, 196], and advances in the synthesis of artificially

structured materials further support studies of novel multiferroic heterostructures [51]. Exploring the coupling of ferroelectric and/or magnetic states to strain has shown to be exceptionally fruitful in many multiferroic nanocomposites [37]. The challenge is to anticipate what new properties can arise in such heterostructures from combining two distinct materials, and how these properties depend on the geometry of the combination.

First-principles approaches are ideally suited for meeting this challenge. These methods allow searching over a variety of compositions, heterostructure geometries, and structure types to find a material with the desired properties [203]. With first-principles methods, it is possible also to identify and characterize low-energy alternative structures; though they are not manifest in the bulk, they can become physically relevant with changes in the external parameters and boundary conditions produced in a nanocomposite.

In this chapter, we use first principles calculations to explore the structure and properties of a prototypical atomic-scale checkerboard of $BiFeO_3$ and $BiMnO_3$ (Fig 4.1). Ferroelectric antiferromagnetic (AFM) bulk $BiFeO_3$ and half-metallic ferromagnetic (FM) bulk $BiMnO_3$ are good candidates for a nanocomposite with ferroelectric-ferromagnetic (multiferroic) behavior. The properties of the atomic-scale checkerboard are found to be directly related to the properties of the bulk constituents in their ground states and in low-energy alternative structures. The ground state of the $BiFeO_3$-$BiMnO_3$ atomic-scale checkerboard is multiferroic, i.e. ferroelectric and ferrimagnetic, acquiring the desired properties from the constituents. In addition, we show that the $BiFeO_3$-$BiMnO_3$ atomic scale checkerboard displays a magnetostructural effect, namely, it changes its magnetic ordering with the change of its crystal structure. This effect is argued to be inherent to B-site cation checkerboard geometry, resulting from magnetic frustration for the particular arrangement of cations and bonds.

The organization of this chapter follows. In Sec. 4.2, we describe the first-principles method and the structural distortions and magnetic orderings considered. Results for low-energy alternative structures of bulk $BiFeO_3$ and $BiMnO_3$ are reported in Secs. 4.3 and 4.4, respectively. The ground

state of the $BiFeO_3$-$BiMnO_3$ atomic-scale checkerboard is shown to be ferroelectric and ferrimagnetic in Sec. 4.5. A simple Heisenberg model is constructured to represent the energies of various magnetic states of this checkerboard computed from first principles. In Sec. 4.6, the effect of structural distortions on the magnetic ordering of the nanocheckerboard is explored, and we relate the properties of alternative low-energy structures of the checkerboard to those of bulk $BiFeO_3$ and $BiMnO_3$. Anisotropic epitaxial strain is shown to drive a magnetic transition in the atomic-scale checkerboard in Sec. 4.7. We study the effect of B-site cation arrangement on magnetic properties of the $BiFeO_3$-$BiMnO_3$ system in Sec. 4.8. The possibility of experimentally realizing a $BiFeO_3$-$BiMnO_3$ nanocheckerboard is discussed in Sec. 4.9. Conclusions are presented in Sec. 4.10.

4.2   Method

First-principles calculations are performed using density functional theory within the local spin-density approximation with Hubbard U (LSDA+U) method as implemented in the Vienna *ab initio* simulation package VASP-4.6.34 [86, 87]. Projector-augmented wave potentials (PAW) [204, 205] are used with 15 valence electrons for Bi ($5d^{10}6s^26p^3$), 14 for Fe ($3p^63d^64s^2$), 13 for Mn ($3p^63d^54s^2$), and 6 for O ($2s^22p^4$). The robustness of the results is tested with two different implementations of the rotationally invariant LSDA+U version. The first is due to Liechtenstein [206] with effective on-site Coulomb interaction $U_{Fe} = U_{Mn} = 5eV$ and effective on-site exchange interaction $J_{Fe} = J_{Mn} = 1eV$. The second is due to Dudarev [207], with $U_{Mn}^{eff} = 5.2eV$, $U_{Fe}^{eff} = 4eV$, where $U^{eff} = U - J$. Both implementations treat localized d electron states in Fe and Mn. It has previously been shown that these U and J values give good agreement with experiment in bulk $BiFeO_3$ [56]. The value $U_{Mn}^{eff} = 5.2eV$ has previously been used for bulk $BiMnO_3$ ground state calculations [57].

The $BiFeO_3$-$BiMnO_3$ atomic-scale checkerboard is shown in Fig. 4.1. $BiFeO_3$ and $BiMnO_3$ alternate at the atomic level, forming a checkerboard pattern in the xy plane and pillars of the same composition along z. The supercell is $\sqrt{2}a \times \sqrt{2}a \times 2c$, containing two Fe and two Mn. In the limit of the atomic-scale pillars considered here, the checkerboard structure is the same as that of a
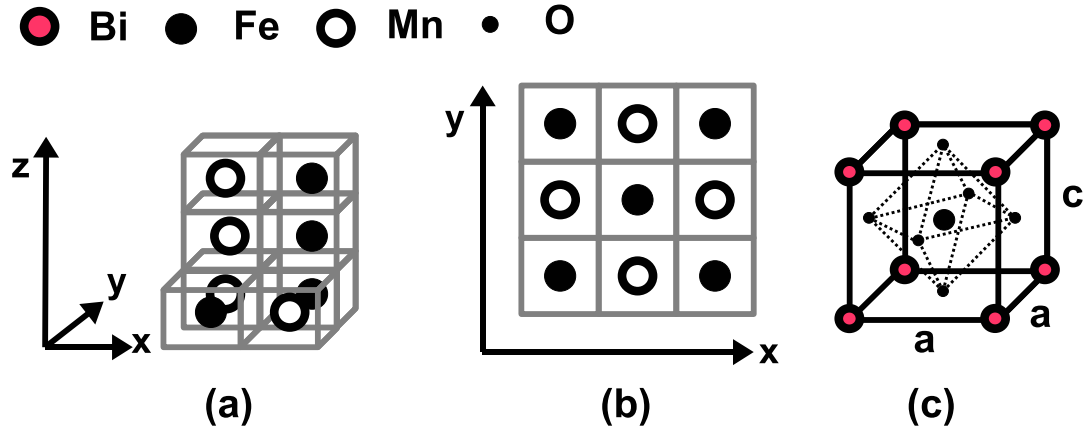
Figure 4.1: (a) BiFeO$_3$-BiMnO$_3$ atomic-scale checkerboard. (b) Top view of the atomic-scale checkerboard. (c) Perovskite cell. Dashed lines show an oxygen octahedron surrounding the B-site (Fe, or Mn) cation.

(110)-oriented superlattice.

We consider two additional types of B-site cation-ordered BiFeO$_3$-BiMnO$_3$ systems: a (001)-oriented layered superlattice, with single unit-cell Fe and Mn layers alternating along z, and a rocksalt structure, with Fe and Mn alternating in every other unit cell ((111) superlattice in the atomic-scale limit considered here). In both cases, the supercell is $\sqrt{2}a \times \sqrt{2}a \times 2c$. For consistency, we take the supercell for bulk BiFeO$_3$ and bulk BiMnO$_3$ calculations to be $\sqrt{2}a \times \sqrt{2}a \times 2c$, except for the R3c structure, where we use a $\sqrt{2}a \times \sqrt{2}a \times \sqrt{2}a$ supercell.
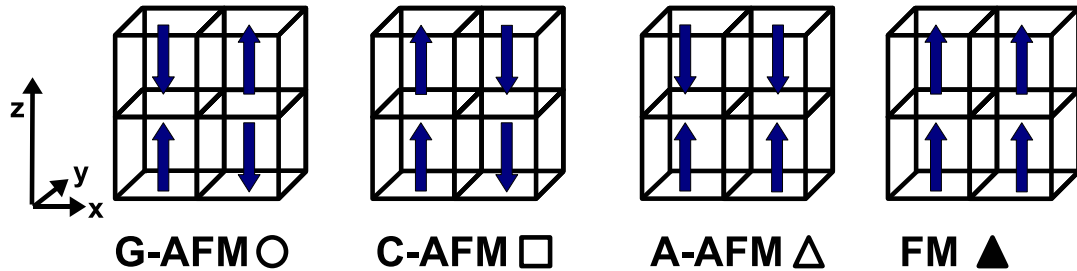
Figure 4.2: Magnetic orderings considered for bulk BiFeO$_3$ and bulk BiMnO$_3$: Symbols for each type of ordering are introduced next to each label.
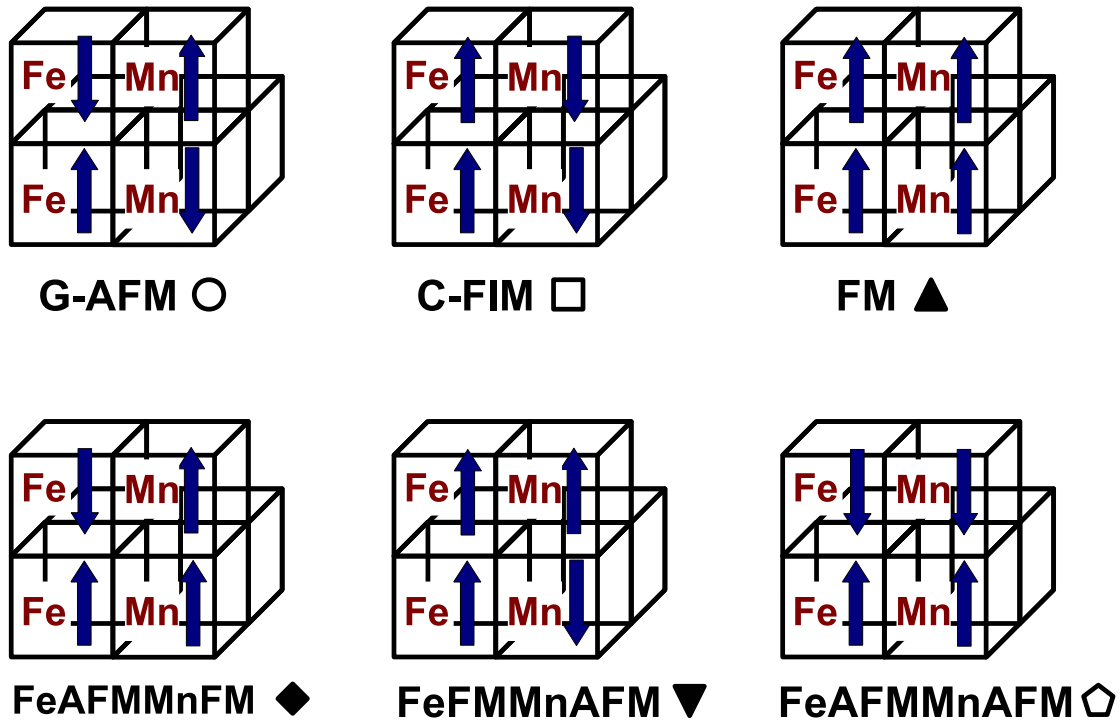
Figure 4.3: Magnetic orderings considered for the $BiFeO_3$-$BiMnO_3$ atomic-scale checkerboard compatible with the $\sqrt{2}a \times \sqrt{2}a \times 2c$ supercell. Symbols for each type of ordering are introduced next to each label.

Several types of magnetic orderings are studied here: the G-type (rocksalt), C-type, A-type AFM, and FM ordering of the local magnetic moments in bulk $BiFeO_3$, or bulk $BiMnO_3$ (see Fig. 4.2). All orderings considered are collinear; this is supported by recent neutron scattering measurements on $BiFeO_3$ doped with Mn [208], that indicate collinear AFM ordering.

Magnetic orderings of the $BiFeO_3$-$BiMnO_3$ atomic-scale checkerboard are shown in Fig. 4.3, where we consider six collinear orderings of Fe and Mn spins. Similarly, six collinear orderings of the magnetic Fe and Mn spins are explored in the $BiFeO_3$-$BiMnO_3$ (001)-oriented superlattice and the rocksalt structure. For the (001)-oriented superlattice, these orderings are described by the notation FeFM (FeAFM), or MnFM (MnAFM), referring to the FM (AFM) ordering for the Fe (Mn) moments in the relevant layer, respectively, with the remaining ambiguities resolved as follows: FeAFMMnAFM magnetic order has AFM ordered Fe and Mn layers with FM order along

Table 4.1: Resulting space groups for considered structural distortions (see Fig. 1.4). Pm$\bar{3}$m is the ideal perovskite structure and P4/mmm is the uniformly strained tetragonal unit cell.

Modes	$\Gamma_4^-(z)$	$M_3^+(z)$	$M_3^+(z)$ and $\Gamma_4^-(z)$	$R_4^+(y)$	$R_4^+(y)$ and $\Gamma_4^-(y)$	$R_4^+([111])$	$R_4^+([111])$ and $\Gamma_4^-([111])$
Abbrevation	$\Gamma_4^-(z)$	$M_3^+(z)$	$M\Gamma(z)$	$R_4^+(y)$	$R\Gamma(y)$	$R_4^+(d)$	$R\Gamma(d)$
Space Group	P4mm	P4/mbm	P4bm	I4/mcm	I4cm	R$\bar{3}$c	R3c

the mixed Fe-Mn chains in the z direction, while G-AFM designates the case with AFM order along the mixed chains; similarly, FeFMMnFM has FM ordered Fe and Mn layers with AFM order, while FM designates the case with FM order along the mixed chains. For the rocksalt structure, we consider FM and G-AFM ordering, FeAFMMnFM ordering, referring to FM ordered Mn sublattice and AFM ordered Fe sublattice; similarly we consider FeFMMnAFM ordering with FM ordered Fe and AFM ordered Mn sublattices, respectively. Finally, the FMFM ordering has AFM ordered Mn and Fe sublattices, which are coupled FM in each Fe-Mn z layer, while the AFMAFM ordering has AFM ordered Mn and Fe sublattices coupled AFM in each Fe-Mn z layer.

Structures generated by three modes of the cubic perovskite structure are considered (see Fig. 1.4) [42]: (a) the zone center polar Γ_4^- mode, (b) the M_3^+ oxygen octahedron rotations (all rotations about a given axis are in phase), and (c) R_4^+ rotations (sense of rotations alternates along the rotation axis). Space groups corresponding to the structural distortions considered are presented in Table 4.1, and we use the notation c-, l-, or r- to refer to the structural distortion of the B-site cation-ordered checkerboard, layered superlattice, or rocksalt structure, respectively. To search for the ground state for a given magnetic ordering and structure type, we perform structural relaxation with the conjugate gradient algorithm. Both the cell shape and the cell volume are relaxed; more specifically, the ions are relaxed towards equilibrium positions until the Hellmann-Feynman forces are less than $10^{-3}eV/\mathring{A}$. An energy cutoff $550eV$ for the plane wave basis set is used. Convergence in the energy is reached with precision $10^{-7}eV$. A Monkhorst-Pack k-point grid [209] is generated with density $4 \times 4 \times 4$ for the ($\sqrt{2} \times \sqrt{2} \times \sqrt{2}$) supercell, and $4 \times 4 \times 2$ for the ($\sqrt{2} \times \sqrt{2} \times 2$) supercell.

For magnetic energy calculations (Secs. 4.5.2 and 4.8), we use the energy cutoff $800eV$, and the Monkhorst-Pack k-point grid with density $6 \times 6 \times 4$. Gaussian broadening of the partial occupancies for each wavefunction is $0.05eV$. A tetrahedron method with Blochl corrections [210] is used for the density of states (DOS) calculations, with the Monkhorst-Pack k-point grid $4 \times 4 \times 4$ for the $(\sqrt{2} \times \sqrt{2} \times \sqrt{2})$ and $8 \times 8 \times 4$ for the $(\sqrt{2} \times \sqrt{2} \times 2)$ supercell.

The rotational distortion can be quantified using the oxygen octahedron rotational angle Θ defined specifically for each oxygen in the octahedron as

$$cos\Theta = \frac{\vec{u} \cdot \vec{v}}{|\vec{u}||\vec{v}|}, \tag{4.1}$$

where $\vec{u}$ is the shortest vector from the rotation axis to the reference position of the oxygen, and $\vec{v}$ is the shortest vector from the rotation axis to the position of the oxygen in the distorted structure. The rotation axis is [001] and [010] for the $M_3^+(z)$ and $R_4^+(y)$ distortions respectively, and the threefold axis (body diagonal of the cube or distorted cube) for the $R_4^+([111])$ distortion. Due to deformation of the oxygen octahedron in the BiFeO$_3$-BiMnO$_3$ checkerboard structures, these angles may be different for different oxygens in the same octahedron. We report an average value if the range is small; otherwise the lower and upper limits of the range are presented.

The polar distortions of the various structures can be quantified by estimating the polarization based on a linearized expression with nominal charges:

$$\vec{P} = \frac{|e|}{\Omega} \sum_j q_j \Delta \vec{u_j}, \tag{4.2}$$

where $\vec{P}$ is the polarization, $\Delta \vec{u_j}$ is the displacement of the jth ion with respect to its ideal perovskite position, q_j is the nominal charge of the jth ion ($q_{Bi} = +3$, $q_{Fe} = +3$, $q_{Mn} = +3$, $q_O = -2$), and Ω is the unit cell volume.

For selected structures the true value for the spontaneous polarization is computed using the Berry phase method [39, 40] as implemented in VASP–4.6.34. In this formalism, the polarization is only well-defined $mod\ e\vec{R}/\Omega$, where $\vec{R}$ is any lattice vector and Ω is the primitive-cell volume;

thus possible values of the polarization are points on the lattice defined by $\vec{P}_0 + e\vec{R}/\Omega$, where $\vec{P}_0$ is the value directly obtained from the Berry phase calculation. Choosing the lattice point (or branch) that corresponds to the measured switching polarization (e.g. in an electrical hysteresis loop) is done by computing the polarization of states closely spaced along an adiabatic path connecting the structure of interest to a high-symmetry reference structure. These laborious calculations can be avoided by an approach based on the reformulation of the polarization in terms of Wannier function centers [39]; the switching polarization is obtained from the difference between the two symmetry-related variants by associating the Wannier centers with the same atoms in both structures [211, 212]. Due to incompatibility between the Wannier90 and the VASP codes, we cannot use this latter approach here; we make the necessary branch choices based on computations along adiabatic paths combined with the nominal-charge polarization estimate.

4.3 BiFeO$_3$ Structures

In agreement with previous first-principles calculations and experiment [56, 208, 213, 214], we find that the ground state structure of BiFeO$_3$ has rhombohedral R3c symmetry, which is a combination of the rotational $R_4^+([111])$ mode (counter-rotations of the oxygen octahedra about the [111] axis) and a polar $\Gamma_4^-([111])$ modes, with Bi, Fe, and O displaced relative to one another along [111] and further distortion of the oxygen octahedra by displacement of the O displaced perpendicular to [111]. [42] The oxygen octahedra rotation angle is large, about $14°$, and is comparable to rotations in other perovskites [215]. The R3c ground state has G-AFM (rocksalt) ordering (see Fig. 4.2), and Fe local magnetic moment of $4\mu_B$. [208] The density of states (DOS) is plotted in Fig. 4.4: it has a $2eV$ band gap that separates occupied and unoccupied Fe d states. The polar character of BiFeO$_3$ arises from the polar $\Gamma_4^-([111])$ mode, and the spontaneous polarization using the Berry phase method is $P^{R3c} = 90\mu C/cm^2$ along the [111] direction.

Next alternative structures of BiFeO$_3$ are studied, and we consider those generated by freezing in linear combinations of the rotational M_3^+, R_4^+, and polar Γ_4^- modes, and four magnetic orderings (see Fig. 4.2). Their energies are plotted in Fig. 4.5 (see also Table 4.2). By symmetry, the FM

Figure 4.4: Density of states (DOS) of the R3c G-AFM ground state (GS) of BiFeO$_3$. Spin up states are plotted by solid line and spin down states by a dashed line (inverted view). The zero is set to the valence band maximum. DOS shows an insulating band gap of 2 eV.

ordering has the same energy for the $\Gamma_4^-(z)$ and $\Gamma_4^-(y)$ structures; this is also true for the G-AFM ordering. In contrast, the C-AFM ordering has different energy for the $\Gamma_4^-(z)$ and $\Gamma_4^-(y)$ structures; this is also true for the A-AFM ordering, as the y and z directions for these spin arrangements are not symmetry-related (see Figs. 4.2 and 4.5).

For all structural distortions considered, the favored magnetic ordering is G-AFM (open circle). This is consistent with the Goodenough-Kanamori rules: either a strong σ bond is formed between Fe e_g and the neighbouring O p orbitals in an ideal $180°$ Fe-O-Fe bond (ideal perovskite structure), or a weak π bond is formed between Fe t_{2g} and O p orbitals when the bond is bent towards $90°$ (as the structure is distorted); in both cases, the AFM superexchange is favored [216–218].
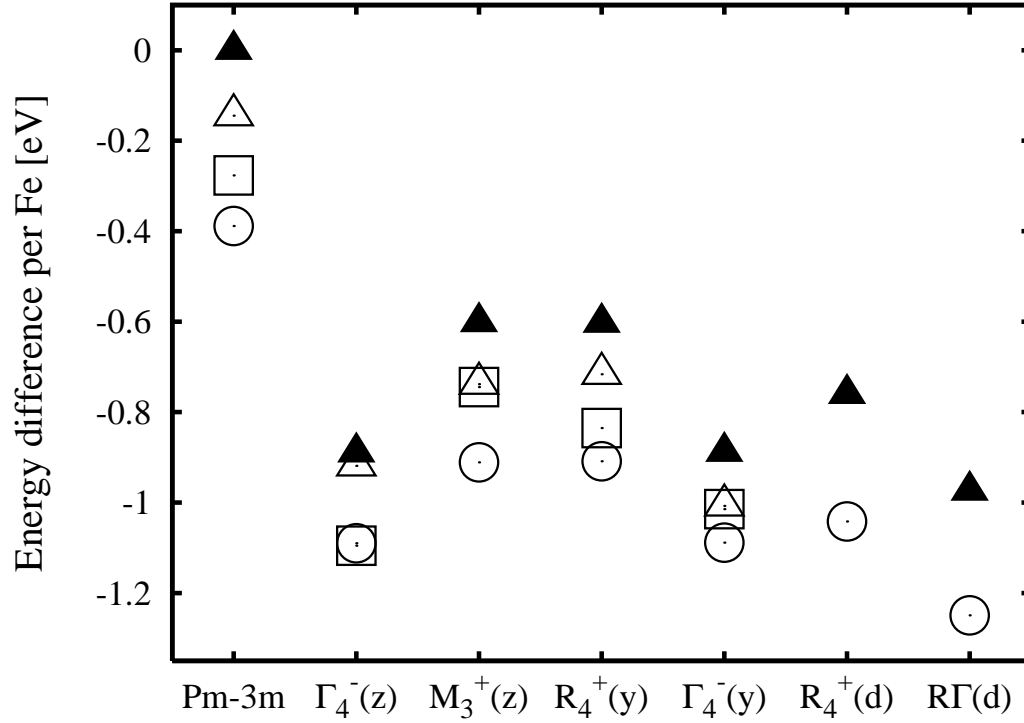
Figure 4.5: Structural energetics of bulk BiFeO$_3$. Energy difference per Fe for different magnetic orderings (see Fig. 4.2) and structural distortions (see Fig. 1.4 and Table 4.1) relative to the FM Pm$\bar{3}$m structure.

The most favorable low-energy alternative structures and the ground state of BiFeO$_3$ are presented in Table 4.2. The low-energy $\Gamma_4^-(z)$ structure, with P4mm symmetry, is the supertetragonal structure with $c/a \sim 1.3$, previously discussed elsewhere [219, 220]. It has been shown recently that this phase can be stabilized in BiFeO$_3$ thin films [221]. The polarization computed by the Berry phase method [219] is $P^{P4mm} \approx 150\mu C/cm^2$. The nominal-charge estimates are therefore smaller than the true values for both the P4mm and R3c structures, but the relative values are well reproduced. The polar distortion is dominant in all structures considered; the rotation-only structures are higher in energy, and the presence of a polar distortion tends to stabilize the rotational instabilities. For example, the $\Gamma_4^-+M_3^+$ and $\Gamma_4^-+R_4^+$ distortions relax back to Γ_4^- with zero oxygen octahedron rotation angle. The only exception is the R3c structure, in which the rotational and polar distortions coexist.

Table 4.2: GS and low-energy alternative structures of bulk BiFeO$_3$. The energy difference ΔE is given with respect to the FM Pm$\bar{3}$m structure, as in Fig. 4.5. Polarization P is estimated from the nominal charges (Eq. (4.2)). Also included are the band gap Δ and the a and c lattice constants for the $\sqrt{2}a \times \sqrt{2}a \times 2c$ supercell of P4mm, and the a lattice constant and the angle α for the $\sqrt{2}a \times \sqrt{2}a \times \sqrt{2}a$ supercell of R3c.

Space Group	P4mm		R3c
Modes	$\Gamma_4^-(z)$		$R_4^+([111]), \Gamma_4^-([111])$
Mag. order	G-AFM	C-AFM	G-AFM
ΔE[eV/Fe]	-1.09	-1.10	-1.25
Δ [eV]	1.75	2.23	1.99
P[$\mu C/cm^2$]	113.6	116.2	62.1
a/ c [Å]	3.68/ 4.64	3.67/ 4.68	$5.52, \alpha = 59.8°$

4.4 BiMnO$_3$ Structures

Previous first principles calculations show that the ground state structure of bulk BiMnO$_3$ is monoclinic centrosymmetric C2/c with zero spontaneous polarization [57] and FM ordering [70, 222, 223]. Bismuth (Bi) cations are off-center due to stereochemically active Bi lone pairs, and the Jahn-Teller activity of Mn^{3+} further distorts the structure [69]. Optimizing the atomic positions and lattice constants, we performed a first-principles calculation for this structure to find an energy gain of $1.26 eV$/Mn relative to the the ideal cubic perovskite structure with G-AFM ordering and $a_0 = 3.83\mathring{A}$; the latter is used as our reference state throughout this section.

We study low-energy alternative structures of BiMnO$_3$ compatible with a $\sqrt{2} \times \sqrt{2} \times 2$ supercell. Results are presented in Fig. 4.7. The lowest energy structure has R3c symmetry, the same structure type as the ground state of BiFeO$_3$. It is FM, with magnetic moment $3.9\mu_B$ per Mn. This structure lies only $43 meV$/Mn above the BiMnO$_3$ monoclinic ground state. The computed DOS is shown in Fig. 4.6: the system is half-metallic, with a gap of 3.25 eV in the spin down channel. As an aside, we note that it might be useful to stabilize BiMnO$_3$ as a half-metal in this low energy structure for possible applications in spintronics [224].

For all structural distortions considered, the favored magnetic ordering is FM, consistent with previous analysis that showed that BiMnO$_3$ favors FM structures with a half-metallic character [69,
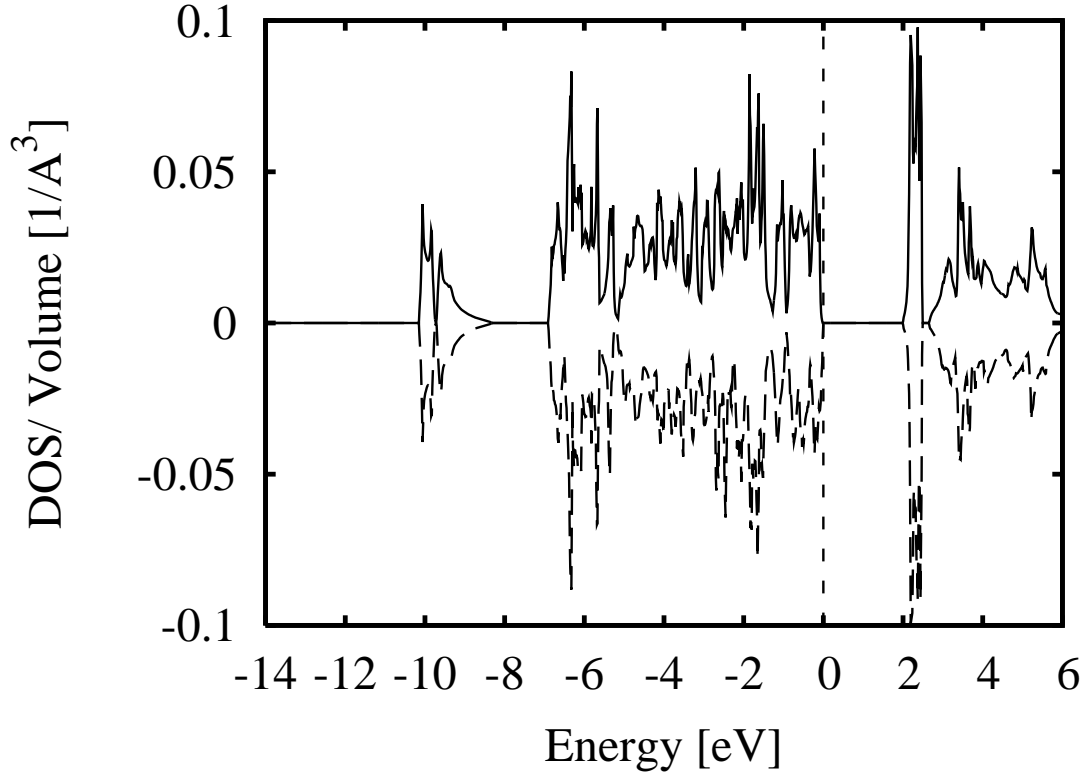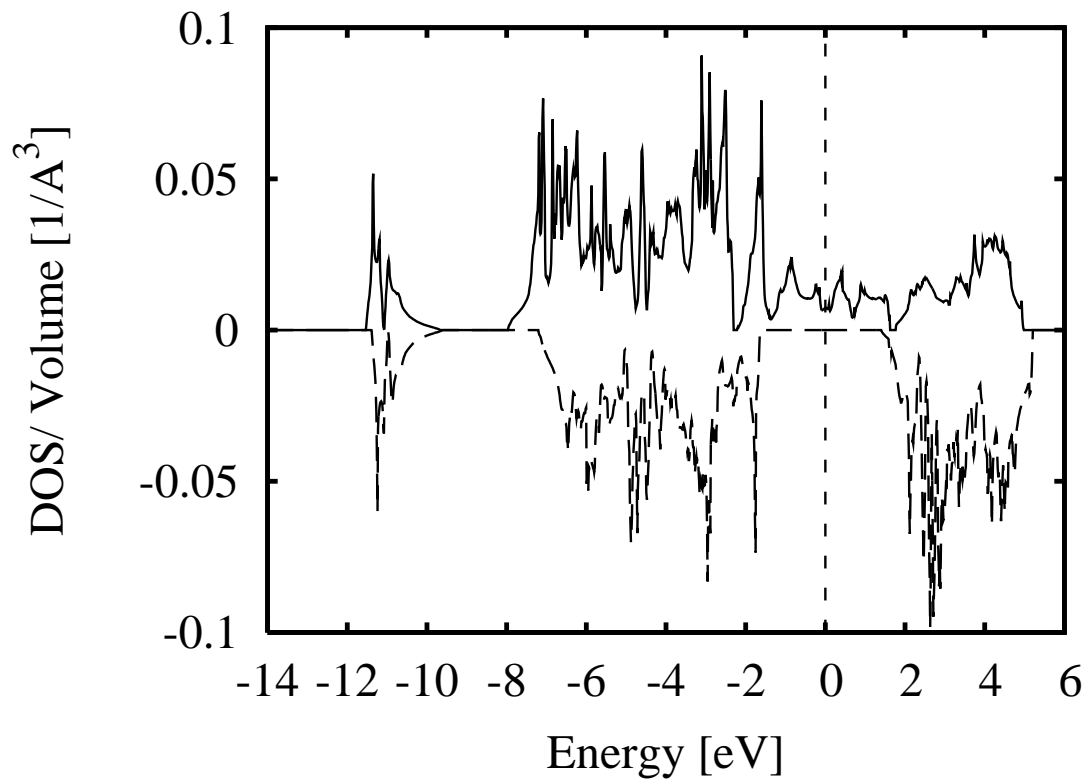
Figure 4.6: Density of states (DOS) of the R3c FM alternative structure of BiMnO$_3$. Spin up states are plotted by solid line and spin down states by a dashed line (inverted view). Fermi energy is shown by the vertical dashed line crossing zero. DOS shows a half-metallic character.
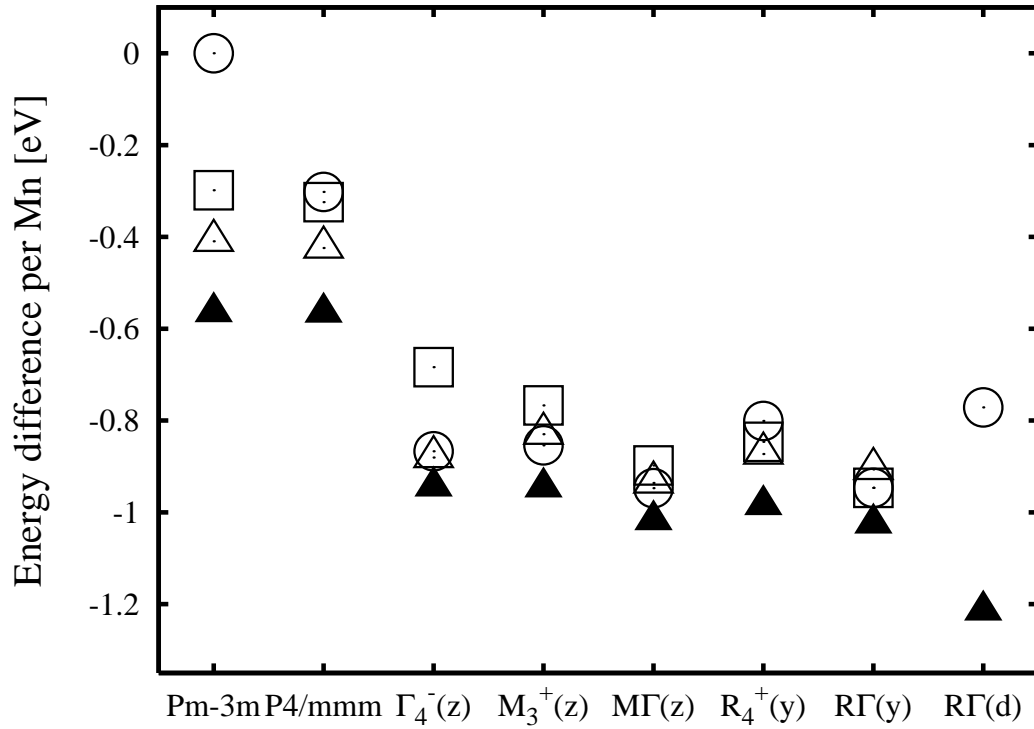
Figure 4.7: Structural energetics of bulk BiMnO$_3$. Energy difference per perovskite cell (Mn) for different magnetic orderings (see Fig. 4.2) and for structural distortions (see Fig. 1.4 and Table 4.1) generated by the specified modes.

225]. The ferromagnetism in BiMnO$_3$ can be explained by a combination of Goodenough-Kanamori rules and orbital ordering [36, 69, 70, 226]. Structural distortions (either oxygen octahedron rotations or polar distortion) widen the spin-down gap (see Table 4.3); a similar trend is observed for the band gap in BiFeO$_3$ (see Table 4.2). A small band gap opens with a monoclinic distortion in the FM BiMnO$_3$ ground state [69, 223].

The Jahn-Teller active Mn^{3+} configuration tends to favor elongation of the oxygen octahedron. In contrast to BiFeO$_3$, in which the polar instability strongly dominates, the rotational and polar instabilities in BiMnO$_3$ are comparable in magnitude, as can be seen by comparing the energies of the $\Gamma_4^-(z)$, $M_3^+(z)$ and $R_4^+(y)$ states. The latter two states have a small residual polar instability. A polar distortion along a Cartesian axis lowers the energy of the G-AFM state so that the energy difference between this state and the FM ground state is greatly reduced; this does not occur if the

Table 4.3: Low energy alternative structures of FM bulk $BiMnO_3$. The energy difference ΔE is calculated with respect to the G-AFM $Pm\bar{3}m$ structure (as in Fig. 4.7). Listed are values of the spin-down band gap Δ_{hm} in the half-metallic structures or metallic (m) character, the oxygen octahedron rotational angle Θ (see Sec. 4.2), and the a and c lattice constants of the $\sqrt{2} \times \sqrt{2} \times 2$ supercell.

Space Group	P4/mmmm	P4bm	I4cm	R3c
Modes	-	$M_3^+(z), \Gamma_4^-(z)$	$R_4^+(y), \Gamma_4^-(y)$	$R_4^+([111]), \Gamma_4^-([111])$
ΔE [eV/Mn]	-0.57	-1.02	-1.03	-1.22
Δ_{hm} [eV]	m	0.73	2.74	3.25
$\Theta[^\circ]$	-	11.4	12.0	13.3
a/ c [Å]	3.83/ 3.86	3.81/ 4.01	3.81/ 3.83	5.51, $\alpha = 60^\circ$

polar distortion is along [111] as in the R3c phase. The octahedral rotation angles in the low-energy

$BiMnO_3$ structures are all similar in magnitude, varying between $11 - 14^\circ$, with an angle of 13° for

the FM R3c structure. The value of the octahedral rotation angle in the G-AFM R3c structure, 14°,

is the same as in G-AFM R3c $BiFeO_3$.

4.5 $BiFeO_3$-$BiMnO_3$ Nanocheckerboard Ground State

4.5.1 Crystal structure, magnetization and polarization

In the search for the ground state of the atomic-scale checkerboard cation ordering, we considered

the six collinear magnetic states of Fig. 4.3 and four different structures: the tetragonal P4/mmm

structure and three additional structures, obtained by freezing in a $\Gamma_4^-(z)$ mode, a combination of

$R_4^+(y)$ and $\Gamma_4^-(y)$, and a combination of $R_4^+(111)$ and $\Gamma_4^-(111)$. We designate these latter three

structures by the space group they would have if all B sites were occupied by the same cation, with

the prefix c- to remind us that the actual symmetry is lower due to the checkerboard ordering: c-

P4mm, c-I4cm, and c-R3c. The GS of the $BiFeO_3$-$BiMnO_3$ nanocheckerboard is found to be c-R3c,

as could be expected based on the R3c GS of bulk $BiFeO_3$, and on our results for bulk $BiMnO_3$. The

magnetic ordering in the c-R3c GS is FeAFMMnFM. Fe magnetic moments are ordered AFM along

the Fe pillars and Mn magnetic moments are ordered FM along the Mn pillars, as expected from

the G-AFM and FM ground states of $BiFeO_3$ and $BiMnO_3$, respectively (see Secs. 4.3 and 4.4).

AFM and FM xy layers alternate along z as is sketched in Fig. 4.3. The computed Fe and Mn local magnetic moments are $4.1\mu_B$ and $3.8\mu_B$, respectively; these are the same values as those reported here in the parent compounds BiFeO$_3$ and BiMnO$_3$. Although the contribution from Fe magnetic moments to the net magnetization cancels due to the AFM pillar ordering, the contribution from Mn moments adds, leading to a net magnetization of $3.8\mu_B$ per Fe-Mn pair.
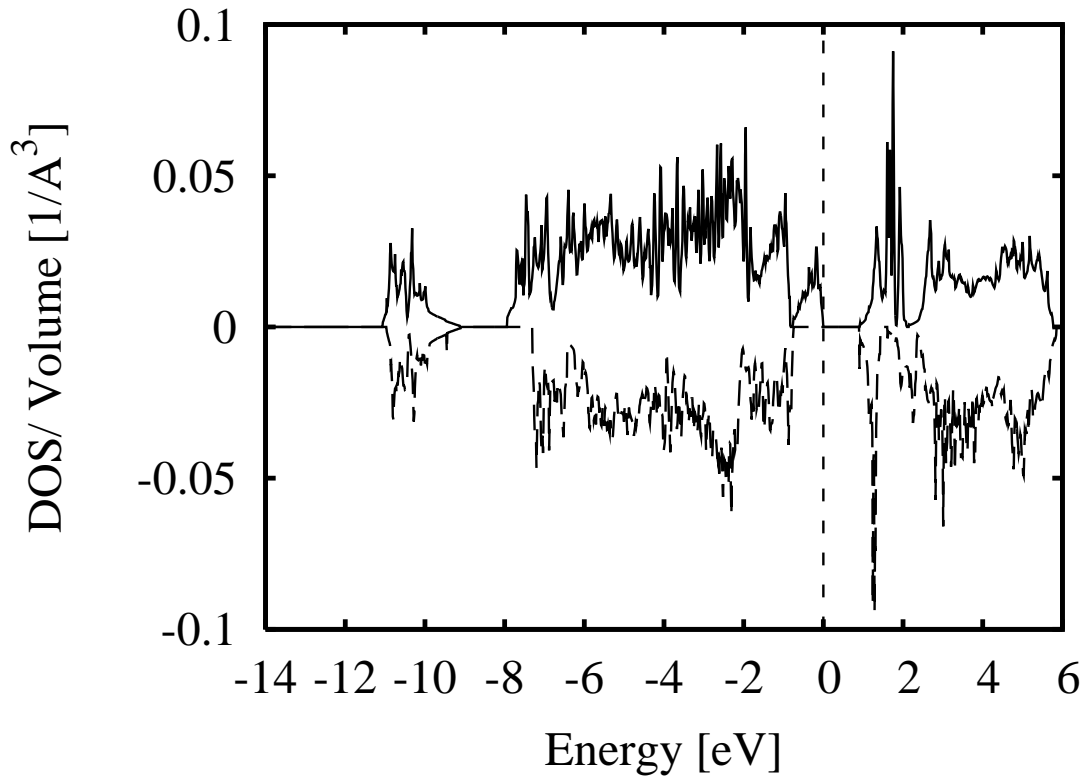
Figure 4.8: Density of states (DOS) of the c-R3c FeAFMMnFM ground state (GS) of BiFeO$_3$-BiMnO$_3$ nanocheckerboard. Spin up states are shown by a solid line and spin down states by a dashed line. The zero is set to the valence band maximum. The band gap in the spin-up channel is 0.9 eV.

The DOS of the c-R3c FeAFMMnFM GS is shown in Fig. 4.8. The general features are very similar to those found in BiFeO$_3$ (Fig. 4.4) and BiMnO$_3$ (Fig. 4.6), the main difference being that the spin-up Mn states at the Fermi level in BiMnO$_3$ have split to open a gap, with the occupied states at the top of the valence band narrowing the gap to $0.9eV$.

Direct calculation of the spontaneous polarization using the Berry phase method for the c-R3c
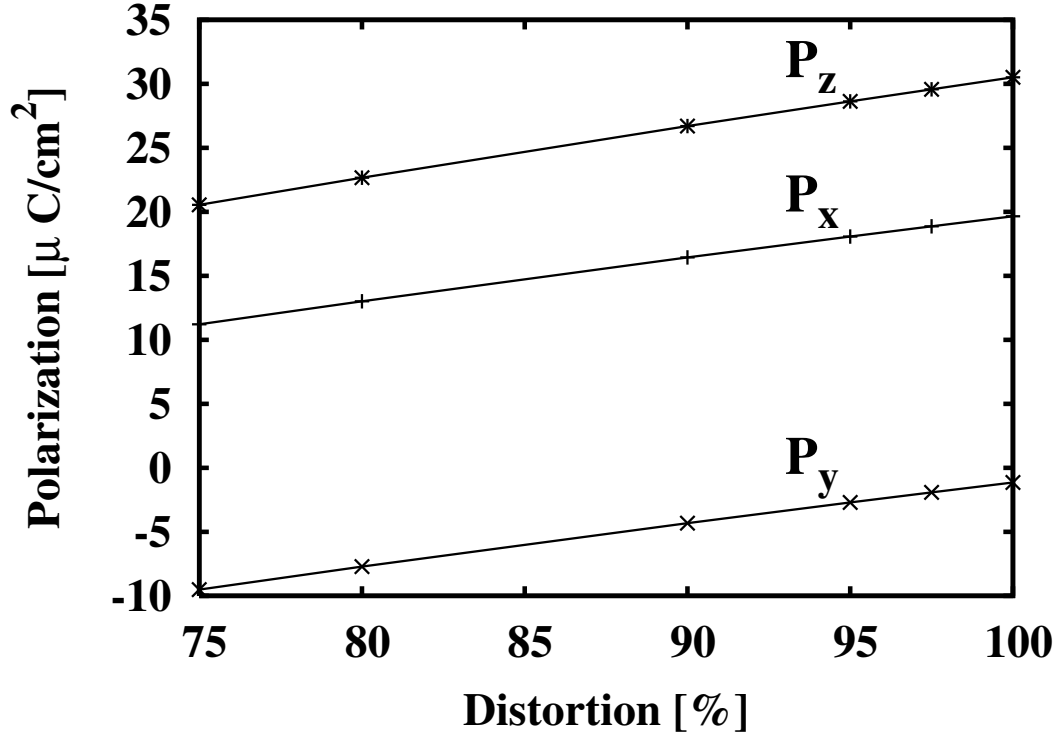
Figure 4.9: Spontaneous polarization $\vec{P} = (P_x, P_y, P_z)$ as a function of the structural distortion of the c-R3c FeAFMMnFM BiFeO$_3$-BiMnO$_3$ nanocheckerboard. 100% distortion corresponds to the c-R3c ground state structure, and 0% to the ideal perovskite structure.

GS yields a value of $\vec{P} = (19.6, \ -1.1, \ 30.5) \ \mu C/cm^2$. This is well defined only up to the polarization lattice $e\vec{R}/\Omega$ [39, 40], which in this case is $(13.2, \ 13.1, \ 0.1)n_1 + (-13.2, \ 13.0, \ 0.1)n_2 + (0.0, \ 0.2, \ 26.6)n_3 \ \mu C/cm^2$, where $\vec{n}$ is a vector of integers. To determine the branch that corresponds to the switching polarization, we compute the polarization along a structural deformation path that linearly connects the c-R3c GS to the ideal cubic perovskite structure. As shown in Fig. 4.9, the computation is performed for structures down to 75% of the full distortion (at which point the structures become metallic) and then linearly extrapolated to 0% using the expression

$$\Delta\vec{P}_{100\%-0\%} = 4 \times \Delta\vec{P}_{100\%-75\%} = (33.8, 33.5, 39.8)\mu C/cm^2. \tag{4.3}$$

The magnitude of this estimate, $62.0\mu C/cm^2$, suggests the branch choice $\vec{P}_{bp} = (32.9, \ 38.0, \ 30.7)$

Table 4.4: B-site-cation-oxygen-B-site-cation (B-O-B) bonds in the c-R3c ground state (GS) of the $BiFeO_3$-$BiMnO_3$ nanocheckerboard. B-O and O-B bond lengths and the B-O-B bond angle are given. Atoms are numbered as in Fig. 4.10. The subscript indicates the cartesian direction along which the bond lies.

B-O-B bond	Notation	$|B-O|$ [Å]	$|O-B|$ [Å]	Angle
$(Fe_1 - O_7 - Fe_2)_z$	J_{Fe}	1.93	2.08	153.8°
$(Fe_2 - O_5 - Fe_1)_z$	J_{Fe}	1.96	2.08	156.8°
$(Mn_1 - O_8 - Mn_2)_z$	J_{Mn}	2.10	1.91	153.7°
$(Mn_2 - O_6 - Mn_1)_z$	J_{Mn}	1.87	2.18	156.3°
$(Mn_1 - O_1 - Fe_1)_x$	J_{int}^{α}	1.92	2.06	166.8°
$(Fe_1 - O_2 - Mn_1)_x$	J_{int}^{β}	1.97	1.97	156.8°
$(Mn_1 - O_3 - Fe_1)_y$	J_{int}^{α}	1.95	1.95	165.1°
$(Fe_1 - O_4 - Mn_1)_y$	J_{int}^{β}	2.04	1.91	155.3°
$(Mn_2 - O_9 - Fe_2)_x$	J_{int}^{β}	2.05	2.03	152.0°
$(Fe_2 - O_{10} - Mn_2)_x$	J_{int}^{γ}	1.94	2.11	143.3°
$(Mn_2 - O_{11} - Fe_2)_y$	J_{int}^{β}	2.05	1.95	151.1°
$(Fe_2 - O_{12} - Mn_2)_y$	J_{int}^{γ}	2.07	1.98	144.1°

$\mu C/cm^2$ with magnitude $|P_{bp}| = 58.9 \mu C/cm^2$. However, we would expect it to be considerably larger, based on comparison between the Berry phase $|P|$ of bulk $BiFeO_3$ and the $|P|$ computed using nominal charges (see Sec. 4.3); following this intuition we would make the branch choice $\vec{P}_{bp} = (46.1,\ 51.3,\ 57.4)\ \mu C/cm^2$ with magnitude $|P_{bp}| = 89.7 \mu C/cm^2$. This remaining ambiguity highlights the challenge of picking the right branch when the polarization is much larger than the quantum; in either case it is clear that the polarization of the checkerboard is comparable to the largest values found in ferroelectrics. Thus, we find that the c-R3c GS of the $BiFeO_3$-$BiMnO_3$ nanocheckerboard is multiferroic: ferroelectric, with polarization comparable to the polarization of bulk $BiFeO_3$, and ferrimagnetic, with magnetization contributed by ferromagnetic ordering in the $BiMnO_3$ component.

4.5.2 Magnetic Coupling Constants

To gain insight into the magnetic properties of the nanocheckerboard, we model the magnetic ordering energies using a nearest-neighbor (nn) Heisenberg model. The nn magnetic couplings arise
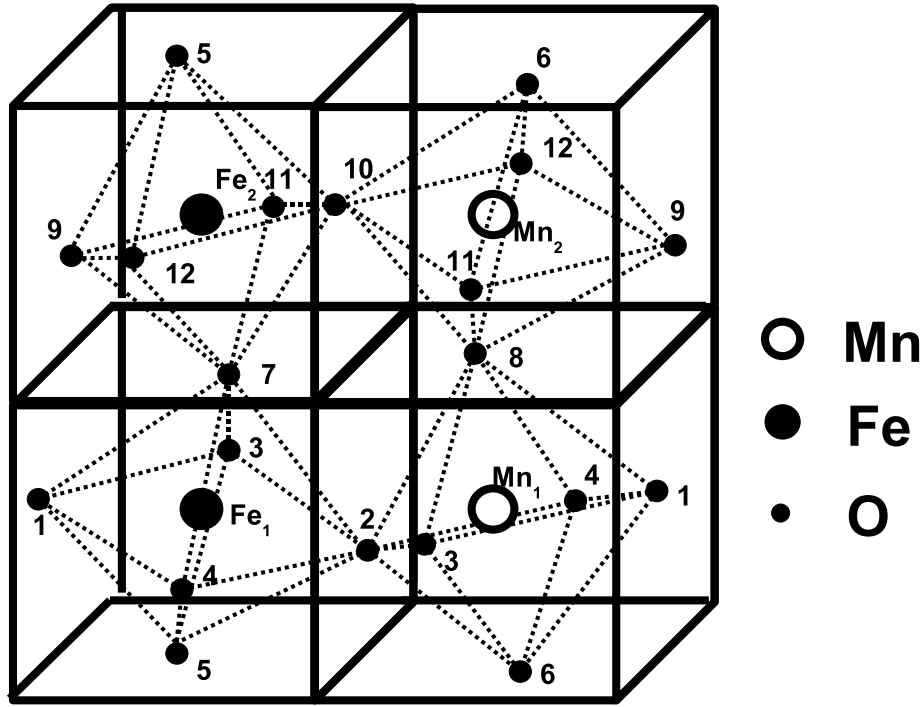
Figure 4.10: Sketch showing the displacements of oxygen atoms in the $R_4^+([111])$ mode, which contributes to the c-R3c ground state (GS) of the $BiFeO_3$-$BiMnO_3$ nanocheckerboard. Two inequivalent iron (Fe_1 and Fe_2) and manganese (Mn_1 and Mn_2) atoms and twelve oxygens ($1 - 12$) comprise the $\sqrt{2} \times \sqrt{2} \times 2$ unit cell. The corners of each cube are occupied by Bi (not shown).

from superexchange through the oxygens that lie on the bonds between the B site cations, with the strength of the superexchange being quite sensitive to the geometry of the B-O-B bond. If the structure were ideal cubic perovskite, there would be three independent couplings, J_{Fe}, J_{Mn} and J_{int}, corresponding to 180° Fe-O-Fe, Mn-O-Mn and Fe-O-Mn bonds, respectively. The analysis of the couplings in the c-R3c structure is based on the geometry of the B-O-B bonds as given in Table 4.4; the labeling of the bonds and the changes in the bonds due to the $R_4^+([111])$ mode are shown in Fig. 4.10. The two Fe-O-Fe bonds are almost identical in bond angle and bond length; this is also the case for the two Mn-O-Mn bonds. This suggests that a single value of J_{Fe} and J_{Mn} can be used for the Fe-O-Fe and Mn-O-Mn interactions, respectively. On the other hand, the mixed Fe-O-Mn bonds vary in both B-O bond length, from $1.91 - 2.11 \text{Å}$, and B-O-B bond angle, from $143.3 - 166.8°$. This suggests the use of three different coupling constants J_{int}^α, J_{int}^β or J_{int}^γ for the

Table 4.5: Calculated magnetic energies ΔE per four-perovskite unit cell (u.c.) in the c-R3c GS structure of BiFeO$_3$-BiMnO$_3$ nanocheckerboard. The notation for magnetic ordering is that of Fig. 4.3. The symbols x, y, a, b, c appearing in the magnetic energy are defined as follows: $x = J_{Fe}S_{Fe}S_{Fe}$, $y = J_{Mn}S_{Mn}S_{Mn}$, $a = J_{int}^{\alpha}S_{Fe}S_{Mn}$, $b = J_{int}^{\beta}S_{Fe}S_{Mn}$, $c = J_{int}^{\gamma}S_{Fe}S_{Mn}$.

Magnetic state	Magnetic ordering	Heisenberg energy [per u.c.]	ΔE [eV/u.c.]	Fitted ΔE [eV/u.c.]
FeAFMMnFM	Fe$_1^{\uparrow}$ Fe$_2^{\downarrow}$ Mn$_1^{\uparrow}$ Mn$_2^{\uparrow}$	$E_0 - 2x + 2y + 2a - 2c$	0.000	0.000
FeAFMMnFM	Fe$_1^{\downarrow}$ Fe$_2^{\uparrow}$ Mn$_1^{\uparrow}$ Mn$_2^{\uparrow}$	$E_0 - 2x + 2y - 2a + 2c$	0.200	0.207
G-AFM	Fe$_1^{\uparrow}$ Fe$_2^{\downarrow}$ Mn$_1^{\downarrow}$ Mn$_2^{\uparrow}$	$E_0 - 2x - 2y - 2a - 4b - 2c$	0.032	0.026
C-AFM	Fe$_1^{\uparrow}$ Fe$_2^{\uparrow}$ Mn$_1^{\downarrow}$ Mn$_2^{\downarrow}$	$E_0 + 2x + 2y - 2a - 4b - 2c$	0.143	0.152
FeFMMnAFM	Fe$_1^{\uparrow}$ Fe$_2^{\uparrow}$ Mn$_1^{\downarrow}$ Mn$_2^{\uparrow}$	$E_0 + 2x - 2y - 2a + 2c$	0.436	0.436
FeFMMnAFM	Fe$_1^{\uparrow}$ Fe$_2^{\uparrow}$ Mn$_1^{\uparrow}$ Mn$_2^{\downarrow}$	$E_0 + 2x - 2y + 2a - 2c$	0.222	0.229
FeAFMMnAFM	Fe$_1^{\uparrow}$ Fe$_2^{\downarrow}$ Mn$_1^{\uparrow}$ Mn$_2^{\downarrow}$	$E_0 - 2x - 2y + 2a + 4b + 2c$	0.275	0.284
FM	Fe$_1^{\uparrow}$ Fe$_2^{\uparrow}$ Mn$_1^{\uparrow}$ Mn$_2^{\uparrow}$	$E_0 + 2x + 2y + 2a + 4b + 2c$	0.416	0.410

Fe-O-Mn interactions based on the typical values of the bond angles, approximately 166°, 154° and 144°, respectively. Note that the angles of the Fe-O-Mn bonds in the Fe$_1$-Mn$_1$ layer in Fig. 4.10 are about 166° and 154°, while the angles in the Fe$_2$-Mn$_2$ layer are about 152° and 144°.

The values of these five exchange couplings were determined from first-principles results for the total energies of various magnetic orderings for the c-R3c GS structure of the nanocheckerboard, given in Table 4.5. The structure is fixed to that obtained for the FeAFMMnFM ordering Fe$_1^{\uparrow}$ Fe$_2^{\downarrow}$ Mn$_1^{\uparrow}$ Mn$_2^{\uparrow}$. The ordering Fe$_1^{\downarrow}$ Fe$_2^{\uparrow}$ Mn$_1^{\uparrow}$ Mn$_2^{\uparrow}$, also described as FeAFMMnFM, is a distinct state with a different (higher) energy. Similarly, for the FeFMMnAFM ordering, there are two distinct magnetic states: Fe$_1^{\uparrow}$ Fe$_2^{\uparrow}$ Mn$_1^{\downarrow}$ Mn$_2^{\uparrow}$ and Fe$_1^{\uparrow}$ Fe$_2^{\uparrow}$ Mn$_1^{\uparrow}$ Mn$_2^{\downarrow}$, with different energies as given in Table 4.5.

We express the Heisenberg magnetic energy of each magnetic state,

$$E = E_0 + \frac{1}{2}\sum_{ij} J_{ij}S_iS_j, \tag{4.4}$$

where S_i and S_j are the spins $S_{Fe} = \frac{5}{2}$, $S_{Mn} = \frac{4}{2}$ with coupling constants $J_{ij} = J_{Fe}$, J_{Mn}, J_{int}^{α}, J_{int}^{β}, J_{int}^{γ}, and E_0 is a constant. We extract values of the coupling constants by fitting the Heisenberg

model energy to the first-principles energies by the least-squares method, obtaining

$$E_0 = 218 meV, \quad J_{Fe} = 7.1 meV, \quad J_{Mn} = -3.2 meV,$$

$$J_{int}^{\alpha} = -3.0 meV, \quad J_{int}^{\beta} = 4.3 meV, \quad J_{int}^{\gamma} = 7.3 meV.$$

$$(4.5)$$

The quality of the fit can be assessed by comparing the first-principles energy to the fitted values in the fifth column of the table.

The AFM character of J_{Fe} and the FM character of J_{Mn} correspond to that of bulk G-AFM BiFeO$_3$ and bulk FM BiMnO$_3$, respectively. Their values are comparable to those obtained from the observed bulk transition temperatures within mean field theory assuming a single J: $J_{Fe,bulk} \approx$ 6.3meV and $J_{Mn,bulk} \approx -1.5meV$, respectively [64, 75–78, 227]. The correspondence is not exact because of the difference in the bond geometry between bulk BiFeO$_3$ and bulk BiMnO$_3$ and the nanocheckerboard.

In the Fe$_1$-Mn$_1$ layer, the average Fe-Mn interaction J_{int} is very weakly AFM $(J_{int}^{\alpha} + J_{int}^{\beta})/2 \gtrsim$ 0, while in the Fe$_2$-Mn$_2$ layer it is strongly AFM $(J_{int}^{\beta} + J_{int}^{\gamma})/2 > 0$. This corresponds to the preferred FeAFMMnFM ordering Fe$_1^{\uparrow}$ Fe$_2^{\downarrow}$ Mn$_1^{\uparrow}$ Mn$_2^{\uparrow}$ and explains the close competition with G-AFM ordering, in which both layers are AFM ordered (see Fig. 4.3 and Table 4.5). The exchange coupling between d^5 Fe and d^4 Mn takes place via superexchange through the bridging O. For angles close to 180°, strong σ bonding favors FM ordering. However, as the Fe-O-Mn angles deviate from 180° through the oxygen octahedron rotational distortion, the admixture of π bonding leads to an increasingly AFM character of the coupling [216–218]. This behavior can be seen in the dependence of the fitted values for J_{int} on the Fe-O-Mn angle, plotted in Fig. 4.11.

Within this nearest-neighbor Heisenberg model, we explored a wider range of possible magnetic orderings for the R3c structure nanocheckerboard, in particular, orderings with lower translational symmetry than those included in the first-principles investigation. The supercells considered included $2 \times 2 \times 2$ ($p = 8$ perovskite cells), $2 \times 2 \times 4$ and $4 \times 2 \times 2$ ($p = 16$ perovskite unit cells).
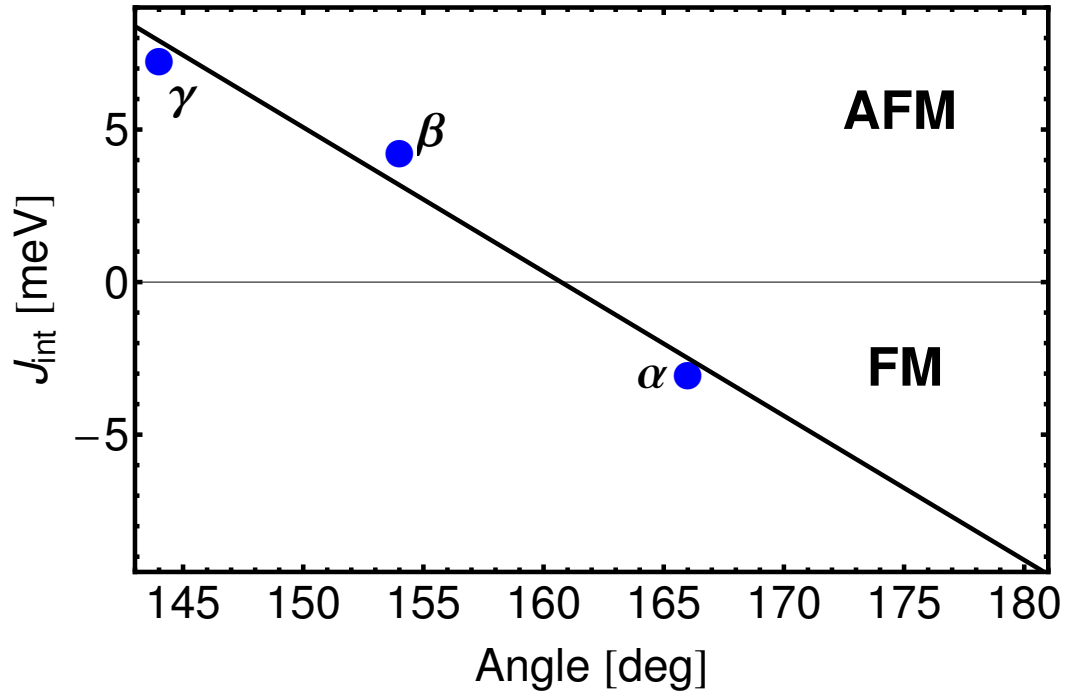
Figure 4.11: Angular dependence of the Fe-Mn magnetic exchange coupling constant J_{int} in the c-R3c GS structure of the BiFeO$_3$-BiMnO$_3$ nanocheckerboard (blue circles). The black line is a linear fit. J_{int} changes sign (AFM $J_{int} > 0$ to FM $J_{int} < 0$) at the bond angle of $160°$.

The Heisenberg model energies were computed for all 2^p spin configurations in each supercell.

The lowest energy ordering found in this larger set of configurations is still the FeAFMMnFM ordering, with FM alignment of the Mn and AFM antialignment of the Fe along the Mn and Fe pillars, respectively, and alternating FM and AFM xy layers as in Fig. 4.3. The lowest-energy alternative magnetic state is a state in which one Mn per supercell in the FM xy layer flips, at an energy cost of 6.3 meV/supercell. The net magnetization for the resulting state decreases from $M_{GS} = 3.8\mu_B$ per one Fe-Mn pair to $\frac{p-2}{p}M_{GS}$.

Within a mean field approximation with four effective fields, two for the two Fe atoms and two for the two Mn atoms in the unit cell of the BiFeO$_3$-BiMnO$_3$ nanocheckerboard, the magnetic transition temperature of the BiFeO$_3$-BiMnO$_3$ nanocheckerboard is $T_c = 406K$. This temperature is intermediate between the Neel temperature, $T_N^{exp} = 643$ K, of bulk BiFeO$_3$ and the Curie temperature, $T_c^{exp} = 105$ K, of bulk BiMnO$_3$ [64, 75–78].

4.6 Alternative Structures of the BiFeO$_3$-BiMnO$_3$ Nanocheckerboard
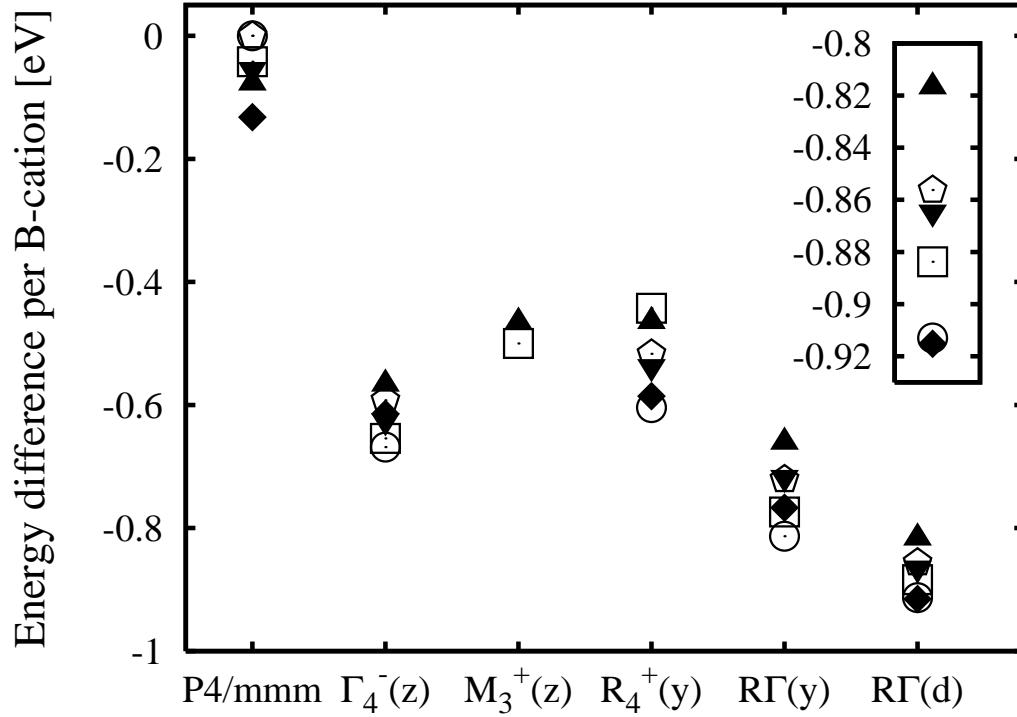
Figure 4.12: Structural energetics of BiFeO$_3$-BiMnO$_3$ nanocheckerboard. Energy difference per perovskite cell (per B-cation) for different magnetic orderings (see Fig. 4.3) and for structural distortions (see Fig. 1.4 and Table 4.1). Inset: zoomed view of the magnetic energies for the c-R3c structure. FeAFMMnFM ordering (filled diamond) competes with G-AFM ordering (open circle) in the nanocheckerboard alternative structures.

The energies for various magnetic orderings and structural distortions of the nanocheckerboard are shown in in Fig. 4.12. The structural parameters for each structure type are relaxed for each magnetic ordering. The most energetically favorable alternative structures, like the ground state FeAFMMnFM c-R3c structure, are polar and include oxygen octahedra rotations.

The polar distortion in the alternative structures of the nanocheckerboard is quantified by the value of the polarization computed using nominal charges (Eq. (4.2)), that can be directly compared with nominal-charge polarizations in the structures of BiFeO$_3$ (cf. Tables 4.2 and 4.6). As in BiFeO$_3$, there is a low-lying supertetragonal P4mm phase, with $c/a \sim 1.3$ and very large spontaneous polarization. For the various structures considered, the polarization tends to decrease as

Table 4.6: Low energy alternative and ground state (GS) structure of $BiFeO_3$-$BiMnO_3$ nanocheckerboard. Energy difference $\Delta E[eV/B - cation]$ is calculated for different magnetic orderings with respect to FeAFMMnAFM P4/mmm structure [as in Fig. 4.12]. Insulating DOS band gap Δ (or metallic m character), polarization P estimated from the nominal charges [Eq. (4.2)], the in-plane a and out-of-plane c lattice constants [see perovskite cell in Fig. 4.1], and oxygen-octahedron rotation angle Θ are given for the lowest-energy magnetic ordering corresponding to each structural distortion.

Space group	P4/mmm	c-P4mm	c-I4cm	c-R3c
Modes	-	$\Gamma_4^-(z)$	$R_4^+,\Gamma_4^-(y)$	$R_4^+,\Gamma_4^-([111])$
Mag. order	FeAFMMnFM	G-AFM	G-AFM	FeAFMMnFM
Δ [eV]	m	1.01	1.55	0.90
P $[\mu C/cm^2]$	-	101.9	71.5	57.9
a/ c [Å]	3.81/ 3.88	3.66/ 4.60	5.80/ 3.67	5.50/ 3.93
$\Theta[°]$	-	-	4.8	7.2-20.3
ΔE (FeAFMMnFM)	-0.132	-0.615	-0.767	-0.915
ΔE (G-AFM)	0.000	-0.668	-0.813	-0.913
ΔE (C-FIM)	-0.042	-0.654	-0.774	-0.884
ΔE (FeFMMnAFM)	-0.054	-0.625	-0.717	-0.865
ΔE (FeAFMMnAFM)	0.000	-0.592	-0.721	-0.856
ΔE (FM)	-0.077	-0.567	-0.661	-0.817

rotational distortion is introduced, with the smallest value found in the c-R3c structure.

In the P4/mmm structure, the nanocheckerboard is metallic, while a band gap opens with either polar or rotational distortion. This behavior is similar to that of $BiMnO_3$ and $BiFeO_3$, which are metallic in the FM Pm$\bar{3}$m, or P4/mmm structures with a band gap opened and/or widened by distortion (in FM $BiMnO_3$, only in the spin-down channel).

As can be seen in Fig. 4.12, the difference in energies between different structure types is generally much larger than the difference in magnetic energies for a given structure type. The interesting feature of this figure is that the favored magnetic ordering is different for different structure types, switching between ferrimagnetic FeAFMMnFM and antiferromagnetic G-AFM. This is in contrast to the case of bulk $BiFeO_3$ (see Fig. 4.5), or bulk $BiMnO_3$ (see Fig. 4.7), in which the favored magnetic ordering does not change for different structure types.

4.7 Magnetic and Structural Transitions Driven by Anisotropic Strain

The sensitivity of the magnetic exchange couplings to the structure should produce changes in the magnetic ordering energies for perturbations that couple to the crystal structure, such as electric field, pressure and epitaxial strain. It is even possible that a structural perturbation could drive the system through a magnetic transition into an alternative low-energy ordering. Furthermore, the fact that in the nanocheckerboard the favored magnetic ordering is different for different structure types, discussed in the previous section, suggests that the magnetic ordering of the system could in principle be changed by a perturbation that changes the structure type, producing a novel magnetic-coupling response at the magnetic-structural phase boundary [200, 90]. For example, it might be possible to drive the nanocheckerboard from its ferrimagnetic FeAFMMnFM c-R3c GS with a nonzero magnetization to a G-AFM c-I4cm state with zero magnetization.

We have explored this possibility for two types of epitaxial strain. First, we investigated the c-R3c phase with an isotropic epitaxial strain, corresponding to an (110) matching plane. Thus, the second and third lattice vectors of the $\sqrt{2}a \times \sqrt{2}a \times 2c$ supercell, along [-110] and along [001], are constrained to be perpendicular with uniform scaling of the lattice constants $a = (1+s)a_0$ and $c = (1+s)c_0$, where $a_0 = 5.50\text{Å}$ and $c_0 = 3.93\text{Å}$ are the unstrained lattice constants of FeAFMMnFM c-R3c GS. In this case, there is no magnetic transition: the system remains FeAFMMnFM from $s = 0\%$ up to strain of 10%.

Second, we considered an anisotropic epitaxial strain, corresponding to a (001) matching plane, such that the lattice constant along [110] is fixed to $\sqrt{2} \times a_0 = 5.52\text{Å}$, while the lattice constant a along [-110] is elongated, with strain defined as $\frac{a-a_0}{a_0}$. $a_0 = 3.9\text{Å}$ is chosen as it is the lattice constant of an ideal perovskite cell with volume which is the average of that of bulk R3c BiFeO$_3$ ($V_{BFO} = 59.28\text{Å}^3/B-cation$) and bulk C2/c [71, 72] BiMnO$_3$ ($V_{BMO} = 59.41\text{Å}^3/B-cation$).

The anisotropic epitaxial strain dependence of the energies of the c-R3c and c-I4m structures is presented in Fig. 4.13. At 0% strain, the energy difference between FeAFMMnFM to G-AFM
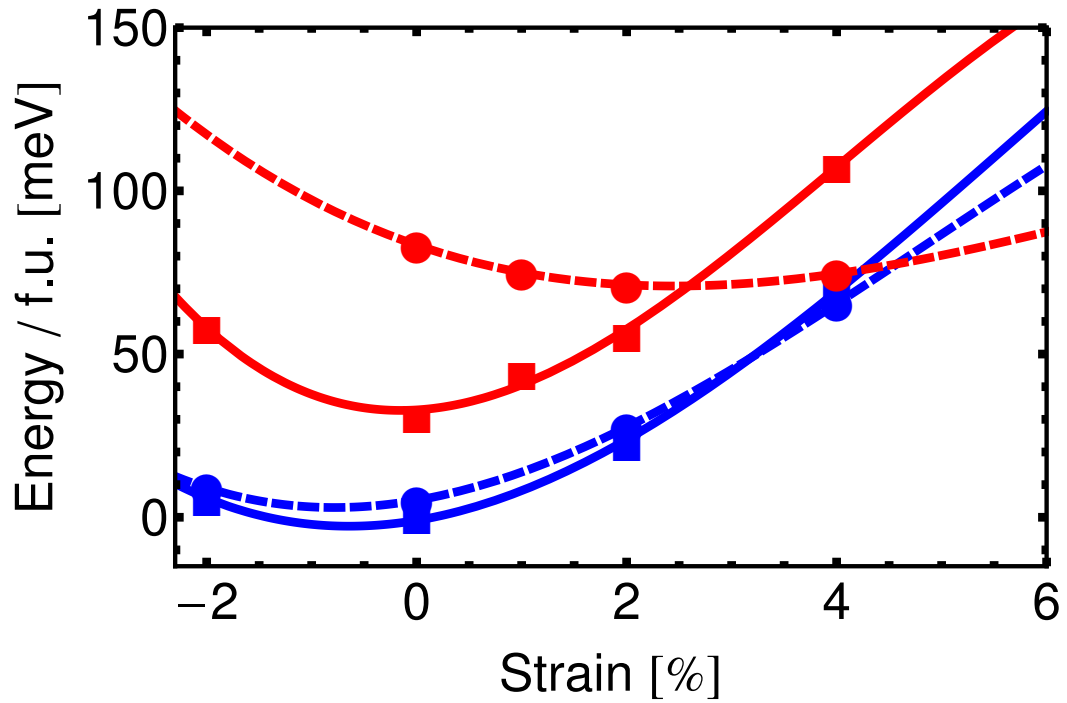
Figure 4.13: Epitaxial-strain-driven magnetic transition in BiFeO$_3$-BiMnO$_3$ nanocheckerboard. Total energies of the FeAFMMnFM (solid) and G-AFM (dashed line) magnetic orderings in the c-R3c structure type (blue) and c-I4cm structure type (red), as a function of anisotropic in-plane tensile strain (details in the text).

in the c-R3c structure is 5 meV/B-cation; this differs slightly from the value for the relaxed structures reported in Table 4.6 due to the difference in lattice constants between the epitaxial constrained structure and the fully relaxed structure (the corresponding energy difference at 0% strain for c-I4cm is greater because the difference in lattice constants is greater). At 3% strain, there is a magnetic transition from ferrimagnetic FeAFMMnFM to this low-lying G-AFM phase, while the structure remains c-R3c. This arises from the modification of the exchange couplings by the structural changes produced by the changing epitaxial strain.

With a further increase in strain, there is a transition from c-R3c to a c-I4cm phase at about 4.5%. Since the favored magnetic ordering is G-AFM in both structural phases, no magnetic transition accompanies the structural transition. However, this result does illustrate the feasibility of a epitaxial-strain-induced structural transition from one pattern of rotational distortions to another in

Table 4.7: Calculated total magnetic energies E [eV/B-cation] and energy differences ΔE [eV/B-cation] in an ideal perovskite structure with lattice constant $a_0 = 3.839\mathring{A}$ for various magnetic states in the checkerboard, rocksalt (oxygens are relaxed to accomodate their preferable positions), and layered superlattice of $BiFeO_3$-$BiMnO_3$. The checkerboard ordering shows a quasidegenerate spectrum of magnetic energies, whereas the rocksalt and layered superlattice show larger gaps between the ground state (GS) and the first alternative magnetic state. Values of $U_{Fe} = U_{Mn} = 5eV$ and $J_{Fe} = J_{Mn} = 1eV$ are used in the upper, while values of $U_{Fe}^{eff} = 4eV$, $U_{Mn}^{eff} = 5.2eV$ with $U^{eff} = U - J$ are used in the lower panel of the table, respectively (see Sec. 4.2).

Checkerboard Magnetic State	E	Rocksalt Superlattice Magnetic State	E	Layered Superlattice Magnetic State	E
FeAFMMnFM	-35.04	FMFM	-35.06	FeAFMMnFM	-35.11
	ΔE		ΔE		ΔE
FeAFMMnFM	0.000	FMFM	0.000	FeAFMMnFM	0.000
FM	0.022	FeAFMMnFM	0.044	FM	0.111
C-FIM	0.076	FeFMMnAFM	0.045	FeAFMMnAFM	0.135
FeAFMMnAFM	0.081	FM	0.065	FeFMMnFM	0.136
G-AFM	0.114	AFMAFM	0.101	G-AFM	0.181
FeFMMnAFM	0.119	G-AFM	0.114	FeFMMnAFM	0.260
	E		E		E
FeAFMMnFM	-34.68	FMFM	-34.66	FeAFMMnFM	-34.76
	ΔE		ΔE		ΔE
FeAFMMnFM	0.000	FMFM	0.000	FeAFMMnFM	0.000
FM	0.028	FM	0.047	FM	0.097
FeAFMMnAFM	0.084	FeFMMnAFM	0.055	FeAFMMnAFM	0.137
C-FIM	0.113	FeAFMMnFM	0.070	FeFMMnFM	0.143
FeFMMnAFM	0.129	G-AFM	0.079	G-AFM	0.219
G-AFM	0.152	AFMAFM	0.084	FeFMMnAFM	0.257

this system; a coupled structural-magnetic phase boundary thus may be brought to light by future exploration of various epitaxial strain constraints.

4.8 Role of the B-Site Cation Ordering in Magnetostructural Effect

Quasidegenerate magnetic states in the $BiFeO_3$-$BiMnO_3$ nanocheckerboard are a necessary ingredient for the observed magnetostructural effect (cf. Fig. 4.12 and Table 4.6), where change in the magnetic ordering is achieved by a perturbation (e.g., epitaxial strain, as in Sec. 4.7]). Here, we investigate the role of the cation-ordering geometry in determining the spectrum of magnetic states; in particular, this will show whether the quasidenerature spectrum is unique to the checkerboard

geometry.

Magnetic energies are computed in the ideal perovskite structure of five systems: the bulk parent $BiFeO_3$ and $BiMnO_3$, the $BiFeO_3$-$BiMnO_3$ nanocheckerboard, the $BiFeO_3$-$BiMnO_3$ layered (001) superlattice, and the $BiFeO_3$-$BiMnO_3$ rocksalt structure with Fe and Mn alternating in every other unit cell ((111) superlattice). The results for the checkerboard, the rocksalt, and the layered superlattice are presented in Table 4.7. Bulk $BiFeO_3$ and bulk $BiMnO_3$ exhibit behavior similar to the (001) layered superlattice [90]. In these three systems, the difference in energy between the magnetic ground state (G-AFM in bulk $BiFeO_3$, FM in bulk $BiMnO_3$, and FeAFMMnFM in the (001) layered superlattice) and the first alternative state is in the range $0.10 - 0.14 eV/B - cation$. This spectral gap is sufficiently large that structural changes cannot lower the energy of an alternative state below that of the original magnetic ground state.

Indeed, for all structures considered the lowest magnetic state in bulk $BiFeO_3$ and bulk $BiMnO_3$ is G-AFM and FM, respectively (see Figs. 4.5, 4.7). In the (001) superlattice, we calculate magnetic energies for the G-AFM and FeAFMMnFM magnetic states in two structural distortions: For l-I4cm (see Table 4.1), we find $\Delta E = -0.504 eV/B - cation$ for G-AFM and $\Delta E = -0.553 eV/B - cation$ for FeAFMMnFM with respect to the FeAFMMnFM magnetic state in the ideal perovskite cell (see Table 4.7). For l-R3c, we find $\Delta E = -0.752 eV/B - cation$ for G-AFM and $\Delta E = -0.761 eV/B - cation$ for FeAFMMnFM. For both structural distortions considered, the lowest energy magnetic ordering is FeAFMMnFM.

In contrast, all magnetic states in the nanocheckerboard are quasidegenerate, all are lower in energy than the lowest-energy states in the (001) superlattice and the bulk. The rocksalt structure is an intermediate case: while the difference between the FMFM magnetic ground state and the first alternative state is $0.05 eV/B - cation$, close to half of the spectral gap of the (001) superlattice and bulk, all the states considered fall in the same low-energy window as for the checkerboard. Therefore it is much more likely that a structurally-driven transition between the different magnetic states could occur in the checkerboard, or in the rocksalt structure, than in the other geometries studied here.

The importance of the B-site cation geometry in the magnetic ordering energy spectrum can be qualitatively understood from a simple Heisenberg model of the form given in Eq. (4.4), where we assume that the exchange couplings J_{Fe}, J_{Mn} and J_{int} are independent of cation geometry, thus being transferable from one geometry to the other. We can approximately reproduce the magnetic ordering energies in the ideal perovskite structure of the checkerboard with the Mn-Mn interaction J_{Mn} being strongly FM, the Fe-Fe interaction J_{Fe} being AFM and about half the strength, and the Fe-Mn interaction J_{int} being weakly FM. Assuming the same values in the FeAFMMnFM GS of the (001) layered superlattice, the high and medium-strength bonds are all satisfied (happy in the language of frustrated magnetism) and the only unhappy bonds are weak bonds between the Mn and the opposite spin Fe in the adjacent layer (one bond per B cation). Thus this state is energetically clearly preferred over other orderings considered, which all involve a significant fraction of unhappy high and/or medium strength bonds, thus opening the observed gap in the magnetic energy spectrum. In contrast, in the checkerboard, the total fraction of high and medium-strength bonds is half that in the layered superlattice, and the alternative states are low in energy as they involve tradeoffs between a larger number of happy weak bonds and a smaller number of unhappy medium or high-strength bonds. Finally, in the rocksalt structure, all the nearest neighbor bonds are weak. This is consistent with the fact that all orderings considered are at low energies. However, a simple one-parameter model does not correctly account for the energetic order of the states in this range or the gap between the ground state ordering and the first alternative state, which would require a model including next-nearest neighbor interactions.

Indeed, the assumption of exact transferability used above is only semi-quantitatively valid. In particular, changes in B-site cation geometry result in relative energy shifts of the Fe, Mn and O states and changes in the orbital wavefunctions, and thus in changes to the wavefunction overlaps and energy denominators that contribute to superexchange. This leads to different values of the magnetic couplings J_{Fe}, J_{Mn}, or J_{int} in the various geometries considered (cf. Table 4.7). In addition, structural distortions modify these magnetic couplings, as would be needed to explain the difference in the ordering of the magnetic energies in Tables 4.6 and 4.7. However, the simple model

does serve to give useful insight into this complex issue, and highlights the fact that the magnetic ordering spectrum is indeed very sensitive to the B-site cation arrangement.

4.9 Discussion

The experimental realization of the $BiFeO_3$-$BiMnO_3$ nanocheckerboard would be challenging as its formation energy is positive: the combined total energies of R3c G-AFM ground state of bulk $BiFeO_3$ ($E[BFO] = -35.079eV/B - cation$) and of the R3c FM lowest energy structure of bulk $BiMnO_3$ ($E[BMO] = -36.676eV/B - cation$) are lower than that of the c-R3c FeAFMM-nFM ground state of the $BiFeO_3$-$BiMnO_3$ nanocheckerboard ($E[BFMO] = -71.694eV/2B - cations$). Though the $BiFeO_3$-$BiMnO_3$ nanocheckerboard is at best metastable, there is indication from experiments that fabrication of the $BiFeO_3$-$BiMnO_3$ nanocheckerboard with square sizes on the order of a unit cell would not be impossible with appropriate tuning of growth parameters. Growth of (001) $BiMnO_3$ on $BiFeO_3$ films has recently been reported. In this study post-annealing led to intermixing of the Fe and Mn, with a concomitant increase in ferromagnetic T_c [228]. This experiment provides support for the first-principles observation that magnetic ordering in this system is very sensitive to the B-site cation arrangement. With regard to other film orientations, (110) and (111) as well as (001) $BiFeO_3$ films have been successfully grown on oriented $SrTiO_3$ substrates [55, 229]. For $BiMnO_3$, (111) and (001) oriented films have been grown with substrate vicinality [74, 230]. There should be no fundamental obstacle to analgous growth of (110) oriented films of $BiMnO_3$. More generally, a combination of patterned substration, possible masking, layer-by-layer growth, and carefully tuned growth parameters could influence the deposition process enough to produce a checkerboard structure of $BiFeO_3$-$BiMnO_3$.

In order to make better contact with future experiment, it is useful to consider magnetic ordering of larger-scale n×n $BiFeO_3$-$BiMnO_3$ checkerboards, where the lateral dimension of the $BiFeO_3$ and $BiMnO_3$ pillars is n perovskite lattice constants. Within each pillar, $BiFeO_3$ and $BiMnO_3$ regions should be G-AFM and FM respectively, since this ordering is the most energetically favorable in the parent bulk structures. This is true even in the extreme case of n=1 discussed in Sec. 4.5. The

magnetic coupling constants J_{Fe}, J_{Mn} and J_{int} (Eq. (4.5)), obtained in Sec. 4.5.2 would allow the construction of Heisenberg models to explore the magnetic ordering of these larger-scale checkerboards with the ideal perovskite structure, where J_{Fe} and J_{Mn} connecting two atoms in the xy plane can be taken to be equal to the coupling along the pillar, but we have not pursued this farther here. Generally speaking, we expect that the possibility of a structurally-driven magnetic transition should decrease as the lateral size of the $BiFeO_3$ and $BiMnO_3$ pillars increases and the interface effects (Fe-Mn interactions) become less important.

On a technical note, the robustness of our calculated first-principles results has been checked by using two different implementations of LSDA+U with different parametrizations to compute magnetic ordering energies in the ideal perovskite structure for the checkerboard, the rocksalt cation ordering, and the layered superlattice (Table VI). The key results are the same for both implementations: the type of ground state magnetic ordering for each cation arrangement, the quasidegeneracy of the spectrum of magnetic energies in the checkerboard, the gap in the energy spectrum in the layered (001) superlattice, and the intermediate character of the rocksalt ordering.

Finally we remark that our first principles calculations do not include spin-orbit coupling (SOC) that is known to lead to weak ferromagnetism in $BiFeO_3$ [67]. Since the $BiFeO_3$-$BiMnO_3$ nanocheckerboard already has a ferrimagnetic ground state without SOC, inclusion of SOC may result in a slightly changed value of the total magnetization and to small canting angles of the Fe and Mn spins; these changes should not fundamentally affect the results presented here. The addition of SOC to our present calculations is certainly worth pursuing in future work.

4.10 Summary

In this chapter, the structure and properties of an atomic-scale $BiFeO_3$-$BiMnO_3$ checkerboard were investigated using first-principles calculations and magnetic modeling. This unusual heterostructure was found to have properties distinct from those of its bulk parent constituents, or those of (001) superlattices of these two materials. We attribute this behavior to the magnetic frustration resulting from its B-site cation geometry; this leads to a quasidegenerate manifold of magnetic states that can

be switched through small applied external perturbations, resulting in an unusual magnetostructural effect. The possibility of realizing this system in the laboratory was discussed. This study of a two-component nanocheckerboard should be considered as a proof-of-principle example, and we plan to study similar geometries on longer length scales to facilitate contact with future experiments.

Bibliography

[1] J. Valasek, *Phys. Rev.* **17**, 475 (1921).

[2] W. P. Mason, *Phys. Rev.* **69**, 173 (1946).

[3] R. E. Newnham and L. E. Cross, *MRS Bulletin* **30**, 845 (2005).

[4] H. Mueller, *Phys. Rev.* **47**, 175 (1935).

[5] W. P. Mason, *Phys. Rev.* **74**, 1134 (1948).

[6] W. P. Mason and B. T. Matthias, *Phys. Rev.* **74**, 1622 (1948).

[7] A. von Hippel, *Rev. Mod. Phys.* **22**, 221 (1950).

[8] S. Roberts, *Phys. Rev.* **71**, 890 (1947).

[9] B. Matthias and A. von Hippel, *Phys. Rev.* **73**, 1378 (1948).

[10] W. Cochran, *Phys. Rev. Lett.* **3**, 412 (1959).

[11] G. Rupprecht and R. O. Bell, *Phys. Rev.* **135**, A748 (1964).

[12] L. D. Landau and E. M. Lifshitz, *Statistical Physics 3rd Edition Part 1* (Elsevier Science, 1980).

[13] P. Chandra and P. B. Littlewood, *Physics of Ferroelectrics: a Modern Perspective* (Springer-Verlag, Berlin, 2007, pp. 69-115).

[14] K. J. Choi, M. Biegalski, Y. L. Li, A. Sharan, J. Schubert, R. Uecker, P. Reiche, Y. B. Chen, X. Q. Pan, V. Gopalan, L.-Q. Chen, D. G. Schlom and C. B. Eom, *Science* **306**, 1005 (2004).

[15] J.H. Haeni, P. Irvin, W. Chang, R. Uecker, P. Reiche, Y. L. Li, S. Choudhury, W. Tian, M. E. Hawley, B. Craigo, A. K. Tagantsev, X. Q. Pan, S. K. Streiffer, L. Q. Chen, S. W. Kirchoefer, J. Levy and D. G. Schlom, *Nature* **430**, 758 (2004).

[16] A. Ohtomo, D. A. Muller, J. L. Grazul and H. Y. Hwang, *Nature* **419**, 378 (2002).

[17] J. B. Neaton and K. M. Rabe, *Appl. Phys. Lett.* **82**, 1586 (2003).

[18] C. H. Ahn, K. M. Rabe and J.-M. Triscone, *Science* **303**, 488 (2004).

[19] C. Bungaro and K. M. Rabe, *Phys. Rev. B* **69**, 184101 (2004).

[20] D. D. Fong, G. B. Stephenson, S. K. Streiffer, J. A. Eastman, O. Auciello, P. H. Fuoss, C. Thompson, A. Ohtomo, D. A. Muller, J. L. Grazul and H. Y. Hwang, *Science* **304**, 1650 (2004).

[21] K. Johnston, X. Huang, J. B. Neaton and K. M. Rabe, *Phys. Rev. B* **71**, 100103(R) (2005).

[22] M. Dawber, K. M. Rabe and J. F. Scott, *Rev. Mod. Phys.* **77**, 1083 (2005).

[23] K. M. Rabe, *Current Opinion in Solid State and Materials Science* **9**, 122 (2005).

[24] M. Dawber, C. Lichtensteiger, M. Cantoni, M. Veithen, P. Ghosez, K. Johnston, K. M. Rabe and J.-M. Triscone, *Phys. Rev. Lett.* **95**, 177601 (2005).

[25] H. N. Lee, H. M. Christen, M. F. Chisholm, C. M. Rouleau and D. H. Lowndes, *Nature* **433**, 395 (2005).

[26] S. M. Nakhmanson, K. M. Rabe and D. Vanderbilt, *Phys. Rev. B* **73**, 060101 (R) (2006).

[27] O. Auciello, J. F. Scott and R. Ramesh, *Physics Today* **51**, 22 (1998).

[28] J. F. Scott, *Ferroelectric Memories* (Springer, Berlin, 2000).

[29] M. Dawber, P. Chandra, P. B. Littlewood and J. F. Scott, *J. Phys.: Cond. Mat.* **15**, L393 (2003).

[30] E. L. Venturini, G. A. Samara, M. Itoh and R. Wang, *Phys. Rev. B* **69**, 184105 (2004).

[31] P. Coleman, *Physica B* **378-380**, 1160 (2006).

[32] S. E. Rowley, L. J. Spalek, R. P. Smith, M. P. M. Dean, G. G. Lonzarich, J. F. Scott and S. S. Saxena, arXiv:0903.1445v1; S. E. Rowley and S. S. Saxena (private communication).

[33] N. A. Spaldin, *Physics of Ferroelectrics: a Modern Perspective* (Springer-Verlag, Berlin, 2007, pp. 175-217).

[34] J. F. Scott, *Nature Materials* **6**, 256 (2007).

[35] M. Mostovoy, *Phys. Rev. Lett.* **96**, 067601 (2006).

[36] N. A. Hill, *J. Phys. Chem. B* **104**, 6694 (2000).

[37] C.-W. Nan, M. I. Bichurin, S. Dong, D. Viehland and G. Srinivasan, *J. Appl. Phys.* **103**, 031101 (2008).

[38] K. M. Rabe, M. Dawber, C. Lichtensteiger, C. H. Ahn and J.-M. Triscone, *Physics of Ferroelectrics: a Modern Perspective* (Springer-Verlag, Berlin, 2007, pp. 1-30).

[39] R. D. King-Smith and D. Vanderbilt, *Phys. Rev. B* **47**, 1651 (1993).

[40] R. Resta and D. Vanderbilt, *Physics of Ferroelectrics: a Modern Perspective* (Springer-Verlag, Berlin, 2007, pp. 31-68).

[41] N. A. Spaldin and M. Fiebig, *Science* **309**, 391 (2005).

[42] H. T. Stokes, E. H. Kisi, D. M. Hatch and C. J. Howard, *Acta Cryst. B* **B58**, 934 (2002).

[43] K. A. Muller and H. Burkard, *Phys. Rev. B* **19**, 3593 (1979).

[44] W. Zhong and D. Vanderbilt, *Phys. Rev. Lett.* **74**, 2587 (1995).

[45] W. Zhong and D. Vanderbilt, *Phys. Rev. B* **53**, 5047 (1996).

[46] N. Sai and D. Vanderbilt, *Phys. Rev. B* **62**, 13942 (2000).

[47] P. A. Fleury, J. F. Scott and J. M. Worlock, *Phys. Rev. Lett.* **21**, 16 (1968).

[48] G. A. Samara and B. Morosin, *Phys. Rev. B* **8**, 1256 (1973).

[49] A. R. Akbarzadeh, L. Bellaiche, K. Leung, J. Iniguez and D. Vanderbilt, *Phys. Rev. B* **70**, 054103 (2004).

[50] C. Ménoret, J. M. Kiat, B. Dkhil, M. Dunlop, H. Dammak and O. Hernandez, *Phys. Rev. B* **65**, 224104 (2002).

[51] R. Ramesh and N. A. Spaldin, *Nature Mater.* **6**, 21 (2007).

[52] V. V. Shvartsman, W. Kleemann, R. Haumont and J. Kreisel, *Appl. Phys. Lett.* **90**, 172115 (2007).

[53] D. Lebeugle, D. Colson, A. Forget, M. Viret, P. Bonville, J. F. Marucco and S. Fusil, *Phys. Rev. B* **76**, 024116 (2007).

[54] J. Wang, J. B. Neaton, H. Zheng, V. Nagarajan, S. B. Ogale, B. Liu, D. Viehland, V. Vaithyanathan, D. G. Schlom, U. V. Waghmare, N. A. Spaldin, K. M. Rabe, M. Wuttig and R. Ramesh, *Science* **299**, 1719 (2003).

[55] J. Li, J. Wang, M. Wuttig, R. Ramesh, N. Wang, B. Ruette, A. P. Pyatakov, A. K. Zvezdin and D. Viehland, *Appl. Phys. Lett.* **84**, 5261 (2004).

[56] J. B. Neaton, C. Ederer, U. V. Waghmare, N. A. Spaldin and K. M. Rabe, *Phys. Rev. B* **71**, 014113 (2005).

[57] P. Baettig, R. Seshadri and N. A. Spaldin, *J. Am. Chem. Soc.* **129**, 9854 (2007).

[58] D. C. Arnold, K. S. Knight, F. D. Morrison and P. Lightfoot, *Phys. Rev. Lett.* **102**, 027602 (2009).

[59] P. Ravindran, R. Vidya, A. Kjekshus, H. Fjellvag and O. Eriksson, *Phys. Rev. B* **74**, 224412 (2006).

[60] D. Kan, L. Pálová, V. Anbusathaiah, C. J. Cheng, S. Fujino, V. Nagarajan, K. M. Rabe and I. Takeuchi, *Adv. Mater.* **20**, 1 (2010).

[61] I. Levin, S. Karimi, V. Provenzano, C. L. Dennis, H. Wu, T. P. Comyn, T. J. Stevenson, R. I. Smith and I. M. Reaney, *Phys. Rev. B* **81**, 020103(R) (2010).

[62] C.-J. Cheng, D. Kan, S.-H. Lim, W. R. McKenzie, P. R. Munroe, L. G. Salamanca-Riba, R. L. Withers, I. Takeuchi and V. Nagarajan, *Phys. Rev. B* **80**, 014109 (2009).

[63] I. Sosnowska, T. Peterlin-Neumaier and E. Streichele, *J. Phys. C* **15**, 4835 (1982).

[64] S. V. Kiselev, R. P. Ozerov and G. S. Zhdanov, *Sov. Phys. Dokl.* **7**, 742 (1963).

[65] I. E. Dzyaloshinskii, *Sov. Phys. JETP* **5**, 1259 (1957).

[66] T. Moriya, *Phys. Rev.* **120**, 91 (1960).

[67] C. Ederer and N. A. Spaldin, *Phys. Rev. B* **71**, 060401(R) (2005).

[68] S.-W. Cheong and M. Mostovoy, *Nature Mat.* **6**, 13 (2007).

[69] R. Seshadri and N. A. Hill, *Chem. Mater.* **13**, 2892 (2001).

[70] A. M. dos Santos, A. K. Cheetham, T. Atou, Y. Syono, Y. Yamaguchi, K. Ohoyama, H. Chiba and C. N. R. Rao, *Phys. Rev. B* **66**, 064425 (2002).

[71] A. A. Belik, S. Iikubo, K. Kodama, N. Igawa, S. Shamoto, M. Maie, T. Nagai, Y. Matsui, S. Y. Stefanovich, B. I. Lazoryak and E. Takayama-Muromachi, *J. Am. Chem. Soc.* **128**, 706 (2006).

[72] A.A. Belik, S. Iikubo, T. Yokosawa, K. Kodama, N. Igawa, S. Shamoto, M. Azuma, M. Takano, K. Kimoto, Y. Matsui and E. Takayama-Muromachi, *J. Am. Chem. Soc.* **129**, 971 (2007).

[73] A. M. dos Santos, S. Parashar, A. R. Raju, Y. S. Zhao, A. K. Cheetham and C. N. R. Rao, *Solid State Commun.* **122**, 49 (2002).

[74] A. Sharan, J. Lettieri, Y. Jia, W. Tian, X. Pan, D. G. Schlom and V. Gopalan, *Phys. Rev. B* **69**, 214109 (2004).

[75] H. Chiba, T. Atou and Y. Syono, Hole-Doping Effect on Ferromagnetic Perovskite $BiMnO_3$", *J. Solid State Chem.* **132**, 139 (1997).

[76] F. Sugawara, S. Iida, Y. Syono and S. Akimoto, *J. Phys. Soc. Jap.* **20**, 1529 (1965).

[77] F. Sugawara, S. Iiida, Y. Syono and S. Akimoto, *J. Phys. Soc. Jap.* **25**, 1553 (1968).

[78] H. Faqir, H. Chiba, M. Kikuchi, Y. Syono, M. Mansori, P. Satre and A. Sebaoun, *J. Solid State Chem.* **142**, 113 (1999).

[79] C. Kittel, *Introduction to Solid State Physics, Eight Edition*, pp. 323–360, (J. Wiley & Sons, Inc., USA, 2005).

[80] H. P. Sun, W. Tian, X. Q. Pan, J. H. Hanei and D. G. Schlom, *Appl. Phys. Lett.* **84**, 3298 (2004).

[81] G. Catalan, L. J. Sinnamon and J. M. Gregg, *J. Phys. Condens. Mat.* **16**, 2253 (2004); G. Catalan, B. Noheda, J. McAneney, L. J. Sinnamon and J. M. Gregg, Phys. Rev. B **72**, 020102 (2005).

[82] W. Ma and L. E. Cross, *Appl. Phys. Lett.* **78**, 2920 (2001); *ibid* **79**, 4420 (2001); *ibid* **81**, 3440 (2002); *ibid* **82**, 3293 (2003).

[83] T. Ishidate, S. Abe, H. Takahashi and N. Mori, *Phys. Rev. Lett.* **78**, 2397 (1997).

[84] R. Wang and M. Itoh, strontium titanate," *Phys. Rev. B* **64**, 174104 (2001).

[85] E. Kaxiras, *Atomic and Electronic Structure of Solids* (Cambridge University Press, Cambridge, 2003).

[86] G. Kresse and J. Hafner, *Phys. Rev. B* **47**, R558 (1993).

[87] G. Kresse and J. Furthmuller, *Phys. Rev. B* **54**, 11169 (1996).

[88] N. Sai, B. Meyer and D. Vanderbilt, *Phys. Rev. Lett.* **84**, 5636 (2000).

[89] S. M. Nakhmanson, K. M. Rabe and D. Vanderbilt, *Appl. Phys. Lett.* **87**, 102906 (2005).

[90] L. Pálová, P. Chandra and K. M. Rabe, *Phys. Rev. Lett.* **104**, 037202 (2010).

[91] M. E. Lines and A. M. Glass, *Principles and Applications of Ferroelectrics and Related Materials* (Clarendon Press, Oxford, 1977).

[92] N. A. Pertsev, A. G. Zembilgotov and A. K. Tagantsev, Phys. Rev. Lett. **80**, 1988 (1998).

[93] D. Balzar, P. A. Ramakrishnan and A. M. Hermann, *Phys. Rev. B* **70**, 092103 (2004).

[94] S. P. Alpay, I. B. Misirlioglu, V. Nagarajan and R. Ramesh, *Appl. Phys. Lett.* **8**5 2044 (2004); V. Nagarajan, C. L. Jia, H. Kohlstedt, R. Waser, I. B. Misirlioglu, S. P. Alpay and R. Ramesh, *Appl. Phys. Lett.* **8**6 192910 (2005).

[95] A. M. Bratkovsky and A. P. Levanyuk, *Phys. Rev. Lett.* **9**4, 107601 (2005).

[96] T. Suzuki, Y. Nishi and M. Fujimoto *Philos. Mag. A* **79**, 2461 (1999).

[97] V. Nagarajan, C. L. Jia, H. Kohlstedt, R. Waser, I. B. Misirlioglu and S. P. Alpay, *Appl. Phys. Lett.* **8**6, 192910 (2005).

[98] A. Gruverman, B. J. Rodriguez, A. I. Kingdon, R. J. Nemanich, A. K. Tagantsev, J. S. Cross and M. Tsukada, *Appl. Phys. Lett.* **8**3, 728 (2003).

[99] A. K. Tagantsev, *Sov. Phys. JETP* **6**1, 1246 (1985); *Phys. Rev. B* **3**4, 5883 (1986).

[100] J. S. Speck and W. Pompe, *J. Appl. Phys.***7**6, 466 (1994).

[101] O. Vendik and S. P. Zubko *J. Appl. Phys.* **88**, 5343 (2000).

[102] C. H. Ahn, T. Tybell, L. Antognazza, K. Char, R. H. Hammond, M. R. Beasley, O. Fischer and J.-M. Triscone, *Science* **276**, 1100 (1997).

[103] T. M. Shaw, Z. Suo, M. Huang, E. Liniger, R. B. Laibowitz and J. D. Baniecki, *Appl. Phys. Lett* **75**, 2129 (1999).

[104] P. Paruch, T. Tybell and J.-M. Triscone, *Appl. Phys. Lett.* **79**, 530 (2001).

[105] C. B. Parker, J.-P. Maria and A. I. Kingon, *Appl. Phys. Lett.* **81**, 340 (2002).

[106] L. J. Sinnamon, R. M. Bowman and J. M. Gregg, Appl. Phys. Lett. **81**, 889 (2002).

[107] A. Lookman, R. M. Bowman, J. M. Gregg, J. Kut, S. Rios, M. Dawber, A. Ruediger and J. F. Scott, *J. Appl. Phys.* **96**, 555 (2004).

[108] M. M. Saad, P. Baxter, R. M. Bowman, J. M. Gregg, F. D. Morrison and J. F. Scott, *J. Phys: Cond. Mat.* **16**, L451 (2004).

[109] H. J. Kim, S. Oh and H. M. Jang, *Appl. Phys. Lett.* **75**, 3195 (1999).

[110] S. Rios, A. Ruedinger, A. Q. Jiang, J. F. Scott, H. Lu and Z. Chen, *J. Phys. Cond. Mat.* **15**, L305 (2003).

[111] R. R. Mehta, B. Silverman and J. T. Jacobs, *J. Appl. Phys.* **44**, 3379 (1973).

[112] R. Kretschmer and K. Binder *Phys. Rev. B* **20**, 1065 (1979).

[113] J. Junquera and P. Ghosez, *Nature* **422**, 506 (2003).

[114] D. L. Tilley, *Ferroelectrics* **134**, 313 (1992).

[115] L. Q. Chen, *Physics of Ferroelectrics: a Modern Perspective* (Springer-Verlag, Berlin, 2007, pp. 363-371).

[116] A. Antons, J. B. Neaton, K. M. Rabe and D. Vanderbilt *Phys. Rev. B* **71**, 024102 (2005).

[117] C. Lichtensteiger, J.-M. Triscone, J. Junquera and P. Ghosez, *Phys. Rev. Lett.* **94**, 047603 (2005).

[118] Z-G. Ban, S. P. Alpay and J. V. Mantese, *Phys. Rev. B* **67**, 184104 (2003); Z.-G. Ban, S.P. Alpay and J. V. Mantese, *Integ. Ferr.* **58**, 1281 (2003).

[119] D. Fuchs, C. W. Schneider, R. Schneider and H. Rietschel *J. Appl. Phys.* **85**, 7362 (1999).

[120] H. N. Lee, S. Nakhmanson, M. F. Chisholm, H. M. Christen, K. M. Rabe and D. Vanderbilt, *Proceedings of Fundamental Physics of Ferroelectrics* (2007), unpublished.

[121] G. Catalan, B. Noheda, J. McAneney, L. J. Sinnamon and J. M. Gregg, *Phys. Rev. B* **72**, 020102 (2005).

[122] D. Balzar, P. A. Ramakrishnan, P. Spagnol, S. Mani, A. M. Hermann and M. A. Matin, *Jpn. J. Appl. Phys.* **41**, 6628 (2002).

[123] S. P. Alpay, Z.-G. Ban and J. V. Mantese, *Appl. Phys. Lett.* **82**, 1269 (2003).

[124] Y. Arimoto and H. Ishiwara, *MRS Bulletin* **29**, 823 (2004).

[125] J. Cardy, *Scaling and Renormalization in Statistical Physics* (Cambridge University Press, Cambridge, 1996).

[126] S. L. Sondhi, S. M. Girvan, J. P. Carini and D. Shahar, *Rev. Mod. Phys* **69**, 315 (1997).

[127] S. Sachdev, *Quantum Phase Transitions* (Cambridge University Press, Cambridge, 1999).

[128] M. A. Continentino, *Quantum Scaling in Many-Body Systems* (World Scientific, Singapore, 2001).

[129] P. Coleman and A. J. Schofield, *Nature* **433**, 226 (2005).

[130] H. B. G. Casimir, *Proc. Kon. Ned. Akad. Wetenschap* **51**, 793 (1948); H. B. G. Casimir and D. Polder, *Phys. Rev.* **73**, 360 (1948).

[131] M. Krech, *The Casimir Effect in Critical Systems* (World Scientific, Singapore, 1994).

[132] M. Kardar and R. Golestanian, *Rev. Mod. Phys.* **71**, 1233 (1999).

[133] S. K. Lamoreaux, Phys. Rev. Lett. **78**, 5 (1997).

[134] U. Mohideen and A. Roy, Phys. Rev. Lett. **81**, 4549 (1998).

[135] H. B. Chan, V. A. Aksyuk, R. N. Kleiman, D. J. Bishop and F. Capasso, Science **291**, 1941 (2001).

[136] M. Lisanti, D. Iannuzzi and F. Capasso, PNAS **102**, 11989 (2005).

[137] J. M. Obrecht, R. J. Wild, M. Antezza, L. P. Pitaevskii, S. Stringari and E. A. Cornell, Phys. Rev. Lett. **98**, 063201 (2007).

[138] A. B. Rechester, *Sov. Phys. JETP* **33**, 423 (1971).

[139] D. E. Khmelnitskii and V. L. Shneerson, *Sov. Phys.- Solid State* **13**, 687 (1971); *ibid Sov. Phys. JETP* **37**, 164 (1973).

[140] R. Roussev and A. J. Millis, **67**, 014105 (2003).

[141] N. Das and S. G. Mishra, *J. Phys.: Condens. Matter.* **21**, 095901 (2009).

[142] T. Schneider, H. Beck and E. Stoll, *Phys. Rev. B* **13**, 1123 (1976).

[143] D. Schmeltzer, *Phys. Rev. B* **27**, 459 (1983).

[144] S. Sachdev, *Phys. Rev. B* **55**, 142 (1997).

[145] A. Lambrecht, Physics World **15** (9), 29 (2002).

[146] S. K. Lamoroeaux, Phys. Today **60** (2), 40 (2007).

[147] J. N. Munday, F. Capasso, and V. A. Parsegian, "Measured long-range repulsive Casimir-Lifshitz forces," *Nature* **457**, 170–173 (2009).

[148] M. E. Fisher and P. G. deGennes, *C.R. Acad. Sci. Paris B* **287**, 207 (1978).

[149] D. M. Danchev, J. G. Brankov and N. S. Tonchev, *Theory of Critical Phenomena in Finite-Size Systems: Scaling and Quantum Effects* (World Scientific, Singapore, 2000).

[150] A. Gambassi, *J. Phys.: Conf. Ser.* **161** 012037 (2009).

[151] F. J. Belinfante, *Am. J. Phys.* **55**, 134 (1987).

[152] J. P. Dowling, *Mathematics Magazine* **62**, 324 (1989).

[153] E. Elizalde and A. Romeo, *Am. J. Phys.* **59**, 711 (1991).

[154] M. Revzen, R. Opher, M. Opher and A. Mann, *Europhys. Lett.* **38**, 245 (1997).

[155] S. K. Lamoreaux, *Am. J. Phys.* **67**, 850 (1999).

[156] J. D. Jackson, *Classical Electrodynamics 3rd Edition* (John Wiley & Sons, New York, 1998).

[157] G. D. Mahan, *Many-Particle Physics 3rd Edition* (Springer, New York, 2007).

[158] T. H. Boyer, *Phys. Rev. A* **9**, 2078 (1974).

[159] V. Hushwater, *Am. J. Phys.* **65**, 381 (1997).

[160] L. Pálová, P. Chandra and P. Coleman, *Am. J. Phys.* **77**, 1055 (2009).

[161] J. Hertz, *Phys. Rev. B* **14**, 1165 (1976).

[162] D. Rytz, U. T. Hochli and H. Bilz, *Phys. Rev. B* **22**, 359 (1980).

[163] E. Brezin and J. Zinn-Justin, *Nucl. Phys. B* **257**, 867 (1985).

[164] J. Rudnick, H. Guo and D. Jasnow, *J. Stat. Phys.* **41**, 353 (1985).

[165] H. Chamati D. M. Danchev and N. S. Tonchev, *Eur. Phys. J. B* **14**, 307 (2000).

[166] M. C. Aronson, R. Osborn, R. A. Robinson, J. W. Lynn, R. Chau, C. L. Seaman and M. B. Maple, Phys. Rev. Lett. **75**, 725 (1995).

[167] A. Schroeder, G. Aeppli, R. Coldea, M. Adams, O. Stockert, H. von Lohneyson, E. Bucher, R. Ramazashvili and P. Coleman, Nature **407**, 351 (2000).

[168] T. Moriya, *Spin Fluctuations in Itinerant Electron Magnets* (Springer-Verlag, Berlin, 1985).

[169] J. H. Barrett, *Phys. Rev.* **86**, 118 (1952).

[170] Y. Yamada and G. Shirane, *J. Phys. Soc. Japan* **26**, 396 (1969).

[171] M. Takesada, M. Itoh and T. Yagi, *Phys. Rev. Lett.* **96**, 227602 (2006).

[172] C. v. K. Schmising, M. Bargheer, M. Kiel, N. Zhavoronkov, M. Woerner, T. Elsaesser, I. Vrejoiu, D. Hesse and M. Alexe, *Phys. Rev. B* **73**, 212202 (2006).

[173] R. O. Bell and G. Rupprecht, *Phys. Rev.* **129**, 90 (1963).

[174] L. Pálová, P. Chandra and K. M. Rabe, Phys. Rev. B **76**, 014112 (2007).

[175] T. Moriya and J. Kawabata, J. Phys. Soc. Japan **34**, 639 (1973); J. Phys. Soc. Japan **35**,669 (1973).

[176] J. A. Hertz, Phys. Rev. B **14**, 1165 (1976).

[177] A. J. Millis, Phys. Rev. B **48**, 7183 (1993).

[178] A. I. Larkin and D. E. Khmel'nitskii, *Sov. Phys. JETP* **29**, 1123 (1969).

[179] H. Taniguchi and M. Itoh, *Phys. Rev. Let.* **99**, 017602 (2007).

[180] A. J. Millis, A. J. Schofield, G. G. Lonzarich and S. A. Grigera, *Phys. Rev. Let.* **88**, 217204 (2002).

[181] P. Gegenwart, Q. Si and F. Steglich, *Nature* **4**, 186 (2008).

[182] J. W. Kim, S. Y. Haam, Y. S. Oh, S. Park, S.-W. Cheong, P. A. Sharma, M. Jaime, N. Harrison, J. H. Han, G.-S. Jeon, P. Coleman and K. H. Kim, *PNAS* **106**, 15573 (2009).

[183] N. D. Mathur, F. M. Grosche, S. R. Julian, I. R. Walker, D. M. Freye, R. K. W. Haselwimmer and G. G. Lonzarich, *Nature* **394**, 39 (1998).

[184] B. Laughlin, G. G. Lonzarich, P. Monthoux and D. Pines, *Adv. Phys.* **50**, 361 (2001).

[185] P. Coleman, C. Pepin, Q. Si and R. Ramazashvili, *J. Phys.: Condens. Matter* **13**, 723(R) (2001).

[186] H. von Löhneysen, A. Rosch, M. Vojta, M. and P. Wolfe, Rev. Mod. Phys. **79**, 1015 (2007).

[187] R. Ramesh and D. G. Schlom, *Science* **296**, 1975 (2002).

[188] C. Cen, S. Thiel, J. Mannhart and J. Levy, *Science* **323**, 1026 (2009).

[189] J. Mannhart and D. G. Schlom, *Science* **327**, 1607 (2010).

[190] H. Zheng, J. Wang, S. E. Lofland, Z. Ma, L. Mohaddes-Ardabili, T. Zhao, L. Salamanca-Riba, S. R. Shinde, S. B. Ogale, F. Bai, D. Viehland, Y. Jia, D. G. Schlom, M. Wuttig, A. Roytburd and R. Ramesh, *Science* **303**, 661 (2004).

[191] J. L. MacManus-Driscoll, P. Zerrer, H. Wang, H. Yang, J. Yoon, A. Fouchet, R. Yu, M. G. Blamire and Q. Jia, *Nature Mater.* **7**, 314 (2008).

[192] S. Yeo, Y. Horibe, S. Mori, C. M. Tseng, C. H. Chen, A. G. Khachaturyan, C. L. Zhang and S.-W. Cheong, *Appl. Phys. Lett.* **89**, 233120 (2006).

[193] C. L. Zhang, S. Yeo, Y. Horibe, Y. J. Choi, S. Guha, M. Croft, S.-W. Cheong and S. Mori, *Appl. Phys. Lett.* **90**, 133123 (2007).

[194] C. L. Zhang, C. M. Tseng, C. H. Chen, S. Yeo, Y. J. Choi and S.-W. Cheong, *Appl. Phys. Lett.* **91**, 233110 (2007).

[195] B. S. Guiton and P. K. Davies, *Nature Mater.* **6**, 586 (2007).

[196] C. A. F. Vaz, J. Hoffman, C. H. Ahn and R. Ramesh, *Adv. Mater.* **XX**, 1 (2010).

[197] D. P. Kozlenko, V. P. Glazkov, R. A. Sadykov, B. N. Savenko, V. I. Voronin and I. V. Medvedeva, *J. Magn. Mag. Mat.* **258-259**, 290 (2003).

[198] J. H. Lee and K. M. Rabe, *Phys. Rev. Lett.* **104**, 207204 (2010).

[199] T. Murata, H. Kushida, T. Terai and T. Kakeshita, *J. Magn. Mag. Mat.* **310**, 1555 (2007).

[200] C. J. Fennie and K. M. Rabe, *Phys. Rev. Lett.* **97**, 267602 (2006).

[201] R. T. Lechner, G. Springholz, T. U. Schlli, J. Stangl, T. Schwarzl and G. Bauer, *Phys. Rev. Lett.* **94**, 157201 (2005).

[202] J. M. Rondinelli, M. Stengel and N. A. Spaldin, *Nature Nanotechnology* **3**, 46 (2008).

[203] P. Baettig and N. A. Spaldin, *Appl. Phys. Lett.* **86**, 012505 (2005).

[204] P. E. Blochl, *Phys. Rev. B* **50**, 17953 (1994).

[205] G. Kresse and J. Joubert, *Phys. Rev. B* **59**, 1758 (1999).

[206] A. I. Liechtenstein, V. I. Anisimov and J. Zaane, *Phys. Rev. B* **52**, R5467 (1995).

[207] S. L. Dudarev, G. A. Botton, S. Y. Savrasov, C. J. Humphreys and A. P. Sutton, *Phys. Rev. B* **57**, 1505 (1998).

[208] I. Sosnowska, W. Schfer, W. Kockelmann, K. H. Andersen and I. O. Troyanchuk, Appl. Phys. A: Mater. Sci. Process. **74**, S1040 (2002).

[209] H. J. Monkhorst and J. D. Pack, *Phys. Rev. B* **13**, 5188 (1976).

[210] P. E. Blochl, O. Jepsen and O. K. Andersen, *Phys. Rev. B* **49**, 16223 (1994).

[211] N. Marzari and D. Vanderbilt, *Phys. Rev. B* **56**, 12847 (1997).

[212] O. Paz and K. M. Rabe (private communication).

[213] C. Michel, J.-M. Moreau, G. D. Achenbach, R. Gerson and W. J. James, *Solid State Commun.* **7**, 701 (1969).

[214] F. Kubel and H. Schmid, *Acta Cryst. B* **B46**, 698 (1990).

[215] S. Coh, T. Heeg, J. H. Haeni, M. D. Biegalski, J. Lettieri, L. F. Edge, K. E. O'Brien, P. Reiche, R. Uecker, S. Trolier-McKinstry, D. G. Schlom and D. Vanderbilt, arXiv:1005.2767v1.

[216] J. B. Goodenough, *Phys. Rev.* **100**, 564 (1955).

[217] J. Kanamori, *J. Phys. Chem. Solids* **10**, 87 (1959).

[218] J. H. Lee and K. M. Rabe (private communication).

[219] C. Ederer and N. A. Spaldin, *Phys. Rev. Lett.* **95**, 257601 (2005).

[220] A. J. Hatt, N. A. Spaldin and C. Ederer, *Phys. Rev. B* **81**, 054109 (2010).

[221] R. J. Zeches, M. D. Rossell, J. X. Zhang, A. J. Hatt, Q. He, C.-H. Yang, A. Kumar, C. H. Wang, A. Melville, C. Adamo, G. Sheng, Y.-H. Chu, J. F. Ihlefeld, R. Erni, C. Ederer, V. Gopalan, L. Q. Chen, D. G. Schlom, N. A. Spaldin, L. W. Martin and R. Ramesh, *Science* **326**, 977 (2009).

[222] T. Atou, H. Chiba, K. Ohoyama, Y. Yamaguchi and Y. Syono, *J. Solid State Chem.* **145**, 639 (1999).

[223] T. Shishidou, N. Mikamo, Y. Uratani, F. Ishii and T. Oguchi, *J. Phys.: Condens. Matter* **16**, S5677 (2004).

[224] S. A. Wolf, D. D. Awschalom, R. A. Buhrman, J. M. Daughton, S. von Molnár, M. L. Roukes, A. Y. Chtchelkanova and D. M. Treger, *Science* **294**, 1488 (2001).

[225] N. A. Hill and K. M. Rabe, *Phys. Rev. B* **59**, 8759 (1999).

[226] C.-H. Yang, T. Y. Koo, S.-H. Lee, C. Song, K.-B. Lee and Y. H. Jeong, *Europhys. Lett.* **74**, 348 (2006).

[227] P. Baettig, C. Ederer and N. A. Spaldin, *Phys. Rev. B* **72**, 214105 (2005).

[228] C.-H. Yang, T. Y. Koo and Y.H. Jeong, *Journal of the Korean Physical Society* **55**, 80 (2009).

[229] Y.-H. Chu, M. P. Cruz, C.-H. Yang, L. W. Martin, P.-L. Yang, J.-X. Zhang, K. Lee, P. Yu, L.-Q. Chen and R. Ramesh, *Adv. Mater.* **19**, 2662 (2007).

[230] J. Y. Son and Y.-H. Shin, *Appl. Phys. Lett.* **93**, 062902 (2008).

Curriculum Vitae
Lucia Pálová

2010   Ph.D. in Physics, Rutgers University, NJ, USA.

2004   "Magister", Faculty of Mathematics, Physics and Informatics, Comenius University, Bratislava, Slovakia.

2007-2010 Graduate Assistant, Department of Physics and Astronomy, Rutgers University, NJ.

2004-2007 Teaching Assistant, Department of Physics and Astronomy, Rutgers University, NJ.

Publications

Lucia Pálová, Premala Chandra and Karin M. Rabe, *Multiferroic BiFeO$_3$-BiMnO$_3$ Nanocheckerboard from First Principles*, arXiv:1006.4648v1.

Daisuke Kan, Lucia Pálová, Varatharajan Anbusathaiah, Ching Jung Cheng, Shigehiro Fujino, Valanoor Nagarajan, Karin M. Rabe, and Ichiro Takeuchi, *Universal Behavior and Electric Field-Induced Structural Transition in Rare-Earth Substituted BiFeO$_3$*, Adv. Funct. Mater. **20**, 1 (2010).

Lucia Pálová, Premala Chandra and Karin M. Rabe, *Magnetostructural Effect in the Multiferroic BiFeO$_3$-BiMnO$_3$ Checkerboard from First Principles*, Phys. Rev. Lett. **104**, 037202 (2010).

Lucia Pálová, Premala Chandra and Piers Coleman, *The Casimir Effect from a Condensed Matter Perspective*, Am. J. Phys. **77**, 1055 (2009).

Lucia Pálová, Premala Chandra and Piers Coleman, *Quantum Critical Paraelectrics and the Casimir Effect in Time*, Phys. Rev. B **79**, 075101 (2009).

Lucia Pálová, Premala Chandra and Karin M. Rabe, *Modeling the Dependence of Properties of Ferroelectric Thin Film on Thickness*, Phys. Rev. B **76**, 014112 (2007).

Lucia Bodnárová, *Anomalous Atomic Dynamics of Crystal Al$_{10}$V*, Diploma thesis, Comenius University, Bratislava, Slovakia (2004).